PFC/RR-82-10

DOE/ET-51013-39
UC20B

Physical and Engineering Constraints

for

Tokamak Reactors and Helical Coils

R.E. Potok, H. Becker, L. Bromberg,
D. Cohn, N. Diatchenko
P.B. Roemer, J.E.C. Williams

Plasma Fusion Center
Massachusetts Institute of Technology
Cambridge, MA 02139

June 1982

Physical and Engineering Constraints for Tokamak Reactors with Helical Coils

R.E. Potok, H. Becker, L. Bromberg,

D.R. Cohn, N. Diatchenko, P.B. Roemer,

J.E.C. Williams

Abstract

We present an analytical and numerical analysis of a tokamak reactor with a set of helical coils added in order to eliminate plasma disruptions. A number of design options for the helical coils are considered (resistive or superconducting coils, placement internal or external to the toroidal field magnets, continuous or modular coils, and type of winding law). The optimum helical configuration is found to be a set of resistive, continuous, $\ell = 2$ stellarator coils which are internal to the toroidal field coils. A set of scaling laws is then developed for this optimal configuration, and a series of parametric scans are done with varying assumptions for the forces on the helical coils and the ratio of helical coil transform to plasma transform (M^*).

We show that the option space available for reactor designs involves large forces on the helical coils, low q plasma operation, and moderately low M^*. We compare data from experimental devices run in the tokamak–stellarator mode (JIPP-T-II and Pulsator) with field tracing data. There is good agreement between the results of the experiments and the field line tracing. These results show that too low a value of M^* (3 to 5) will cause a destructive resonance interaction between the plasma and helical coil transforms. M^* must be kept at moderately low levels (4 to 6), though, if the forces on the helical coils and their power dissipation are to be acceptably small. There is thus only a narrow region in parameter space where an attractive reactor design can be built, and this region only exists if the helical coils enable the reactor to operate in a low q regime ($q_{edge} \simeq 1.5$).

Under the above mentioned constraints, an illustrative tokamak–stellarator reactor design is developed. A moderately large major radius is required, ($R_o = 14.31$ m), since the external transform scales as R_o^2. The large major radius allows for much higher flux storage in the OH coils (for the same OH energy storage) than is found in conventional tokamaks, and burn times on the order of 10 hours appear feasible.

The illustrative design is based upon a remote maintenance scheme in which removable, modular units of the reactor consist of: two toroidal field coils, sectors of helical coils, and sectors of the blanket/shield region and first wall. The resistive helical coils are water cooled and are clamped together at the module interfaces. The helical coils are supported by a reinforcing structure external to the helical coils and internal to the toroidal field coils.

Table of Contents

Chapter I. Introduction and Summary

1.1 Use of Externally Supplied Rotational Transform in a Tokamak

There has been considerable interest in recent years in adding an external rotational transform ($\bar{\iota}$) to the tokamak magnetic configuration. There is both theoretical[1] and experimental[2] evidence that such an addition (with $\bar{\iota} \simeq .15$) will prevent tokamak plasma disruptions, and thereby make the tokamak a more attractive reactor concept. The external transform could also increase the reactor's β by allowing a lower q operation.

In this report, we investigated the addition of stellarator windings to a tokamak reactor. A detailed analytical and numerical investigation was made of an illustrative design. A number of parametric studies were done, comparing the performance of helical coils in terms of winding law, ℓ number, pitch length, major and minor radii, and current. The ability to combine the fields from the helical coils with tokamak-reactor equilibrium fields (obtained from the PEST code) was then explored, and a comparison made with present experiments (JIPP-T-II and Pulsator). The engineering requirements of a tokamak-stellarator reactor were evaluated, and an illustrative design was developed. The overall attractiveness of the concept was then assessed.

1.2 Magnet Design Choices

A number of magnet design choices were made:

1) superconducting or resistive magnets,

2) placement of helical coils inside or outside the toroidal field coils,

3) continuous, demountable coils or modular coils,

4) geometry of helical coils (ℓ number, torsatron or stellarator configuration, and winding law).

A resistive, continuous, $\ell = 2$ stellarator winding internal to the TF coils was chosen as the optimal helical coil system for adding external transform. The $\ell = 2$ winding configuration was found to superimpose the most external transform onto the plasma transform for fixed helical current, and the stellarator configuration resulted in a smaller peak bending stress (a dominant constraint) than an equivalent torsatron configuration. Superconducting helical coils were not used because of the difficulties in assembling superconducting helices internal to the toroidal field coils. If the superconducting coils were placed external to the toroidal field coils, the helical current would be on the same order as the toroidal current ($\simeq$ 20 MA per coil), and a twisted toroidal field coil design would be a better approach (there would be little advantage in separating the magnetic configuration into separate toroidal and helical systems). A continuous coil design (rather than a modular, dipole coil design) was chosen because this feature greatly decreases the bending moments and torques that act upon the helical coils due to their interaction with the toroidal field.

1.3 Scaling Laws and Engineering Constraints

With the magnetic geometry chosen, it was found that the choices for vacuum $\bar{\iota}$, $K_\beta(\beta_l = K_\beta/A)$, B_{zo} (the toroidal field on axis), N (number of helical field periods), dissipated magnet power, and total fusion power would determine the plasma and helical coil minor radii. The additional choice of $\mathcal{Q}$, the average force/meter on the helices, determines the major radius. The reactor scaling is set by the expression:

$$\bar{\iota} = \frac{4}{N}\left(\frac{1}{r_{\text{coil}}}\right)^4\left(\frac{\mu_o}{\pi}\frac{R_o I_h}{B_{zo}}\right)^2$$

The helical current I_h should be as low as possible, in order to minimize the forces on the helical coils and the helical coil dissipative power loss. For fixed $\bar{\iota}$, the need to minimize the helical coil current I_h results in a design with low N and r_{coil} and with large major radius (R_o). The forces on the helical coils are inversely proportional to the major radius, so structural support requirements also favor a large R_o. Unfortunately, tokamaks with aspect ratio (large major radius and small r_{coil}) tend toward low wall loading and margin on ignition, due to the inverse plasma aspect ratio dependence of the plasma β. (The margin of ignition is defined as $\tau_{\text{emp}}/\tau_{\text{ign}}$. τ_{emp} is the energy confinement time given by the empirical scaling law $\tau_{\text{emp}} \sim na_p^2$ (n and a_p being the plasma density and plasma radius, respectively). τ_{ign} is the energy confinement time required for ignition at a given temperature). The optimum choice for R_o is determined by a trade-off among these different scalings.

1.4 Parametric Studies — Low N and M^*

It was found that an attractive reactor required a small number of helical coil periods (N/ℓ), leading to low M^* (the ratio of the helical coil transform to plasma transform). A large average force/meter on the helical coils was also needed. The ⟨force/meter⟩ was found to be approximately inversely proportional to the major radius (R_o) and thermal output (P_{th}) of the reactor, and high forces ($\geq$ 10 MN/m) were found to be necessary to keep $R_o \leq 20$ m and $M^* \geq 5$ (the present experimental limit on M^*). The power dissipation requirements of the helical coils determined the amount of copper needed by the coils, and thus influences the helical coil radial thickness and minor radius.

The $M^* \leq 5$ regime was found necessary for an attractive reactor. We have also found that the average force/meter on the helices ($\mathbb{Q}$) must be $\geq$ 10 MN/m for an attractive wall loading and total thermal power output. Analyses of the support requirements in Chapters V and VII show, however, that $\mathbb{Q} \simeq 10 - 15$ MN/m is a practical upper limit in the design of the helical coil support structure. Thus the option space for an attractive reactor design is limited.

A comparison was made between numerical field-line tracing and experimental results of JIPP-T-II[3] on the minimum M^* obtainable in tokamak-stellarator configurations. There was good agreement between the two results, JIPP-T-II showed that the plasma was unstable to tearing instabilities for $M^* \leq 5$ and $\bar{\iota}^{vacuum} \leq .1$, and the numerical analysis showed that the well defined flux surfaces of a tokamak would be replaced by ergodic field lines for $M^* \leq 3$ and $\bar{\iota}^{vacuum} \leq .15$.

1.5 Illustrative Design Parameters

A summary of the base design parameters is given in Table 1.1 . The tokamak-stellarator reactor has a large major radius, even if the optimistic $M^* = 4$ regime is assumed. In addition, one must assume that the external transform would allow a low q operation in order to achieve a high fusion power density. For the base design, q^{edge} was assumed to be 1.4 . The following constraints were also picked: $B_{zo} = 6$ tesla, $P_{th} = 3000$ MW, helical coil power dissipation = 240 MW, and the average force/length on the helical coils = 10 MN/m. This resulted in a major radius = 14.31 m, a plasma minor radius $a_p = 1.52$ m, and a helical coil minor radius = 2.50 m. The toroidal magnet system was divided into 16 modular units, each consisting of two toroidal field coils and internal helical coil segments. The performance of the helical coils (721 A/cm^2), was kept low in order to minimize the dissipative power.

Figure 1.1 shows a side view of the illustrative design. Figure 1.2 shows a 30^o elevated view of the machine. This figure shows that the helical coils have a pitch length (the toroidal distance traversed during one poloidal revolution of the coil) equal to $\frac{1}{4}$ of the major circumference. The helical coil sections are attached to a ring support system in which the peak bending stress is approximately 200 MPa. The module to module electrical connections are achieved with copper inserts. Figure 1.3 shows a plan view of a module.

R_o	14.31 meters
a_{plasma}	1.52 meters
B_{zo}	6 tesla
β_t	5.3%
Margin of Ignition	5.53
Wall Loading	3.50 MW/m^2
$P_{lh}^{primary}$	3000 MW
N , M^*	8 , 4
$\bar{\iota}_{external}$	0.1
r_{coil}	2.50 meters
I_{helix}	2.91 MA
I_p	2.94 MA
Resistive Power Loss	240 MW
Force on Helices	10 MN/m

Illustrative Design Parameters

Table 1.1

The low current density of the helical coils will facilitate the demountable design of the joints which join the modular helical segments together. Each of the helical coils carries a current of 2.91 MA (15 cables of 194 KA each). The helical coil support structure must allow sufficient access for the joints to be bolted together. A detailed description of the support structure is given in Chapters V and VII.

The plasma current of the base design was 2.94 MA, and the large major radius allows a much higher flux storage in the OH coil (for the same OH energy storage) than is found in conventional tokamaks with smaller major radii. Defining B_{OH} to be the peak field in the OH coil the OH energy requirements of the base design can be written as $E_{OH} = 1.7$ GJ-tesla$^2/B_{OH}^2$, and there are more than 400 volt-seconds available during the burn (after start-up) for each tesla in the OH coil. This results in an ideal burn time of 5 hours per tesla B_{OH}, and thus actual burn times on the order of 10 hours appear feasible.

The illustrative design brings out some interesting features of high aspect ratio tokamaks. In addition to the potential for very long pulse lengths, the modular design of the magnet system facilitates straight-forward replacement of the toroidal field coils and sectors. A remote maintenance scheme can be based upon complete removal of a module containing two toroidal field coils, sectors of the helical coils, and sectors of the blanket/shield region and first wall. The toroidal field coils could have independent cryogenic systems, and could be supported by room temperature structure through thermally insulating barriers. The cryogenic losses would be low.

1.6 Conclusions

Under an optimal set of physics and engineering assumptions, an attractive illustrative design can be developed for a tokamak reactor with helical coils. The device would be an improvement over the conventional tokamak in terms of its capability of disruption control, its capability for very long pulses ($\simeq$ 10 hours), and its capability for operating at lower q and higher values of β. The device would also have a completely modular design. While it is larger than a conventional tokamak reactor, it is smaller than stellarator or torsatron reactors (which have proposed major radii of 20 to 30 meters).

The design space for the tokamak-stellarator reactor is very sensitive to the allowed values of M^* ($M^* = \bar{\iota}^{winding}/\bar{\iota}^{plasma}$), q at the plasma edge, and the forces on the helical coils. If larger values of M^* and q^{edge} and smaller helical forces are necessary (compared to the base design assumptions), the reactor becomes very large and unattractive. The allowable force/meter on the helical coils is severely limited, compared with the forces allowed in a typical tokamak or torsatron design. In a tokamak design, the coil forces do not produce the large bending moments as they do in a tokamak-stellarator design. In a torsatron design, the massive coil support structure need not be contained inside the bore of a TF coil system, and furthermore, there is no external toroidal field with which the helical coils interact. The twisted toroidal field coil reactor (that is, a modular stellarator design) may also have stringent limitations on the allowable forces on the coil structures, due to the torques and bending moments these forces will create on the twisted coils.

If the tokamak-stellarator device could be designed with the average force/length on the helical coils ($\mathfrak{Q}$) equal to 30–40 MN/m, an attractive reactor could be built with experimentally and

theoretically justified physics assumptions ($M^* \geq 5$, $i^{external} \geq .15$, $q^{edge} \geq 2.5$). There does not appear, however, to be a way to support such loads inside the TF coils effectively. In order to obtain an attractive reactor design with $\mathcal{Q} = 10$ MN/m, low q operation ($q^{edge} \simeq 1.5$) must be assumed.

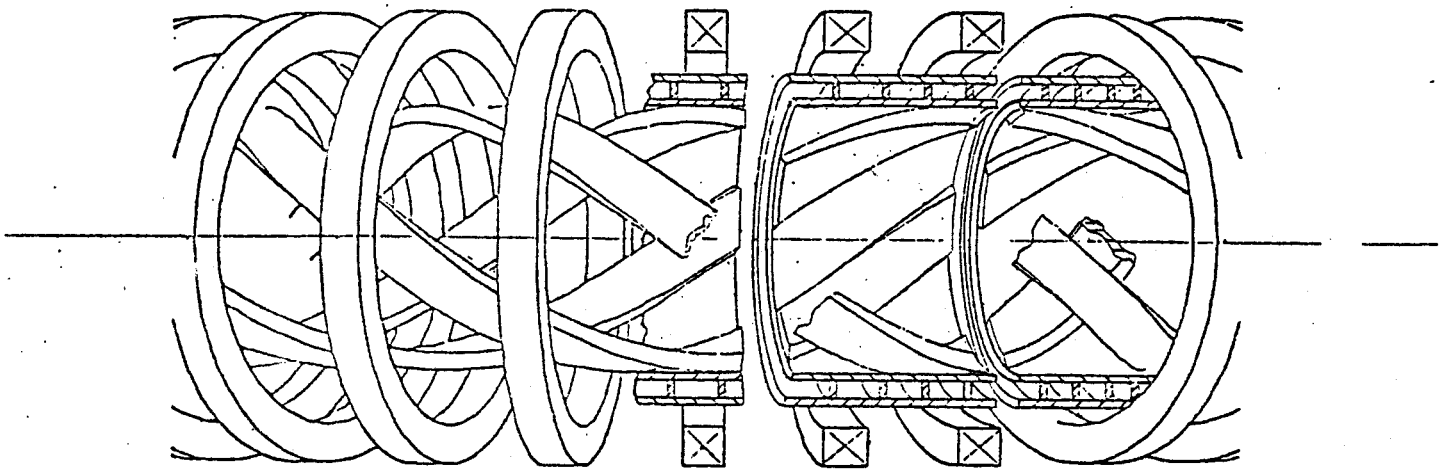

FIGURE 1.1
SIDE VIEW OF ILLUSTRATIVE DESIGN

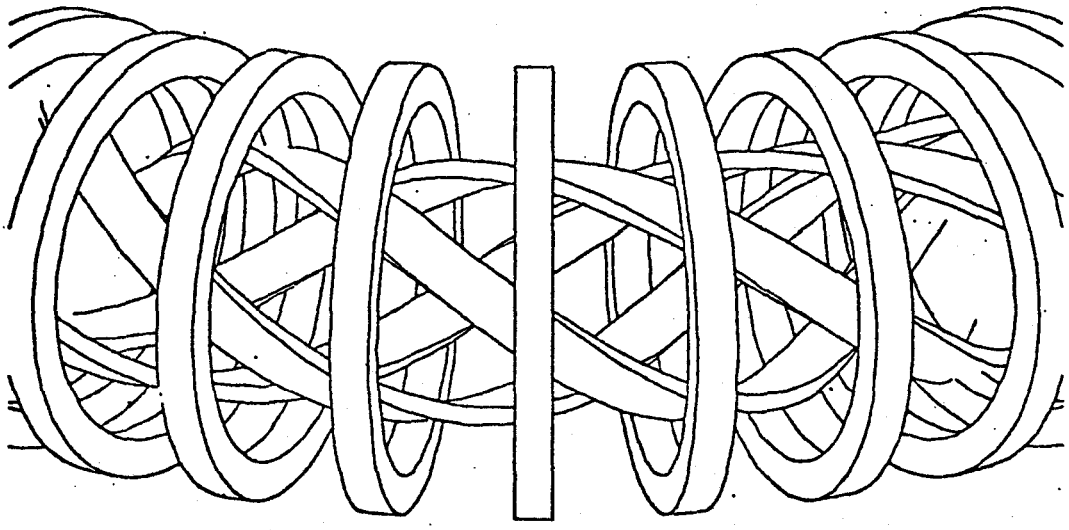

FIGURE 1.2
30° ELEVATION VIEW OF HELICAL AND TOROIDAL FIELD COILS

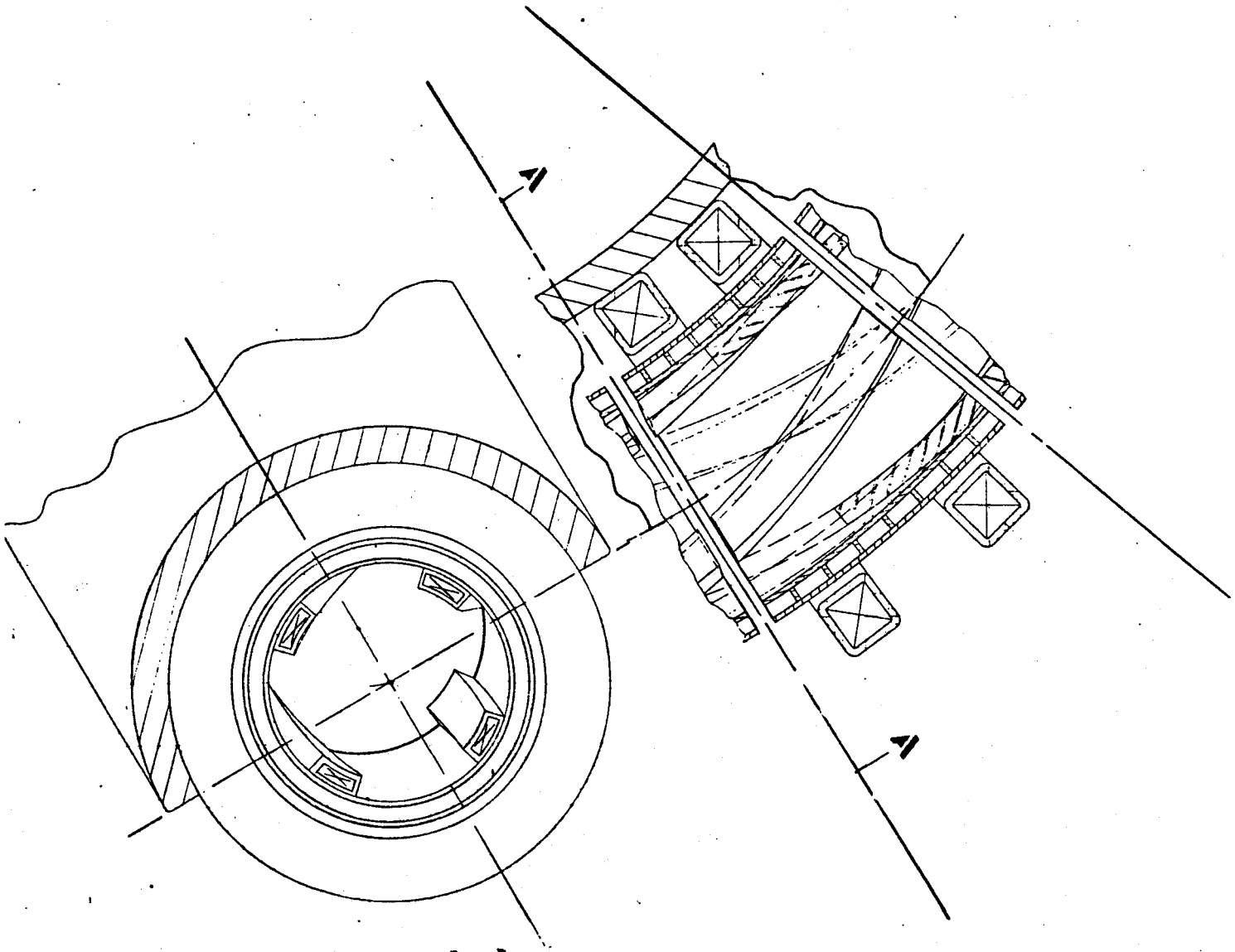

FIGURE 1.3
PLAN VIEW OF REACTOR MODULE

References

1) P. A. Politzer, et. al. Bulletin of the American Physical Society; 25, 8, October 1980 — paper 2R7; American Institute of Physics; New York, NY

2) J. Fujita, et. al. Proceedings of the Eighth International Conference Plasma Physics and Controlled Nuclear Fusion Research; Brussels, 1, p. 209, 1–10 July 1980, International Atomic Energy Agency, Vienna, Austria

3) J. Fujita, et. al. Proceedings of the Eighth International Conference Plasma Physics and Controlled Nuclear Fusion Research; Brussels, 1, p. 209, 1–10 July 1980, International Atomic Energy Agency, Vienna, Austria

4) L. M. Lidsky, et. al. M.I.T. report PFC/IR/81-1, 1981, Cambridge, Mass.

5) F. Karger, et. al. Proceedings of the Sixth International Conference on Plasma Physics and Controlled Nuclear Fusion Research; Berchtesgaden 1, p. 267, 6–13 October 1976, International Atomic Energy Agency, Vienna, Austria

6) The Alcator A Modification Proposal, MIT Plasma Fusion Center, 1981, Cambridge, Massachusetts

Chapter II. Coil Geometries of Tokamak-Stellarator Reactors

In this chapter, we discuss the advantages and disadvantages of various coil designs, and show that a resistive-coil, continuously wound, demountable helical magnet system located inside the toroidal field coil bore is the most practical magnet configuration for a tokamak-stellarator reactor.

2.1 Helical Coil Configurations

The helical geometry is illustrated in Figure 2.1 . The magnetic field produced by a set of ℓ helical coils in a straight (cylindrical) configuration is[1]:

$$B_r = B_Z \sum_{m=l}^{\infty} C_m m\ell(k\, r_{\text{coil}}) K'_{m\ell}\Big[m\ell(k\, r_{\text{coil}})\Big] I'_{m\ell}\Big[m\ell(k\, r)\Big] \sin(m\ell a)$$

$$B_\theta = B_Z \sum_{m=1}^{\infty} C_m m\ell\left(\frac{\dot{r}_{\text{coil}}}{r}\right) K'_{m\ell}\Big[m\ell k\, r_{\text{coil}}\Big] I_{m\ell}\Big[m\ell(k\, r)\Big] \cos(m\ell a)$$

$$B_z = B_Z\left(1 - \sum_{m=1}^{\infty} C_m m\ell(k\, r_{\text{coil}}) K'_{m\ell}\Big[m\ell(k\, r_{\text{coil}})\Big] I_{m\ell}\Big[m\ell(k\, r)\Big] \cos(m\ell a)\right)$$

where

$$C_m = \frac{2sin(m\pi f_o)}{m\pi f_o}$$

$$B_Z = \frac{\mu_o \ell I_h}{p}$$

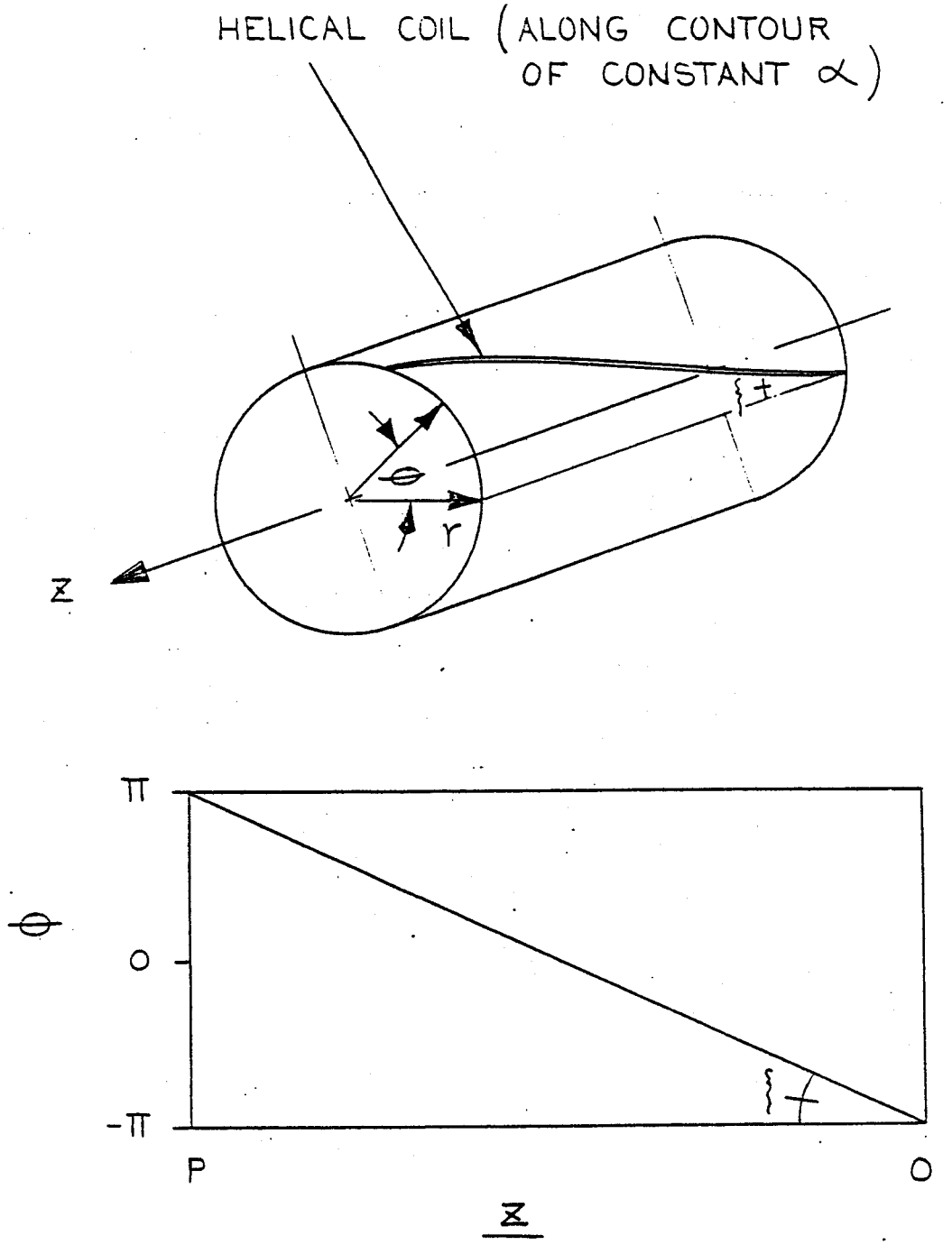

FIGURE 2.1

HELICAL COIL GEOMETRY

I and K are the modified Bessel functions of integer order

f_o = total fraction of the $r = r_{\text{coil}}$ surface that is covered by ℓ windings

p = pitch length of coils (axial distance covered during one poloidal revolution of coil)

$$k = \frac{2\pi}{p}$$

$$\alpha = \theta - \frac{2\pi Z}{p}$$

A cylindrical stellarator field is composed of two sets of ℓ windings (carrying helical currents I_1 and I_2 in opposite axial directions and having opposite signs for B_Z), plus an additional B_{zo} field from axial field coils. A cylindrical torsatron field is composed of one set of ℓ windings (each carrying helical current $I_1 = I_h$, with $I_2 = 0$), and additional axial field coils are optional since there is a net B_Z from the helical coils.

2.2 Choice of ℓ number

Keeping only the lowest order terms of the Bessel series, the rotational transform $\bar{\iota}$ per winding period may be expressed as:

$$\bar{\iota}_{\text{winding period}} = \frac{\ell - 1}{\ell}(kr)^{2\ell-4}\left(\frac{B_{lI}}{B_{zo}}\right)^2$$

where

$$\frac{B_{lI}}{B_{zo}} = \frac{\mu_o \ell (I_1 - I_2)}{pB_{zo}} \frac{1}{(kr_{\text{coil}})^\ell}$$

This approximation is valid when:

1) $2 \leq \ell \leq 5$,

2) $kr \ll 1$, and

3) $kr_{\text{coil}} \ll 1$.

The number of field periods in a toroidal configuration is:

$$N = \frac{2\pi R_o \ell}{p} = \ell k R_o$$

with R_o = major radius of coils.

The number of winding periods is:

$$\frac{2\pi R_o}{p} = \frac{N}{\ell}$$

The average rotational transform over the torus is thus:

$$\bar{\iota} = \langle \frac{d\theta}{d\phi} \rangle = \bar{\iota}_{\text{winding period}} \cdot N/\ell$$

$$\bar{\iota} = kR_o \frac{(\ell - 1)}{\ell} (kr)^{2\ell - 4} \left(\frac{B_H}{B_{zo}} \right)^2$$

where

$$\frac{B_H}{B_{zo}} = \frac{N\mu_o}{2\pi R_o} \frac{(I_1 - I_2)}{B_{zo}} \frac{1}{(kr_{\text{coil}})^\ell}$$

After some algebra, $\bar{\iota}$ can be expressed as:

$$\bar{\iota} = \frac{\ell^2(\ell - 1)}{Nr^4} \left(\frac{r}{r_{\text{coil}}} \right)^{2\ell} \left(\frac{\mu_o}{2\pi} \frac{R_o(I_1 - I_2)}{B_{zo}} \right)^2$$

We are now in a position to optimize our choices for ℓ number and I_1/I_2. For fixed I_1, I_2, B_{zo}, N, and R_o, we want to maximize $\bar{\iota}$. We therefore find the ℓ number that maximizes the expression $\ell^2(\ell - 1)\left(\frac{r}{r_{\text{coil}}} \right)^{2\ell}$.

r/r_{coil}	ℓ value that maximizes $\ell^2(\ell - 1)(r/r_{\text{coil}})^{2\ell}$
$0.0 \Rightarrow .47$	2
$.47 \Rightarrow .61$	3
$.61 \Rightarrow .69$	4
$.69 \Rightarrow .75$	5

Table 2.1

There is both theoretical[2] and experimental[3] evidence that the external transform must exist near the magnetic axis in order to damp disruptive instabilities, so ℓ must be ≤ 2. As will be shown later, $a_{\text{plasma}}/r_{\text{coil}}$ will be $\leq .5$, so, from Table 2.1 , $\ell = 2$ clearly adds the most transform, averaged over the plasma cross section. In addition, a higher ℓ number implies more windings, poorer access and, if resistive helical coils are used, a larger dissipative power loss. Therefore, $\ell = 2$ is the optimal choice for the helical coils.

The $\ell = 1$ case was discarded for several reasons. An $\ell = 1$ coil configuration would have a magnetic axis with a large helical pitch, as opposed to $\ell \geq 2$ configurations where the magnetic axis lies on the minor axis. It would thus be impossible to center the helical transform of an $\ell = 1$ coil configuration onto the plasma transform. Also, the vacuum separatrix of an $\ell = 1$ system is smaller and more highly elongated than the separatrix of an $\ell = 2$ system. There is also a large unbalanced translational force with an $\ell = 1$ configuration which is not present for $\ell \geq 2$ configurations. For these reasons, an $\ell = 2$ system was chosen to be superior to an $\ell = 1$ system.

2.3 Magnet Design Options

We now address the question of whether the helical coils should be resistive or superconducting. The helical coil geometries (illustrated in Figure 2.2 and 2.3) can be divided into four general categories:

1) modular, twisted TF coils,

2) dipoles placed between the TF coils which are arranged to excite helical harmonics in the magnetic field, and

3) continuous helical windings inside or outside the TF coil bore.

4) a dragon configuration of TF coils,

The twisted toroidal field coil systems[4,5] are currently being investigated at Wisconsin, Los Alamos, Princeton, and Garching. The system shows promise, though structural support and access remain difficult questions in the twisted coil reactor concept. We have excluded the twisted TF coil concept from our evaluation of tokamak-stellarator reactors because this approach is being investigated elsewhere and because it is beyond the scope of this report to address the above questions adequately. Similarly, we exclude the dragon configuration from our evaluation, since its physical characteristics are still largely unexplored. A figure-8 stellarator is an example of a dragon configuration, and a representative illustration the of the dragon magnetic geometry is given in Figure 2.3 . As with the twisted TF coil configuration, support requirements for a dragon configuration will be substantial.

2.4 Use of Superconducting Coils

The use of superconducting dipoles placed between the TF coils (in order to excite helical harmonics) does not appear to be feasible. From the expression for $\bar{\iota}$, we see that $\bar{\iota}$ is proportional to $1/N$ so long pitch lengths are most suited for adding transform. Also, the amount of added transform scales approximately with the square of the percentage of the complete (classical stellarator) winding

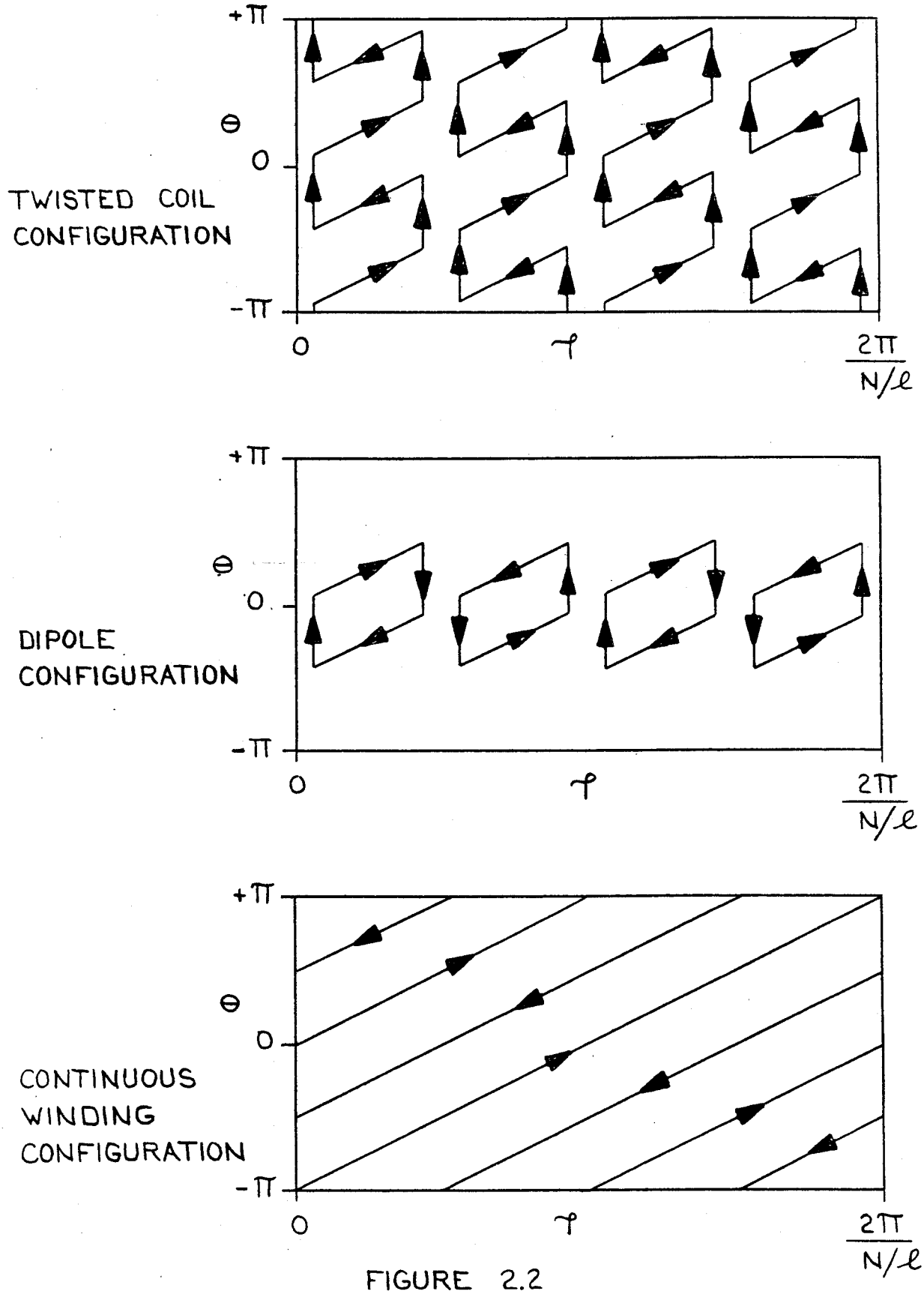

FIGURE 2.2

HELICAL COIL GEOMETRIES

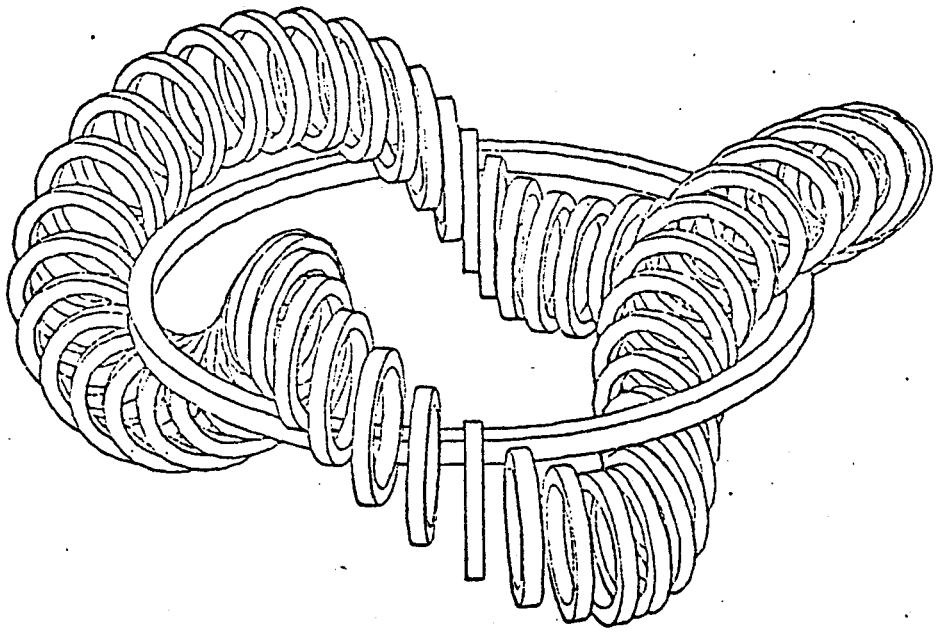

FIGURE 2.3
HELICAL AXIS ("DRAGON") COIL GEOMETRY

present. By placing the dipoles only on the outboard side and only between the toroidal coils, only about a third of the complete stellarator winding could be present. By comparing this to the base design given in Chapter IV, we can see that the dipole current would be in excess of 10 MA. This would result in an average force/length along the dipole of $>$ 50 MN/meter, and, more critically, result in an unbalanced torque on each dipole of $>$ 200 MN-meters. This torque is two orders of magnitude above what could reasonably be supported.

The placement of superconducting dipoles external to the TF coils and with complete coverage must also be discarded. Due to the increased distance from the plasma axis, the required helical current could again be in excess of 10 MA, with large torques and unbalanced forces due to the dipole–dipole interactions. In general, once the helical current becomes comparable to the toroidal field coil current, the twisted toroidal field coil geometry becomes more practical, since there is then no reason to have two separate coil systems.

The use of continuous helical windings (the classical stellarator winding configuration) precludes the use of superconducting helical coils, since fabrication and access problems with the superconducting helical and TF coils nested within each other made the reactor unfeasible. We therefore conclude that the resistive, continuously wound coils are the most appropriate choice for the helices in a tokamak-stellarator reactor. Resistive helical coils can be constructed with joints that facilitate mounting and demounting.

2.5 Resistive Magnet Design Options

We now decide whether to make the resistive, continuous, helical coils external or internal to the TF coil system. From the equation for $\bar{\iota}$, we see that, for $\ell = 2$, $\bar{\iota}$ scales as $r_{\text{coil}}^{-4} \cdot I_h^2$, so placing the coils external to the TF coils results in a large increase in helical current. In the base design, the internal helical coils have a minor radius of 2.50 meters, and $I_h = 2.91$ MA. If the helical coil minor radius were increased to 6 or 7 meters in order to be external to the TF coils, the helical current would be about 30 MA, the helical coil – helical coil interaction would be a factor of 100 greater than with the base design, and the amount of copper needed to make the associated resistive load of 10^{10} Amp-meters equal to $300\, MW_{\text{electric}}$ is 60 thousand tonnes. The reason the helical coils can not be located closer to the plasma is that the factor of ten increase in the helical current results in a factor of 100 increase in the cross–sectional area of the helical coils in order to maintain the same power dissipation. The large radial thickness of the coils (several meters) thus results in a large minor radius for the current centroid. Clearly the external coil design is not feasible.

2.6 Stellarator versus Torsatron Configurations

In a classical stellarator, there are 2 ℓ helical windings with the current in each winding in the reverse direction from the two nearest neighboring windings, and $I_1 = -I_2$. In a classical torsatron, there are ℓ helical windings with the currents flowing in the same direction, with $I_1 = I_h$ and $I_2 = 0$. The torsatron configuration has the following advantages:

1) The forces between the helical coils diminish if the coil pitch length is near $2\pi r_{coil}$.

2) The number of helical windings is half that of a stellarator configuration, hence there is increased access with the torsatron coils.

3) The torsatron windings add a net toroidal field so the toroidal field coil current can be reduced.

On the other hand, the stellarator configuration has these advantages:

1) The current per stellarator coil (for fixed $\bar{\iota}$) is half that of a torsatron coil, resulting in a 28% decrease in the peak bending stress on the coil support structure (see Chapter V).

2) There is no net magnetic dipole moment or net vertical field associated with the stellarator windings. Thus the current requirements for the equilibrium coils are less with a stellarator configuration.

3) There is some computational and experimental evidence[6] (comparing Wendelstein VII-A and Heliotron-E) that an $\ell = 2$ stellarator produces a slightly larger vacuum separatrix than an $\ell = 2$ torsatron, though separatrix size and elongation are strong functions of pitch length, helical current, and winding law, and the interrelationship of these parameters with the ratio I_1/I_2 remains largely unexplored.

In Chapter V, the forces between the helical coils and the toroidal field will be shown to be a dominant constraint in coil design, while the helical coil - helical coil forces are comparatively small and access does not appear to be a problem in $\ell = 2$ stellarator designs. Thus the stellarator current configuration (with $I_1 = -I_2$) was chosen as optimal.

One final option that remains to be considered is the use of resistive toroidal field coils in order to have the helical coils external to the toroidal field coils and still have the helical coils relatively close to the plasma surface. An analysis of this concept is given in Chapter IV, where the distance between the plasma surface and the helical coils was 1.5 meters. The analysis shows that a resistive tokamak–stellarator reactor would be at best a marginal machine, if optimistically low aspect ratios for the helical coils could be assumed.

References

1) P. A. Politzer Torsatron Design Memo 77-1; M.I.T. Department of Nuclear Engineering, 1977, Cambridge, Mass.

2) P. A. Politzer, et. al. Bulletin of the American Physical Society; 25, 8, October 1980 — paper 2R7; American Institute of Physics; New York, NY

3) J. Fujita, et. al. Proceedings of the Eighth International Conference Plasma Physics and Controlled Nuclear Fusion Research; Brussels, 1, p. 209, 1–10 July 1980, International Atomic Energy Agency, Vienna, Austria

4) T. K. Chu, et. al. Princeton Plasma Physics Laboratory No. PPPL–1796, 1981.

5) K. Ohasa and K. Miyamoto Jap. J. of Applied Physics 16, p. 813–816, May 1977.

6) Joint U.S.–Euratom Report Stellarators—Status and Future directions, p. 18–35, July 1981, Max-Planck-Institut für Plasmaphysik, -8046 Garching, F. R. Germany

Chapter III – Physics and Engineering Reactor Constraints

3.1 Physical and Engineering Constraints

We will now set the following physical and engineering constraints:

1. vacuum $\bar{\iota}$,
2. K_β ($\beta_l = K_\beta/A$),
3. B_{zo}, the toroidal field on axis,
4. $\mathcal{F}$, the dissipated magnet power/fusion power, and
5. $\mathcal{Q}$, the average force/meter on the helices,

and show that the additional choice of total fusion power determines all other reactor parameters (wall loading, margin of ignition, major radius, plasma and helical coil aspect ratios, helical current and current density).

Setting $\ell = 2$ and $I_1 = -I_2 = I_h$, the rotational transform $\bar{\iota}$ can be written as:

$$\bar{\iota} = \frac{4}{N}\left(\frac{1}{r_{\text{coil}}}\right)^4\left(\frac{\mu_o}{\pi}\frac{R_o I_h}{B_{zo}}\right)^2$$

There is both theoretical[1] and experimental[2] evidence that $\bar{\iota}$ should be $\simeq .15$ in order to prevent disruptive instabilities. Setting $\bar{\iota} = .15\ C_o$, the expression for $\bar{\iota}$ becomes

$$.48\sqrt{C_o N}\left(\frac{\text{MA}}{\text{tesla - meter}}\right) = \frac{I_h R_o}{B_{zo} r_{\text{coil}}^2}$$

3.2 Resistive Power Losses of Helical Coils

The coil shape should be chosen so as to minimize r_{coil} and the ohmic power loss. This implies that the percentage of toroidal surface area covered by the coils (f_o) should be as large as possible. From previous studies[1], it has been shown that the external transform begins to rapidly decrease when $f_o > 30\%$. We therefore pick $f_o = .3$ for the analysis. The helical coils are illustrated in Figure 3.1, and are defined to have a radial thickness t, a thickness perpendicular to r termed b, and a total length of:

$$\text{length} = 2\,\ell\,(S)\,2\pi R_o \sqrt{1 + \left(\frac{N}{\ell}\frac{r_{\text{coil}}}{R_o}\right)^2}$$

where S represents the extra length due to deviation from the sinusoidal winding law (S always $\geq$1). For the $\ell = 2$, low N cases considered in this study, we picked length $= 27\ R_o$ as the approximate length of all winding systems. The breadth of the coils (b) is :

$$\text{torus surface area} = 4\pi^2 r_{\text{coil}} R_o$$

$$f_o = .3 = \frac{\text{length} \cdot b}{4\pi^2 r_{\text{coil}} R_o}$$

$$b = .44\, r_{\text{coil}}$$

The resistivity of the coils ρ was approximated as $3 \cdot 10^{-8}$ ohm-meter, averaged over the copper conductor and cooling channels. The total resistance of the helical coils is then:

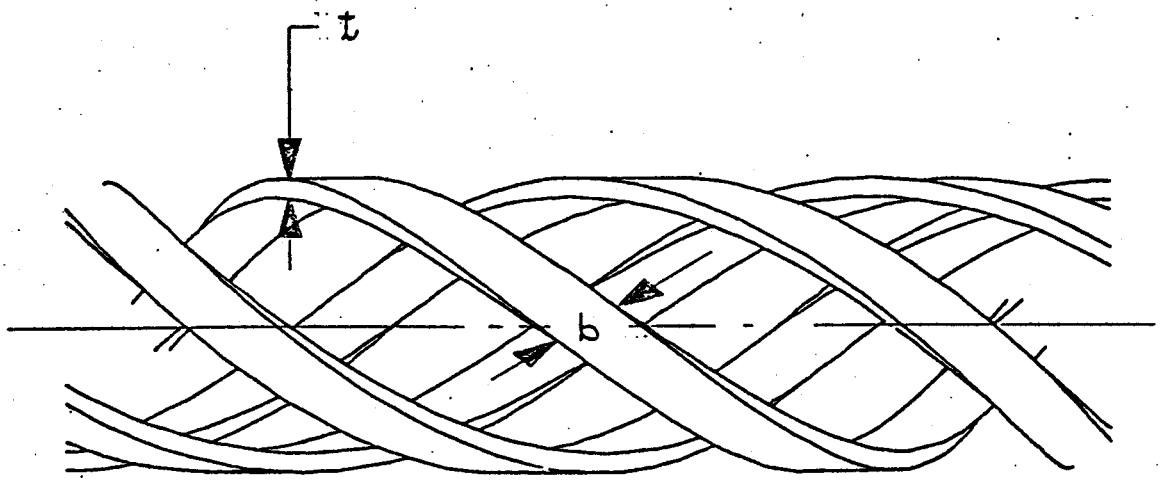

FIGURE 3.1
HELICAL COIL PARAMETERS

$$\text{Resistance} = \frac{\langle\rho\rangle \cdot \text{length}}{b \cdot t} = 1.841 \cdot 10^{-6} \text{ ohm–meters } \frac{R_o}{r_{\text{coil}}\, t}$$

The ohmic power dissipated in the magnets is:

$$\text{Dissipated Power} = I_h^2 \times \text{Resistance} = \left(.48\sqrt{C_o N}\frac{B_{zo} r_{\text{coil}}^2}{R_o}\right)^2 \times \text{Resistance}$$

$$= \frac{.424 C_o N B_{zo}^2 r_{\text{coil}}^3}{R_o t} \text{ MW}$$

3.3 Margin of Ignition and Constraints on β

The margin of ignition for a fusion reactor is defined as $\tau_{\text{emp}}/\tau_{\text{ign}}$. τ_{ign} is the energy confinement time required for ignition at a given temperature, where ignition is the state of a self sustaining plasma burn. τ_{emp} is the energy confinement time. For a tokamak it can be expressed by the empirical scaling law $\tau_{\text{emp}} \sim n a_p^2$. The margin of ignition (MI) for a tokamak reactor may be expressed as[4]:

$$\beta_i^2 B_{zo}^4 a_p^2 = 1.5 \cdot (MI)$$

with

$$\beta_t = \frac{K_\beta\, a_p}{R_o}$$

$a_p =$ minor radius of plasma

B_{zo} = toroidal field on axis

The maximum allowable value for K_β is determined by 1) the force balance between the plasma pressure and vertical field, and 2) the MHD activity that might arise between a high internal plasma transform and a low N number helical coil system. We now analyze both constraints.

There exists an outward force on the plasma loop due to the fact that there is more surface area on the outboard side of the plasma. This additional surface area may be expressed as:

$$\text{Area} = \int_o^{2\pi} d\phi \int_{\theta_1}^{\theta_2} R(\theta) a_p d\theta$$

with

$$R(\theta) = R_o + a_p \cos\theta$$

$$dr = a_p d\theta$$

The difference in area between the outboard side and inboard side is:

$$\Delta\text{Area} = 2\pi \int_{-\frac{\pi}{2}}^{\frac{\pi}{2}} a_p^2 \cos\theta d\theta - 2\pi \int_{\frac{\pi}{2}}^{\frac{3\pi}{2}} a_p^2 \cos\theta d\theta$$

$$= 8\pi a_p^2$$

The force balance between the plasma pressure and vertical field is:

$$\text{Force}_{total} = 2\pi R_o I_p B_{\text{vert}} = 8\pi a_p^2 \sum_j n_j k_b T_j$$

with

$$B_p = \frac{\mu_o I_p}{2\pi a_p}$$

$$\beta_p = \frac{\sum_j n_j k_b T_j}{B_p^2/2\mu_o}$$

Substituting, we obtain:

$$B_{\text{vert}} = \frac{a_p B_p}{\pi R_o} \beta_p$$

In addition, B_{vert} must balance the bursting force of the plasma current loop. B_{vert} must be much less than B_p so as not to unravel the rotational transform at the plasma edge. This sets a maximum pratical limit on β_p.[5]

Therefore:

$$\beta_p^{max} \leq \frac{R_o}{a_p}$$

$$K_\beta^{max} \leq (\iota^{\text{edge}})^2$$

There is a second constraint on K_β arising from the need to keep the plasma rotational transform less than the helical coil transform. This requirement can be expressed as:

$$\frac{N}{\ell} q^{\text{axis}} \geq M^*$$

where M^* is the safety factor necessary to supress MHD resonance behavior between the internal and external transform. The minimum acceptable value for M^* is unknown, but there is experimental and numerical data (which will be presented later in this report) that $M^*_{\text{minimum}} = 4$ to 6. Setting $N\, q^{\text{axis}} = \ell M^*$, we can express K_β as:

$$K_\beta \leq \left(\frac{q^{\text{axis}}}{q^{\text{edge}}}\right)^2_{\text{max}} \left(\frac{N^2}{\ell^2 M^{*2}}\right)$$

Picking as a practical maximum limit

$$\left(\frac{q^{\text{axis}}}{q^{\text{edge}}}\right)^2_{\text{max}} = .5,$$

the expression for K_β becomes:

$$K_\beta \leq \frac{1}{2}\left(\frac{N}{\ell M^*}\right)^2$$

for $N \leq \ell M^*$. For $N > \ell M^*$, K_β still has a maximum value $= .5$, otherwise the $q = 1$ surface approaches the plasma edge and Kruskol – Shafranov screw instabilities occur. Assuming the highest practical internal transforms ($q_{\text{axis}} \simeq 1$, $q_{\text{edge}} \simeq \sqrt{2}$), we get:

$$K_\beta = .5 \times \min\left(1, \left(\frac{N}{\ell M^*}\right)^2\right)$$

This equation shows that the optimum choice of N is: $N = \ell M^*$. Even though engineering problems are eased at lower N, the fusion power density is $\sim \beta^2 \sim K_\beta^2 \sim N^4$, and the sharp drop-off in power density for low N is the dominant consideration. For example, if $\ell M^* = 10$, an $N = 6$

system would have only 13% the fusion power density of an $N = 10$ system. This constraint will be analyzed in more detail in Chapter IV.

3.4 Reactor Power Balance

The primary fusion wall loading (assuming the plasma is operating at the pressure minimum for fixed power output, $T_i = 15$ KeV is (for $a_p \simeq a_{\text{wall}}$):

$$\text{Wall Loading (no multiplication in blanket)} \simeq (.64\beta_t^2 B_{zo}^4 a_p)\ \text{MW/m}^2 \qquad \text{[SI units]}$$

$$\simeq \frac{.96(MI)}{a_{\text{plasma}}}\ \text{MW/meter}$$

The total output of primary fusion power is:

$$P_{\text{thermal}} = 4\pi^2 R_o a_p \cdot \text{Wall Loading}$$

$$= 37.9 R_o (MI)\ \text{MW/meter}$$

The ratio of ohmic power dissipated in the helical coils divided by the primary thermal power ($\mathcal{F}$) is:

$$\mathcal{F} = \frac{.424\, C_o\, N\, B_{zo}^2\, r_{\text{coil}}^3 \,/\, (R_o\, t)}{37.9\, R_o\, (MI)}$$

For an economical reactor, $\mathcal{F}$ must be $\leq .1$, we thus present four constraints on the tokamak–stellarator reactor:

$$\bar{\iota} = .15C_o \qquad (C_o \simeq 1)$$

$$K_\beta = .5C_1 \qquad (C_1 \leq 1)$$

$$B_{zo} = 10 \text{ tesla } \cdot C_2 \qquad (C_2 \leq 1)$$

$$\mathcal{F} = .1C_3 \qquad (C_3 \leq 1)$$

Table 3.1 — Constraints on the tokamak–stellarator reactor

It is assumed that Nb_3Sn superconductor can produce up to 10 tesla at the plasma axis.

3.5 Constraints on Plasma and Helical Coil Minor Radii

The expression for $\mathcal{F}$ can be written as:

$$C_3 = \frac{11.2C_oNC_2^2r_{\text{coil}}^3}{R_o^2(MI)t}$$

The equation for (MI) may be written as:

$$\frac{C_1^2C_2^4a_p^4}{R_o^2} = .0006(MI)$$

We can eliminate the expression $R_o^2\ (MI)$ and get:

$$C_3 = \frac{.00672C_oNr_{\text{coil}}^3}{tC_1^2C_2^2a_p^4}$$

Setting $r_{\text{coil}} = a_p + \Delta S + \frac{1}{2}t$, (Where ΔS is the void and blanket thickness between the plasma edge and helical coil), we get:

$$A_o \equiv \left(\frac{.00672 C_o N}{t C_1^2 C_2^2 C_3}\right)^{1/4}$$

$$a_p = A_o r_{\text{coil}}^{3/4}$$

$$r_{\text{coil}} = A_o r_{\text{coil}}^{3/4} + (\Delta S + \frac{1}{2}t)$$

Thus, a_p and r_{coil} are set by the choices of ΔS and t. In this study, we picked the minimum value of $\Delta S = .8$ meter, allowing a .2m void and a .6m blanket between the first wall and helical coils for breeding and heat removal. The choice for coil radial thickness t will be shown to determine the total power output of the reactor. Smaller t increases dissipative power losses. For fixed $\mathcal{F}$, this implies an increase in fusion power.

3.6 Forces on Helical Coils and Constraints on Major Radius

The force per meter on the helical field due to the toroidal field is an important design consideration. This average force per meter can be expressed as:

$$< F/\text{meter} >= I_h B_{zo} \sin(\text{pitch angle})$$

This force is primarily in the minor radius direction, radially outward for the helical windings carrying current in the direction of B_{zo}, and radially inward for the opposing pair of helical windings carrying current in the opposite toroidal direction. The pitch angle is the angle between the direction of the helical current and the toroidal direction.

$$\frac{F}{\text{meter}} = \frac{I_h B_{zo}}{\sqrt{1 + \left(\frac{R_o \ell}{r_{coil} N}\right)^2}}$$

The maximum allowable force/meter is set by structural support requirements. The torques on the helices are large, and must be supported externally. In our parameter scans we will examine systems from 2 to 16 MN/meter, with the base design having a load of 10 MN/meter.

We thus have:

$$\mathfrak{Q} \equiv \langle \text{force/length} \rangle = 4 \frac{\text{MN}}{\text{meter}} \cdot C_4 = I_h B_{zo} \sin(\text{pitch angle})$$

Substituting, we obtain:

$$R_o^2 + R_o^4 \left(\frac{\ell}{r_{\text{coil}} N}\right)^2 = 144 C_o N C_2^4 r_{\text{coil}}^4 / C_4^2$$

$$A_r \equiv \left(\frac{\ell}{r_{\text{coil}} N}\right)^2$$

$$C_r \equiv \frac{144 C_o N C_2^4 r_{\text{coil}}^4}{C_4^2}$$

$$R_o = \sqrt{\frac{\sqrt{1+4A_rC_r}-1}{2A_r}}$$

3.7 Summary

It can now be seen that the choices for $\bar{\iota}$, K_β, B_{zo}, $\mathcal{F}$, $\mathcal{Q}$, and t (the helical coil radial thickness) determine the following reactor parameters:

1) wall loading,

2) margin of ignition,

3) major radius,

4) plasma minor radius,

5) helical coil minor radius,

6) helical current,

7) helical current density, and

8) total fusion power.

At constant $\mathcal{F}$, the total fusion power is approximately proportional to $1/t$, so we can replace t with P_{th} in the list of constraints needed to determine the reactor parameters. In Chapter IV, we will pick a set of constraints that result in an attractive power reactor, and illustrate how changes in each of the constraints affect the reactor design.

References

1) P. A. Politzer, et. al. Bulletin of the American Physical Society; 25, 8, October 1980 — paper 2R7; American Institute of Physics; New York, NY

2) J. Fujita, et. al. Proceedings of the Eighth International Conference Plasma Physics and Controlled Nuclear Fusion Research; Brussels, 1, p. 209, 1–10 July 1980, International Atomic Energy Agency, Vienna, Austria

3) R. E. Potok, et. al. M.I.T. Plasma Fusion Center Report PFC/RR–80–15, 1981.

4) D. R. Cohn, et. al. M.I.T. Plasma Fusion Center Report PFC/RR–79–2, 1979.

5) Glenn Bateman MHD Instabilities, p. 163, 1978, The MIT Press, Cambridge, Massachusetts

Chapter IV – Parametric Scans

4.1 Physical Assumptions

In order to get an attractive base design for the tokamak-stellarator reactor, the following optimistic assumptions were required:

1) $K_\beta = .5$ (a factor ≥ 2 above current tokamak reactor designs (e.g. in STARFIRE[1], $K_\beta = .19$)). We assume that the addition of external transform will enable the reactor to operate at a very high total transform ($q^{\text{edge}} = 1.4$).

2) We assume flat profiles of temperature and density within the plasma volume. While the peaking of β at the plasma axis will result in an enhancement of the fusion power, the elongation and helical shaping of the plasma flux surfaces will result in a smaller plasma radius and thermal power output. We assume these effects approximately cancel each other.

3) $M^* = 4$ (M^* = ratio of helical winding transform/plasma transform). As will be shown in Chapter VI, current experiments on JIPP-T-II show $M^*_{\text{minimum}} \simeq 5$ for no MHD disruptions, and a numerical analysis shows $M_{\text{minimum}} \simeq 3$ for no island formation and no ergodic field lines near the plasma axis.

4) $\langle \mathcal{Q} \rangle = 10$ MN/meter. The bending stress imposes the most severe constraint on the support structure, and is approximately proportional to $\langle \mathcal{Q} \rangle$. This stress is transmitted to a ring support system external to the helical coils, which must be sufficiently rigid in order to withstand the

elliptical deformation.

5) $\bar{\iota}^{external} = .1$. This is the lower limit (both theoretically and experimentally) for the external transform to be an effective control of plasma MHD instabilities. Tables 4.3 and 4.4 show the changes in the reactor parameters that would occur if $\bar{\iota}^{external} = .15$ were required, rather than $\bar{\iota}^{external} = .1$.

4.2 Description of Base Design

In the optimal base design, we set $\bar{\iota}^{vacuum} = .1, \langle \mathbb{Q} \rangle = 10$ MN/meter, $K_\beta = .5, M^* = 4$, and set the wall loading by using the optimization algorithim shown in Figure 4.1 . This results in a base design with $B_{zo} = 6$ tesla, $\mathcal{F} = .08, P_{th}^{primary} = 3000$ MW, and a primary wall loading of 3.50 MW/m^2.

The major radius of the base design is 14.31 m. STARFIRE, which has a comparable wall loading and a primary thermal power $\simeq$ 3500 MW, has as its characteristic machine dimensions for its reactor envelope a height of 28.6 m and a diameter of 33 m. The power to system volume ratio is about 300 KW$_{th}$/m^3. The power to volume ratio of the tokamak-stellarator is about 250 KW$_{th}$/m^3. This value could be raised by decreasing the percentage volume of the helical support system, which would occur with an increase in R_o. A general finding of this study is that the cost per kilowatt remains acceptable as R_o is increased, but the total fusion power rises rapidly to unacceptably large values ($P_{th} > 5000$ MW). With constant wall loading, K_β, and B_{zo}, we find that P_{th} is proportional to $R_o^{5/3}$, so the range in R_o that is of reactor interest is limited to $R_o \leq 25$ meters.

Table 4.1 shows the variations in major radius R_o, the wall loading, and K_β as N is varied (keeping $M^* = 4$, $P_{th} = 3000$ MW, $\bar{\iota} = .1$, and $\mathbb{Q} = 10$ MN/m). It is instructive to see how it is not possible to lower both N and K_β in order to reduce R_o. The sharp drop in K_β results in a net loss in wall loading and a larger R_o. The scaling of $K_\beta \simeq N^2$ (for $N/\ell > M^*$) shows that the optimum choice for N is:

$$N = \ell M^*,$$

agreeing with the argument presented in the preceeding section.

N	K_β	R_o	Wall Loading
11	.5	19.82 m	2.33 MW/m^2
10	.5	17.97 m	2.63 MW/m^2
9	.5	16.13 m	3.01 MW/m^2
8	.5	14.31 m	3.50 MW/m^2
7	.383	15.29 m	2.82 MW/m^2
6	.281	16.70 m	2.16 MW/m^2
5	.195	18.79 m	1.55 MW/m^2

Table 4.1 — Parametric Scan of N versus R_o

Tables 4.2A to 4.2G illustrate the changes in the base design that would occur with the change of each constraint. The quantity $h + 2t_p$ is the radial thickness of a representative helical coil support structure needed to support the bending stresses. An analysis of the support structure requirements is given in Chapter V. Tables 4.2A to 4.2G also illustrate that there is the sharp drop in the wall

loading for decreases in K_β, $\langle \mathbb{Q} \rangle$, P_{th}, and $1/M^*$. Failure to meet any of their values in the base design would have a large detrimental effect on reactor viability.

The parametric scans also show the the required value of external transform has a large effect on the wall loading and major radius (see Table 4.2A). If a tokamak–stellarator reactor were ever built, it would be worthwhile not to add more external transform than was necessary.

Table 4.2B, along with Table 4.1, shows that the $K_\beta = .5$ regime must be reached for the tokamak–stellarator reactor to become attractive. If the current tokamak design parameter of $K_\beta = .2$ were used, the tokamak–stellarator would have a larger major radius and a much lower wall loading.

Table 4.2C shows that the major radius can be decreased by lowering the toroidal field, the main disadvantage being a decrease in the wall loading. If the base design had an axis field of 4 tesla rather than 6 tesla, the major radius would be reduced by 9.85%, while the wall loading would be reduced by 24.3%.

Table 4.2D shows that a higher ohmic loss in the helical coils will decrease the major radius. If the ohmic loss were increased from 240 MW to 360 MW, the major radius would decrease by 5.6%.

Table 4.2E shows that wall loading, major radius, and margin of ignition all scale favorably with an increase in $\mathbb{Q}$. Several additional force loads (such as the helical coil – helical coil interaction) have been optimistically neglected, so the $\mathbb{Q} = 10$ MN/m limit is probably a reasonable one. The force requirements are discussed in detail in Chapter V.

Table 4.2F shows that the major radius is near its minimum for $P_{th} = 3000$ MW, and the associated wall loading is acceptably large.

Table 4.2G shows how critically the reactor parameters depend on M^*. If $M^* = 6$ (rather than $M^* = 4$) were necessary, the major radius would increase by 52%, the margin of ignition would decrease by 34%, and the wall loading would decrease by 41%.

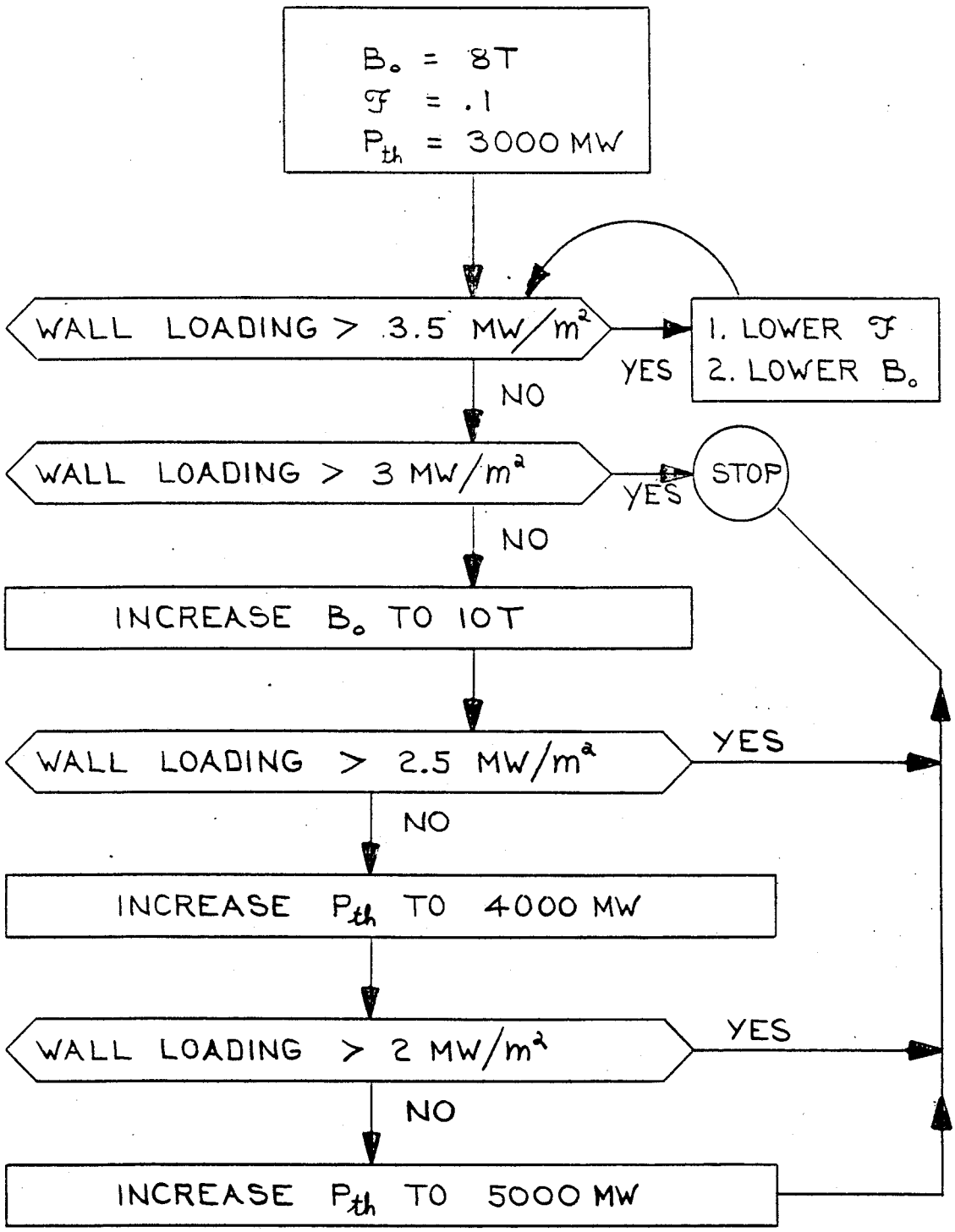

FIGURE 4.1

OPTIMIZATION ALGORITHIM USED IN PARAMETRIC SCANS

Constraints					
$\bar{\iota}_{external}$	.05	.075	.1	.15	.2
K_β			.5		
B_{zo} (tesla)			6		
$\mathfrak{F}$			.08		
$\mathfrak{Q}$ (MN/m)			10		
$P_{th}^{primary}$ (MW)			3000		
N , M^*			8 , 4		
Parameters					
margin of ignition	7.93	6.44	5.53	4.42	3.71
wall loading (MW/m^2)	5.48	4.23	3.50	2.64	2.12
t (meters)	.201	.284	.367	.536	.717
a_{plasma} (meters)	1.39	1.46	1.52	1.61	1.68
r_{coil} (meters)	2.29	2.40	2.50	2.67	2.84
R_o (meters)	9.99	12.30	14.31	17.92	21.32
I_{helix} (MA)	2.47	2.71	2.91	3.25	3.55
$\langle j \rangle_{helix}$ (A/cm^2)	1219	902	721	515	397
$h + 2\,t_p$ (meters)	1.02	1.01	1.02	1.04	1.08

Table 4.2A — Parametric Scan of $\bar{\iota}$

Constraints					
$\bar{\iota}_{external}$			.1		
K_β	.281	.383	.5	.633	.781
B_{zo} (tesla)			6		
$\mathcal{F}$			.08		
$\mathcal{Q}$ (MN/m)			10		
$P_{th}^{primary}$ (MW)			3000		
N , M^*	6 , 4	7 , 4	8 , 4	9 , 4	10 , 4
Parameters					
margin of ignition	4.74	5.18	5.53	5.83	6.07
wall loading (MW/m^2)	2.16	2.82	3.50	4.20	4.91
t (meters)	.465	.406	.367	.338	.317
a_{plasma} (meters)	2.11	1.76	1.52	1.33	1.19
r_{coil} (meters)	3.14	2.77	2.50	2.30	2.15
R_o (meters)	16.70	15.29	14.31	13.59	13.05
I_{helix} (MA)	3.39	3.12	2.91	2.75	2.62
$\langle j \rangle_{helix}$ (A/cm^2)	529	630	721	804	877
$h + 2\,t_p$ (meters)	1.22	1.10	1.02	.95	.89

Table 4.2B — Parametric Scan of K_β

Constraints					
$\bar{\iota}_{external}$			.1		
K_β			.5		
B_{zo} (tesla)	4	5	6	7	8
$\mathcal{F}$			.08		
$\mathcal{Q}$ (MN/m)			10		
$P_{th}^{primary}$ (MW)			3000		
N , M^*			8 , 4		
Parameters					
margin of ignition	6.14	5.82	5.53	5.26	5.01
wall loading (MW/m^2)	2.65	3.10	3.50	3.83	4.12
t (meters)	.382	.369	.367	.370	.378
a_{plasma} (meters)	2.22	1.80	1.52	1.32	1.17
r_{coil} (meters)	3.21	2.78	2.50	2.30	2.16
R_o (meters)	12.90	13.60	14.31	15.04	15.80
I_{helix} (MA)	3.54	3.16	2.91	2.74	2.61
$\langle j \rangle_{helix}$ (A/cm^2)	657	699	721	729	728
$h + 2\,t_p$ (meters)	1.36	1.14	1.02	.93	.87

Table 4.2C — Parametric Scan of B_{zo}

Constraints					
$\iota_{external}$			.1		
K_β			.5		
B_{zo} (tesla)			6		
$\mathcal{F}$	.04	.06	.08	.1	.12
$\mathcal{Q}$ (MN/m)			10		
$P_{th}^{primary}$ (MW)			3000		
N , M^*			8 , 4		
Parameters					
margin of ignition	4.54	5.20	5.53	5.73	5.86
wall loading (MW/m^2)	2.73	3.24	3.50	3.65	3.76
t (meters)	.872	.516	.367	.284	.232
a_{plasma} (meters)	1.60	1.54	1.52	1.51	1.50
r_{coil} (meters)	2.83	2.60	2.50	2.45	2.41
R_o (meters)	17.43	15.22	14.31	13.82	13.51
I_{helix} (MA)	3.06	2.95	2.91	2.88	2.87
$\langle j \rangle_{helix}$ (A/cm^2)	282	501	721	942	1163
$h + 2\,t_p$ (meters)	1.15	1.05	1.02	.99	.98

Table 4.2D — Parametric Scan of $\mathcal{F}$

Constraints					
$\bar{\iota}_{external}$			.1		
K_β			.5		
B_{zo} (tesla)			6		
$\mathcal{F}$			.08		
$\mathcal{Q}$ (MN/m)	4	7	10	13	16
$P_{th}^{primary}$ (MW)			3000		
N , M^*			8 , 4		
Parameters					
margin of ignition	2.93	4.30	5.53	6.68	7.77
wall loading (MW/m^2)	1.58	2.55	3.50	4.43	5.35
t (meters)	.245	.310	.367	.420	.473
a_{plasma} (meters)	1.78	1.62	1.52	1.45	1.39
r_{coil} (meters)	2.70	2.57	2.50	2.46	2.43
R_o (meters)	27.05	18.40	14.31	11.85	10.18
I_{helix} (MA)	1.80	2.39	2.91	3.39	3.86
$\langle j \rangle_{helix}$ (A/cm^2)	618	682	721	747	764
$h + 2\,t_p$ (meters)	.47	.72	1.02	1.34	1.72

Table 4.2E — Parametric Scan of $\mathcal{Q}$

Constraints					
$\bar{\iota}_{external}$			.1		
K_β			.5		
B_{zo} (tesla)			6		
$\mathcal{F}$			.08		
$\mathcal{Q}$ (MN/m)			10		
$P_{th}^{primary}$ (MW)	1000	2000	3000	4000	5000
N , M^*			8 , 4		
Parameters					
margin of ignition	1.84	3.90	5.53	6.92	8.15
wall loading (MW/m^2)	1.53	2.77	3.50	4.01	4.40
t (meters)	1.10	.523	.367	.291	.245
a_{plasma} (meters)	1.15	1.35	1.52	1.66	1.78
r_{coil} (meters)	2.51	2.41	2.50	2.60	2.70
R_o (meters)	14.34	13.52	14.31	15.25	16.18
I_{helix} (MA)	2.91	2.87	2.91	2.96	3.00
$\langle j \rangle_{helix}$ (A/cm^2)	240	516	721	888	1031
$h + 2\,t_p$ (meters)	1.11	1.02	1.02	1.02	1.04

Table 4.2F — Parametric Scan of P_{th}

Constraints					
$\bar{\iota}_{external}$			.1		
K_β			.5		
B_{zo} (tesla)			6		
$\mathcal{F}$			.08		
$\mathcal{Q}$ (MN/m)			10		
$P_{th}^{primary}$ (MW)			3000		
N , M^*	4 , 2	6 , 3	8 , 4	10 , 5	12 , 6
Parameters					
margin of ignition	11.05	7.39	5.53	4.41	3.65
wall loading (MW/m^2)	8.30	5.02	3.50	2.63	2.08
t (meters)	.250	.311	.367	.417	0.465
a_{plasma} (meters)	1.28	1.41	1.52	1.61	1.68
r_{coil} (meters)	2.20	2.37	2.50	2.62	2.72
R_o (meters)	7.17	10.71	14.31	17.97	21.68
I_{helix} (MA)	3.18	3.02	2.91	2.83	2.77
$\langle j \rangle_{helix}$ (Λ/cm^2)	1316	929	721	590	499
$h + 2\,t_p$ (meters)	.88	.96	1.02	1.07	1.11

Table 4.2G — Parametric Scan of N , M^*

4.3 Helical Coil Transform and Support Requirements

In Tables 4.3A to 4.3K we show how the optimal design would change for different values of $\langle \mathfrak{Q} \rangle$ and M^*, if an external transform of .1 were necessary. Tables 4.4A to 4.4K show a similar parametric scan for an external transform of .15 . The algorithim used to optimize each case of the parameter scans is described in Figure 4.1 . M^* is varied from 1 to 6, and ⟨force/meter⟩ on the helices is varied from 2 MN/m to 16 MN/m. The primary result is that the attractiveness of the base design is strongly dependent on achieving $M^* = 4$ and $\langle \mathfrak{Q} \rangle = 10$ MN/m, and a failure to meet these requirements will result in a much larger reactor size and a large decrease in the wall loading. For example, if $M^* = 6$, $\bar{\iota} = .15$, and $\mathfrak{Q} = 8$ MN/m were necessary for the base design (rather than $M^* = 2$, $\bar{\iota} = .1$, and $\mathfrak{Q} = 10$ MN/m), the major radius would increase 151%, to 35.87 meters. A major goal in the tokamak-stellarator design is to raise the wall loading to a regime of economic interest (2 – 3.5 MW/m^2) while still keeping the major radius and total fusion power acceptably small ($R_o \leq 20$ m and $P_{th} \leq 4000$ MW$_{th}$). The scalings of the optimized major radius R_o and margin of ignition versus $\mathfrak{Q}$ and M^* are illustrated in Figures 4.2 to 4.5 . Further experiments with tokamak-stellarator devices at low $M^*(M^* = 4$ to 5) are needed to ascertain if such a goal is realizable.

Constraints		
$\bar{\iota}_{external}$	.15	.15
K_β	.5	.5
B_{zo} (tesla)	5	3
$\mathcal{F}$	.05	.035
$\mathcal{Q}$ (MN/m)	2	4
$P_{th}^{primary}$ (MW)	3000	3000
N , M^*	2 , 1	2 , 1
Parameters		
margin of ignition	6.30	9.56
wall loading (MW/m^2)	3.43	3.46
t (meters)	.211	.426
a_{plasma} (meters)	1.76	2.65
r_{coil} (meters)	2.67	3.66
R_o (meters)	12.57	8.28
I_{helix} (MA)	1.92	3.30
$\langle j \rangle_{helix}$ (A/cm^2)	776	481
$h + 2\,t_p$ (meters)	.30	.58

Table 4.3A — Optimal Reactor Parameters for $\bar{\iota} = .15$ and $M^* = 1$

Constraints			
$\bar{\iota}_{external}$	.15	.15	.15
K_β	.5	.5	.5
B_{zo} (tesla)	8	5	3
$\mathcal{F}$	.1	.04	.03
$\mathcal{Q}$ (MN/m)	2	4	8
$P_{th}^{primary}$ (MW)	3000	3000	3000
N , M^*	3 , 1.5	3 , 1.5	3 , 1.5
Parameters			
margin of ignition	4.19	6.23	9.63
wall loading (MW/m^2)	3.30	3.38	3.50
t (meters)	.129	.449	.903
a_{plasma} (meters)	1.22	1.77	2.64
r_{coil} (meters)	2.09	2.55	3.90
R_o (meters)	18.89	12.70	8.22
I_{helix} (MA)	1.53	2.55	4.60
$\langle j \rangle_{helix}$ (A/cm^2)	1298	463	297
$h + 2\,t_p$ (meters)	.27	.45	1.20

Table 4.3B — Optimal Reactor Parameters for $\bar{\iota} = .15$ and $M^* = 1.5$

Constraints			
$\bar{\iota}_{external}$	.15	.15	.15
K_β	.5	.5	.5
B_{zo} (tesla)	10	8	4
$\mathcal{F}$	.1	.05	.045
$\mathcal{Q}$ (MN/m)	2	4	8
$P_{th}^{primary}$ (MW)	3000	3000	3000
N , M^*	4 , 2	4 , 2	4 , 2
Parameters			
margin of ignition	3.01	4.36	7.56
wall loading (MW/m^2)	2.72	3.47	3.45
t (meters)	.155	.434	.636
a_{plasma} (meters)	1.06	1.21	2.11
r_{coil} (meters)	1.94	2.23	3.22
R_o (meters)	26.29	18.13	10.47
I_{helix} (MA)	1.37	2.10	3.81
$\langle j \rangle_{helix}$ (A/cm^2)	1041	493	423
$h + 2\,t_p$ (meters)	.26	.42	.99

Table 4.3C — Optimal Reactor Parameters for $\bar{\iota} = .15$ and $M^* = 2$

Constraints				
$\bar{\iota}_{external}$	.15	.15	.15	.15
K_β	.5	.5	.5	.5
B_{zo} (tesla)	10	8	5	2.8
$\mathcal{F}$	.1	.1	.07	.04
$\mathcal{Q}$ (MN/m)	2	4	8	16
$P_{th}^{primary}$ (MW)	4000	3000	3000	3000
N , M^*	5 , 2.5	5 , 2.5	5 , 2.5	5 , 2.5
Parameters				
margin of ignition	3.03	3.89	6.32	10.14
wall loading (MW/m^2)	2.38	3.00	3.44	3.48
t (meters)	.137	.219	.425	1.379
a_{plasma} (meters)	1.22	1.24	1.76	2.80
r_{coil} (meters)	2.09	2.15	2.78	4.29
R_o (meters)	34.85	20.36	12.52	7.81
I_{helix} (MA)	1.35	1.96	3.30	7.07
$\langle j \rangle_{helix}$ (A/cm^2)	1065	943	636	272
$h + 2\,t_p$ (meters)	.27	.50	.86	3.15

Table 4.3D — Optimal Reactor Parameters for $\bar{\iota} = .15$ and $M^* = 2.5$

Constraints				
$\bar{\iota}_{external}$	.15	.15	.15	.15
K_β	.5	.5	.5	.5
B_{zo} (tesla)	10	10	7	3
$\mathcal{F}$	.1	.1	.07	.06
$\mathcal{Q}$ (MN/m)	2	4	8	16
$P_{th}^{primary}$ (MW)	5000	3000	3000	3000
N , M^*	6 , 3	6 , 3	6 , 3	6 , 3
Parameters				
margin of ignition	2.99	3.06	4.81	9.64
wall loading (MW/m^2)	2.09	2.78	3.43	3.50
t (meters)	.127	.252	.487	.904
a_{plasma} (meters)	1.37	1.06	1.35	2.64
r_{coil} (meters)	2.24	1.98	2.39	3.90
R_o (meters)	44.13	25.88	16.46	8.21
I_{helix} (MA)	1.33	1.79	2.86	6.52
$\langle j \rangle_{helix}$ (A/cm^2)	1064	812	558	421
$h + 2\,t_p$ (meters)	.27	.38	.76	2.95

Table 4.3E — Optimal Reactor Parameters for $\bar{\iota} = .15$ and $M^* = 3$

Constraints				
$\bar{\iota}_{external}$	.15	.15	.15	.15
K_β	.5	.5	.5	.5
B_{zo} (tesla)	10	10	8	4.5
$\mathfrak{F}$	.1	.1	.1	.06
$\mathfrak{Q}$ (MN/m)	2	4	8	16
$P_{th}^{primary}$ (MW)	5000	4000	3000	3000
N , M^*	7 , 3.5	7 , 3.5	7 , 3.5	7 , 3.5
Parameters				
margin of ignition	2.56	3.33	4.25	6.98
wall loading (MW/m^2)	1.72	2.68	3.35	3.50
t (meters)	.137	.215	.354	.931
a_{plasma} (meters)	1.43	1.19	1.22	1.91
r_{coil} (meters)	2.29	2.10	2.19	3.18
R_o (meters)	51.51	31.70	18.63	11.35
I_{helix} (MA)	1.30	1.77	2.62	5.08
$\langle j \rangle_{helix}$ (A/cm^2)	935	892	768	391
$h + 2\,t_p$ (meters)	.28	.39	.70	2.16

Table 4.3F — Optimal Reactor Parameters for $\bar{\iota} = .15$ and $M^* = 3.5$

Constraints				
$\bar{\iota}_{external}$	.15	.15	.15	.15
K_β	.5	.5	.5	.5
B_{zo} (tesla)	10	10	9	7
$\mathcal{F}$	.1	.1	.1	.061
$\mathcal{Q}$ (MN/m)	2	4	8	16
$P_{th}^{primary}$ (MW)	5000	4000	3000	3000
N , M^*	8 , 4	8 , 4	8 , 4	8 , 4
Parameters				
margin of ignition	2.24	2.91	3.56	4.87
wall loading (MW/m^2)	1.46	2.26	3.03	3.48
t (meters)	.147	.230	.391	1.048
a_{plasma} (meters)	1.47	1.23	1.13	1.34
r_{coil} (meters)	2.35	2.15	2.13	2.67
R_o (meters)	58.92	36.23	22.20	16.24
I_{helix} (MA)	1.27	1.73	2.49	4.16
$\langle j \rangle_{helix}$ (A/cm^2)	835	797	680	339
$h + 2\,t_p$ (meters)	.28	.40	.68	1.71

Table 4.3G — Optimal Reactor Parameters for $\bar{\iota} = .15$ and $M^* = 4$

Constraints				
$\bar{\iota}_{external}$	.15	.15	.15	.15
K_β	.5	.5	.5	.5
B_{zo} (tesla)	10	10	10	7
$\mathcal{F}$	.1	.1	.1	.08
$\mathcal{Q}$ (MN/m)	2	4	8	16
$P_{lh}^{primary}$ (MW)	5000	5000	3000	3000
N , M^*	9 , 4.5	9 , 4.5	9 , 4.5	9 , 4.5
Parameters				
margin of ignition	2.00	3.13	3.04	4.90
wall loading (MW/m^2)	1.14	2.00	2.75	3.50
t (meters)	.156	.202	.429	.766
a_{plasma} (meters)	1.69	1.51	1.06	1.34
r_{coil} (meters)	2.56	2.41	2.07	2.52
R_o (meters)	65.99	42.12	26.07	16.17
I_{helix} (MA)	1.29	1.78	2.37	3.98
$\langle j \rangle_{helix}$ (A/cm^2)	734	832	606	467
$h + 2\,t_p$ (meters)	.29	.42	.67	1.63

Table 4.3H — Optimal Reactor Parameters for $\bar{\iota} = .15$ and $M^* = 4.5$

Constraints				
$\bar{\iota}_{external}$	.15	.15	.15	.15
K_β	.5	.5	.5	.5
B_{zo} (tesla)	10	10	10	8
$\mathcal{F}$	.1	.1	.1	.095
$\mathcal{Q}$ (MN/m)	2	4	8	16
$P_{th}^{primary}$ (MW)	5000	5000	4000	3000
N , M^*	10 , 5	10 , 5	10 , 5	10 , 5
Parameters				
margin of ignition	1.79	2.78	3.54	4.38
wall loading (MW/m^2)	1.10	1.91	2.89	3.48
t (meters)	.165	.216	.349	.667
a_{plasma} (meters)	1.56	1.40	1.18	1.21
r_{coil} (meters)	2.44	2.31	2.15	2.34
R_o (meters)	73.89	47.54	29.80	18.08
I_{helix} (MA)	1.23	1.70	2.36	3.68
$\langle j \rangle_{helix}$ (A/cm^2)	690	775	713	536
$h + 2\,t_p$ (meters)	.28	.41	.68	1.50

Table 4.3I — Optimal Reactor Parameters for $\bar{\iota} = .15$ and $M^* = 5$

Constraints				
$\bar{\iota}_{external}$	.15	.15	.15	.15
K_β	.5	.5	.5	.5
B_{zo} (tesla)	10	10	10	8
$\mathcal{F}$	.1	.1	.1	.1
$\mathcal{Q}$ (MN/m)	2	4	8	16
$P_{th}^{primary}$ (MW)	5000	5000	4000	3000
N , M^*	11 , 5.5	11 , 5.5	11 , 5.5	11 , 5.5
Parameters				
margin of ignition	1.62	2.52	3.21	4.03
wall loading (MW/m^2)	0.97	1.69	2.56	3.14
t (meters)	.174	.227	.368	.660
a_{plasma} (meters)	1.61	1.43	1.20	1.23
r_{coil} (meters)	2.49	2.35	2.19	2.36
R_o (meters)	81.44	52.36	32.82	19.62
I_{helix} (MA)	1.21	1.67	2.32	3.62
$\langle j \rangle_{helix}$ (A/cm^2)	636	714	656	528
$h + 2\,t_p$ (meters)	.29	.42	.69	1.52

Table 4.3J — Optimal Reactor Parameters for $\bar{\iota} = .15$ and $M^* = 5.5$

Constraints				
$\bar{\iota}_{external}$	.15	.15	.15	.15
K_β	.5	.5	.5	.5
B_{zo} (tesla)	10	10	10	10
$\mathcal{F}$	.1	.1	.1	.1
$\mathcal{Q}$ (MN/m)	2	4	8	16
$P_{th}^{primary}$ (MW)	5000	5000	4000	3000
N , M^*	12 , 6	12 , 6	12 , 6	12 , 6
Parameters				
margin of ignition	1.48	2.31	2.94	3.25
wall loading (MW/m^2)	0.87	1.51	2.29	3.00
t (meters)	.182	.238	.386	.745
a_{plasma} (meters)	1.63	1.46	1.23	1.04
r_{coil} (meters)	2.53	2.38	2.22	2.21
R_o (meters)	89.02	57.21	35.87	24.37
I_{helix} (MA)	1.19	1.65	2.29	3.34
$\langle j \rangle_{helix}$ (A/cm^2)	590	663	608	461
$h + 2\,t_p$ (meters)	.29	.42	.70	1.40

Table 4.3K — Optimal Reactor Parameters for $\bar{\iota} = .15$ and $M^* = 6$

Constraints		
$\bar{\iota}_{external}$	.1	.1
K_β	.5	.5
B_{zo} (tesla)	4.3	2.4
$\mathfrak{F}$	.03	.03
$\mathfrak{Q}$ (MN/m)	2	4
$P_{th}^{primary}$ (MW)	3000	3000
N , M^*	2 , 1	2 , 1
Parameters		
margin of ignition	7.14	11.25
wall loading (MW/m^2)	3.45	3.40
t (meters)	.256	.366
a_{plasma} (meters)	1.99	3.18
r_{coil} (meters)	2.92	4.16
R_o (meters)	11.09	7.04
I_{helix} (MA)	1.83	3.27
$\langle j \rangle_{helix}$ (A/cm^2)	556	489
$h + 2\,t_p$ (meters)	.31	.66

Table 4.4A — Optimal Reactor Parameters for $\bar{\iota} = .1$ and $M^* = 1$

Constraints			
$\bar{\iota}_{external}$	.1	.1	.1
K_β	.5	.5	.5
B_{zo} (tesla)	7	4	2
$\mathcal{F}$	.06	.04	.03
$\mathcal{Q}$ (MN/m)	2	4	8
$P_{th}^{primary}$ (MW)	3000	3000	3000
N , M^*	3 , 1.5	3 , 1.5	3 , 1.5
Parameters			
margin of ignition	4.83	7.70	13.11
wall loading (MW/m^2)	3.44	3.52	3.43
t (meters)	.153	.308	.688
a_{plasma} (meters)	1.35	2.10	3.67
r_{coil} (meters)	2.22	3.05	4.82
R_o (meters)	16.39	10.28	6.04
I_{helix} (MA)	1.43	2.46	5.21
$\langle j \rangle_{helix}$ (A/cm^2)	959	594	358
$h + 2\,t_p$ (meters)	.27	.51	1.66

Table 4.4B — Optimal Reactor Parameters for $\bar{\iota} = .1$ and $M^* = 1.5$

Constraints			
$\bar{\iota}_{external}$	.1	.1	.1
K_β	.5	.5	.5
B_{zo} (tesla)	9	6	3.2
$\mathcal{F}$	.1	.04	.03
$\mathcal{Q}$ (MN/m)	2	4	8
$P_{th}^{primary}$ (MW)	3000	3000	3000
N , M^*	4 , 2	4 , 2	4 , 2
Parameters			
margin of ignition	3.59	5.43	9.05
wall loading (MW/m^2)	3.06	3.45	3.45
t (meters)	.106	.363	.723
a_{plasma} (meters)	1.13	1.52	2.52
r_{coil} (meters)	1.98	2.50	3.68
R_o (meters)	22.04	14.47	8.74
I_{helix} (MA)	1.26	2.04	3.88
$\langle j \rangle_{helix}$ (A/cm^2)	1355	509	332
$h + 2\,t_p$ (meters)	.26	.55	1.20

Table 4.4C — Optimal Reactor Parameters for $\bar{\iota} = .1$ and $M^* = 2$

Constraints			
$\bar{\iota}_{external}$	.1	.1	.1
K_β	.5	.5	.5
B_{zo} (tesla)	10	8	4.3
$\mathcal{F}$	.1	.06	.04
$\mathcal{Q}$ (MN/m)	2	4	8
$P_{th}^{primary}$ (MW)	3000	3000	3000
N , M^*	5 , 2.5	5 , 2.5	5 , 2.5
Parameters			
margin of ignition	2.82	4.35	7.25
wall loading (MW/m^2)	2.51	3.45	3.52
t (meters)	.120	.268	.566
a_{plasma} (meters)	1.08	1.21	1.98
r_{coil} (meters)	1.94	2.14	3.06
R_o (meters)	28.04	18.20	10.92
I_{helix} (MA)	1.17	1.77	3.24
$\langle j \rangle_{helix}$ (A/cm^2)	1139	699	425
$h + 2\,t_p$ (meters)	.26	.40	.98

Table 4.4D — Optimal Reactor Parameters for $\bar{\iota} = .1$ and $M^* = 2.5$

Constraints				
$\bar{\iota}_{external}$	.1	.1	.1	.1
K_β	.5	.5	.5	.5
B_{zo} (tesla)	10	8.2	5.1	2.8
$\mathcal{F}$	.1	.1	.06	.03
$\mathcal{Q}$ (MN/m)	2	4	8	16
$P_{th}^{primary}$ (MW)	4000	3000	3000	3000
N , M^*	6 , 3	6 , 3	6 , 3	6 , 3
Parameters				
margin of ignition	2.94	3.81	6.28	10.17
wall loading (MW/m^2)	2.29	3.00	3.48	3.49
t (meters)	.106	.168	.388	1.58
a_{plasma} (meters)	1.23	1.22	1.73	2.79
r_{coil} (meters)	2.08	2.10	2.72	4.38
R_o (meters)	35.85	20.76	12.61	7.78
I_{helix} (MA)	1.16	1.68	2.88	6.64
$\langle j \rangle_{helix}$ (A/cm^2)	1199	1077	619	218
$h + 2\,t_p$ (meters)	.26	.39	.87	3.65

Table 4.4E — Optimal Reactor Parameters for $\bar{\iota} = .1$ and $M^* = 3$

Constraints				
$\bar{\iota}_{external}$	.1	.1	.1	.1
K_β	.5	.5	.5	.5
B_{zo} (tesla)	10	10	7	3
$\mathcal{F}$	.1	.1	.06	.04
$\mathcal{Q}$ (MN/m)	2	4	8	16
$P_{th}^{primary}$ (MW)	5000	3000	3000	3000
N , M^*	7 , 3.5	7 , 3.5	7 , 3.5	7 , 3.5
Parameters				
margin of ignition	2.98	3.11	4.92	9.69
wall loading (MW/m^2)	2.08	2.84	3.52	3.52
t (meters)	.097	.189	.433	1.17
a_{plasma} (meters)	1.37	1.05	1.34	2.64
r_{coil} (meters)	2.22	1.95	2.36	4.02
R_o (meters)	44.26	25.42	16.09	8.17
I_{helix} (MA)	1.16	1.55	2.51	6.17
$\langle j \rangle_{helix}$ (A/cm^2)	1223	956	558	298
$h + 2\,t_p$ (meters)	.27	.38	.76	3.44

Table 4.4F — Optimal Reactor Parameters for $\bar{\iota} = .1$ and $M^* = 3.5$

Constraints				
$\bar{\iota}_{external}$	.1	.1	.1	.1
K_β	.5	.5	.5	.5
B_{zo} (tesla)	10	10	8	4
$\mathcal{F}$	.1	.1	.085	.044
$\mathcal{Q}$ (MN/m)	2	4	8	16
$P_{th}^{primary}$ (MW)	5000	4000	3000	3000
N , M^*	8 , 4	8 , 4	8 , 4	8 , 4
Parameters				
margin of ignition	2.61	3.44	4.40	7.63
wall loading (MW/m^2)	1.77	2.79	3.50	3.48
t (meters)	.103	.160	.315	1.05
a_{plasma} (meters)	1.42	1.18	1.21	2.10
r_{coil} (meters)	2.27	2.06	2.16	3.43
R_o (meters)	50.55	30.70	18.00	10.38
I_{helix} (MA)	1.13	1.54	2.31	5.02
$\langle j \rangle_{helix}$ (A/cm^2)	1094	1058	768	317
$h + 2\,t_p$ (meters)	.27	.39	.70	2.65

Table 4.4G — Optimal Reactor Parameters for $\bar{\iota} = .1$ and $M^* = 4$

Constraints				
$\bar{\iota}_{external}$	.1	.1	.1	.1
K_β	.5	.5	.5	.5
B_{zo} (tesla)	10	10	8	5
$\mathcal{F}$	.1	.1	.1	.05
$\mathcal{Q}$ (MN/m)	2	4	8	16
$P_{th}^{primary}$ (MW)	5000	4000	3000	3000
N , M^*	9 , 4.5	9 , 4.5	9 , 4.5	9 , 4.5
Parameters				
margin of ignition	2.32	3.06	4.01	6.37
wall loading (MW/m^2)	1.52	2.41	3.12	3.48
t (meters)	.109	.170	.279	.934
a_{plasma} (meters)	1.46	1.22	1.23	1.76
r_{coil} (meters)	2.32	2.10	2.17	3.03
R_o (meters)	56.88	34.48	19.74	12.42
I_{helix} (MA)	1.11	1.51	2.25	4.33
$\langle j \rangle_{helix}$ (A/cm^2)	991	960	844	349
$h + 2\,t_p$ (meters)	.28	.39	.70	2.21

Table 4.4H — Optimal Reactor Parameters for $\bar{\iota} = .1$ and $M^* = 4.5$

Constraints				
$\bar{\iota}_{external}$	.1	.1	.1	.1
K_β	.5	.5	.5	.5
B_{zo} (tesla)	10	10	10	6
$\mathcal{F}$	.1	.1	.1	.058
$\mathcal{Q}$ (MN/m)	2	4	8	16
$P_{th}^{primary}$ (MW)	5000	4000	3000	3000
N , M^*	10 , 5	10 , 5	10 , 5	10 , 5
Parameters				
margin of ignition	2.09	2.76	3.34	5.53
wall loading (MW/m^2)	1.33	2.11	3.10	3.50
t (meters)	.116	.179	.308	.819
a_{plasma} (meters)	1.50	1.25	1.03	1.52
r_{coil} (meters)	2.36	2.14	2.00	2.73
R_o (meters)	63.22	38.28	23.68	14.32
I_{helix} (MA)	1.09	1.48	2.07	3.87
$\langle j \rangle_{helix}$ (A/cm^2)	907	880	766	393
$h + 2\,t_p$ (meters)	.28	.40	.65	1.92

Table 4.4I — Optimal Reactor Parameters for $\bar{\iota} = .1$ and $M^* = 5$

Constraints				
$\bar{\iota}_{external}$	.1	.1	.1	.1
K_β	.5	.5	.5	.5
B_{zo} (tesla)	10	10	10	7
$\mathcal{F}$	.1	.1	.1	.067
$\mathcal{Q}$ (MN/m)	2	4	8	16
$P_{th}^{primary}$ (MW)	5000	5000	3000	3000
N , M^*	11 , 5.5	11 , 5.5	11 , 5.5	11 , 5.5
Parameters				
margin of ignition	1.90	2.97	3.04	4.89
wall loading (MW/m^2)	1.18	2.08	2.76	3.49
t (meters)	.122	.158	.324	.727
a_{plasma} (meters)	1.54	1.37	1.06	1.34
r_{coil} (meters)	2.40	2.25	2.02	2.51
R_o (meters)	69.60	44.36	26.03	16.20
I_{helix} (MA)	1.07	1.49	2.04	3.53
$\langle j \rangle_{helix}$ (A/cm^2)	837	948	707	440
$h + 2\,t_p$ (meters)	.28	.41	.66	1.73

Table 4.4J — Optimal Reactor Parameters for $\bar{\iota} = .1$ and $M^* = 5.5$

Constraints				
$\bar{\iota}_{external}$	.1	.1	.1	.1
K_β	.5	.5	.5	.5
B_{zo} (tesla)	10	10	10	8
$\mathcal{F}$	.1	.1	.1	.078
$\mathcal{Q}$ (MN/m)	2	4	8	16
$P_{th}^{primary}$ (MW)	5000	5000	4000	3000
N , M^*	12 , 6	12 , 6	12 , 6	12 , 6
Parameters				
margin of ignition	1.74	2.73	3.57	4.39
wall loading (MW/m^2)	1.06	1.88	2.92	3.50
t (meters)	.127	.165	.264	.641
a_{plasma} (meters)	1.57	1.40	1.17	1.21
r_{coil} (meters)	2.44	2.29	2.11	2.33
R_o (meters)	76.00	48.40	29.58	18.01
I_{helix} (MA)	1.06	1.47	2.04	3.26
$\langle j \rangle_{helix}$ (A/cm^2)	777	881	831	498
$h + 2\,t_p$ (meters)	.28	.41	.67	1.58

Table 4.4K — Optimal Reactor Parameters for $\bar{\iota} = .1$ and $M^* = 6$

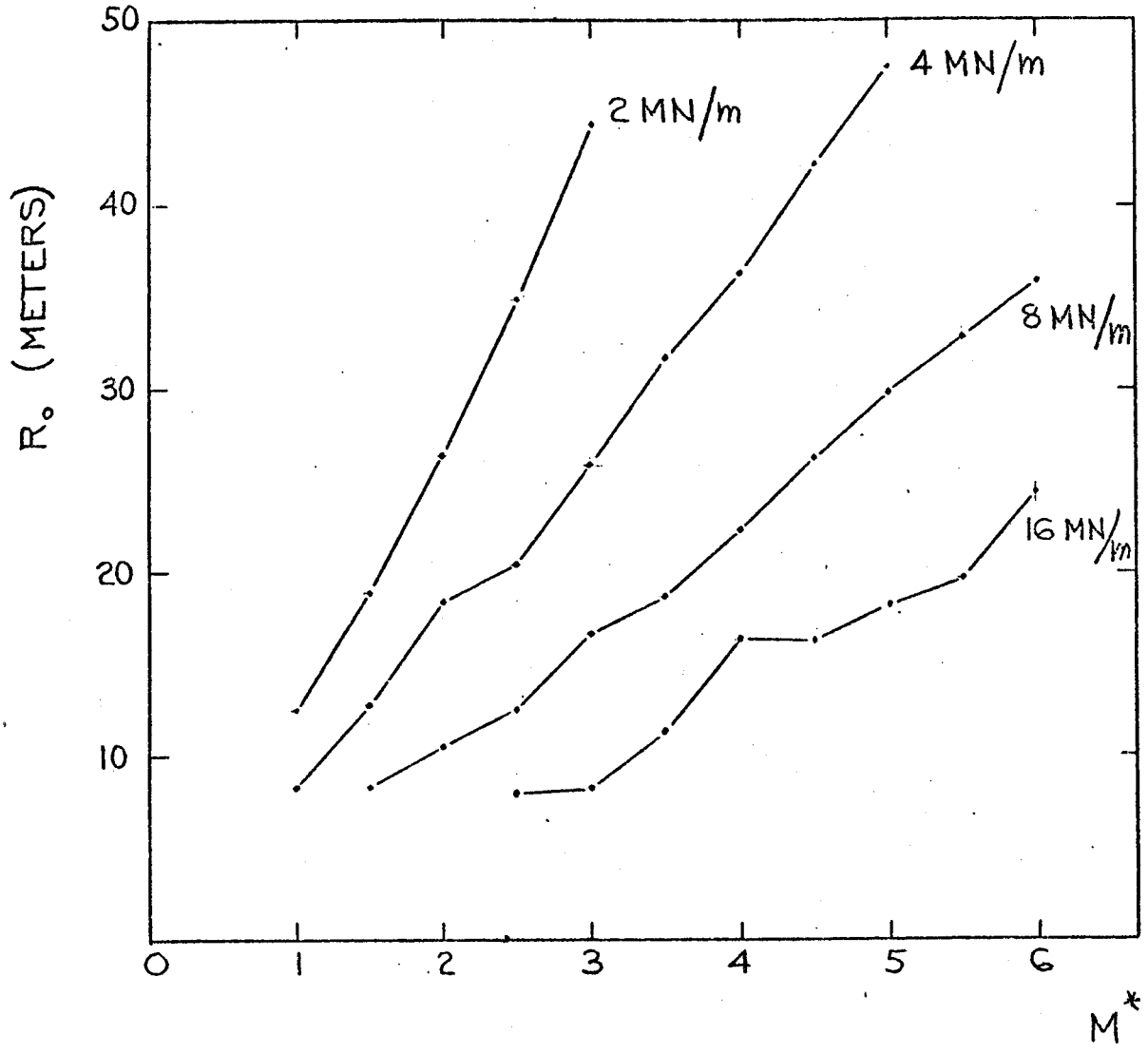

FIGURE 4.2

OPTIMIZED REACTOR RADIUS VERSUS $\langle$FORCE/LENGTH$\rangle$ AND M^* FOR $\bar{\iota} = .15$

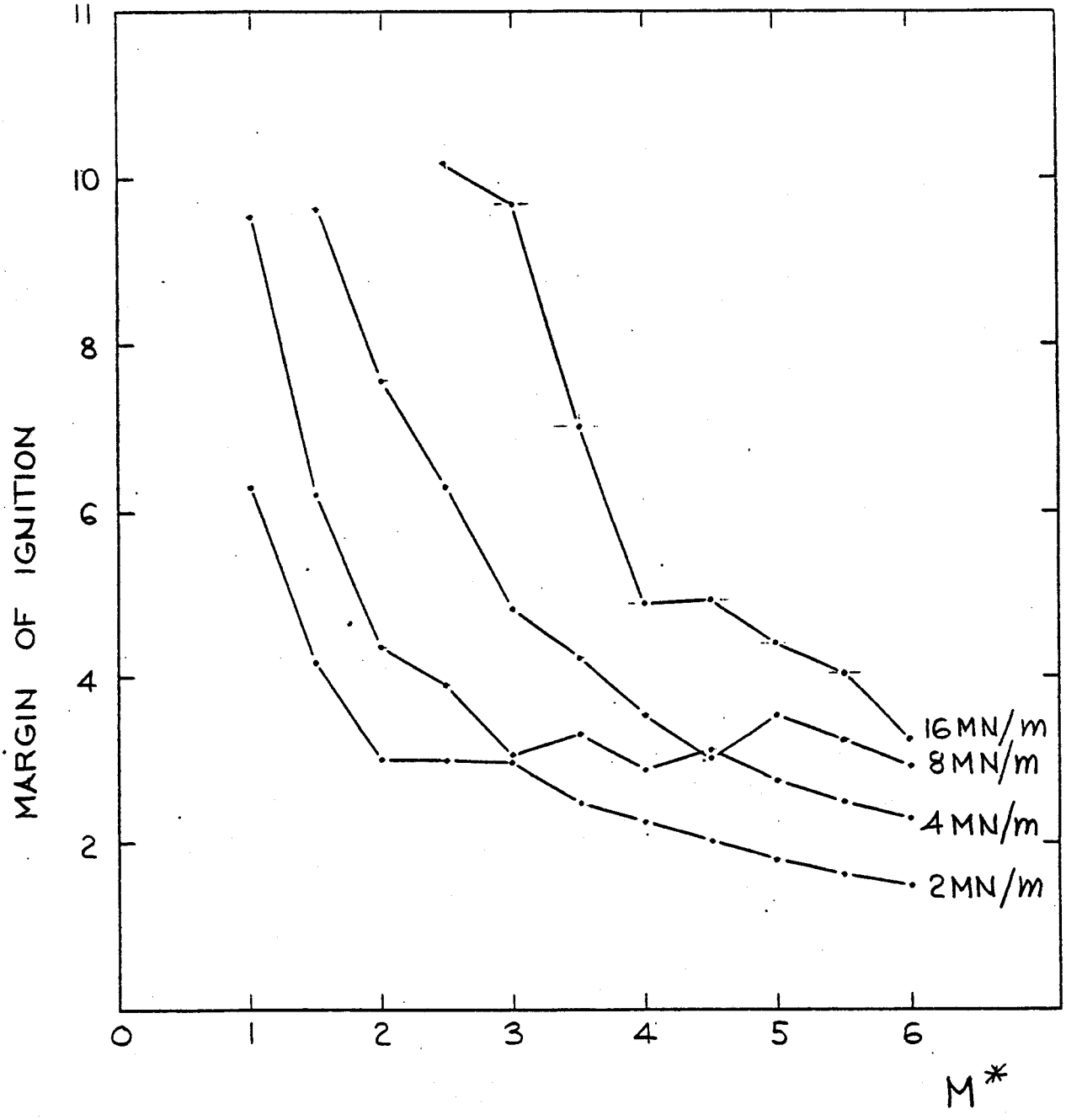

FIGURE 4.3

OPTIMIZED MARGIN OF IGNITION VERSUS $\langle$FORCE/LENGTH$\rangle$ AND M^* FOR $\bar{\tau}$=.15

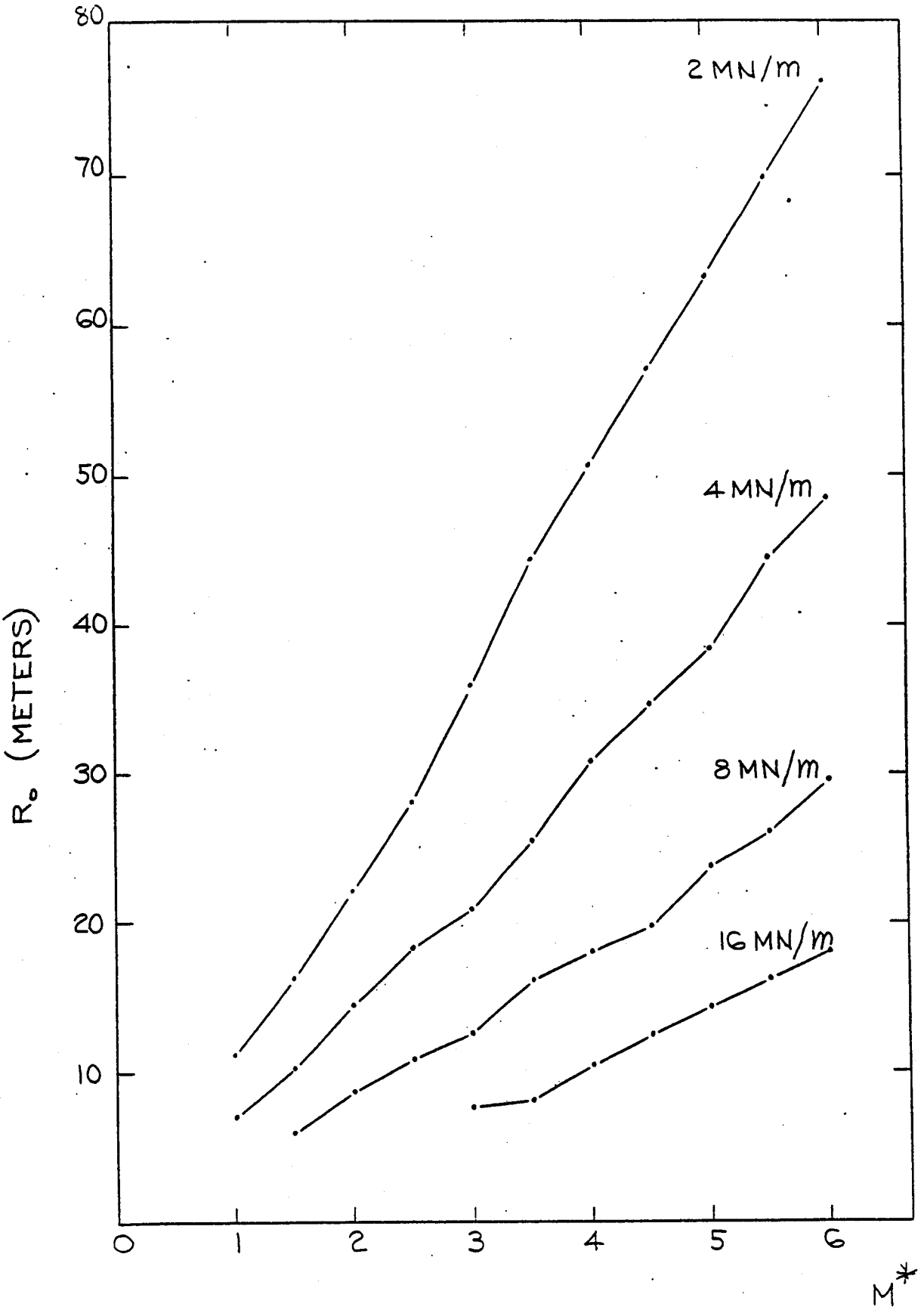

FIGURE 4.4

OPTIMIZED REACTOR RADIUS VERSUS FORCE LENGTH AND M^* FOR $\bar{\iota} = .1$

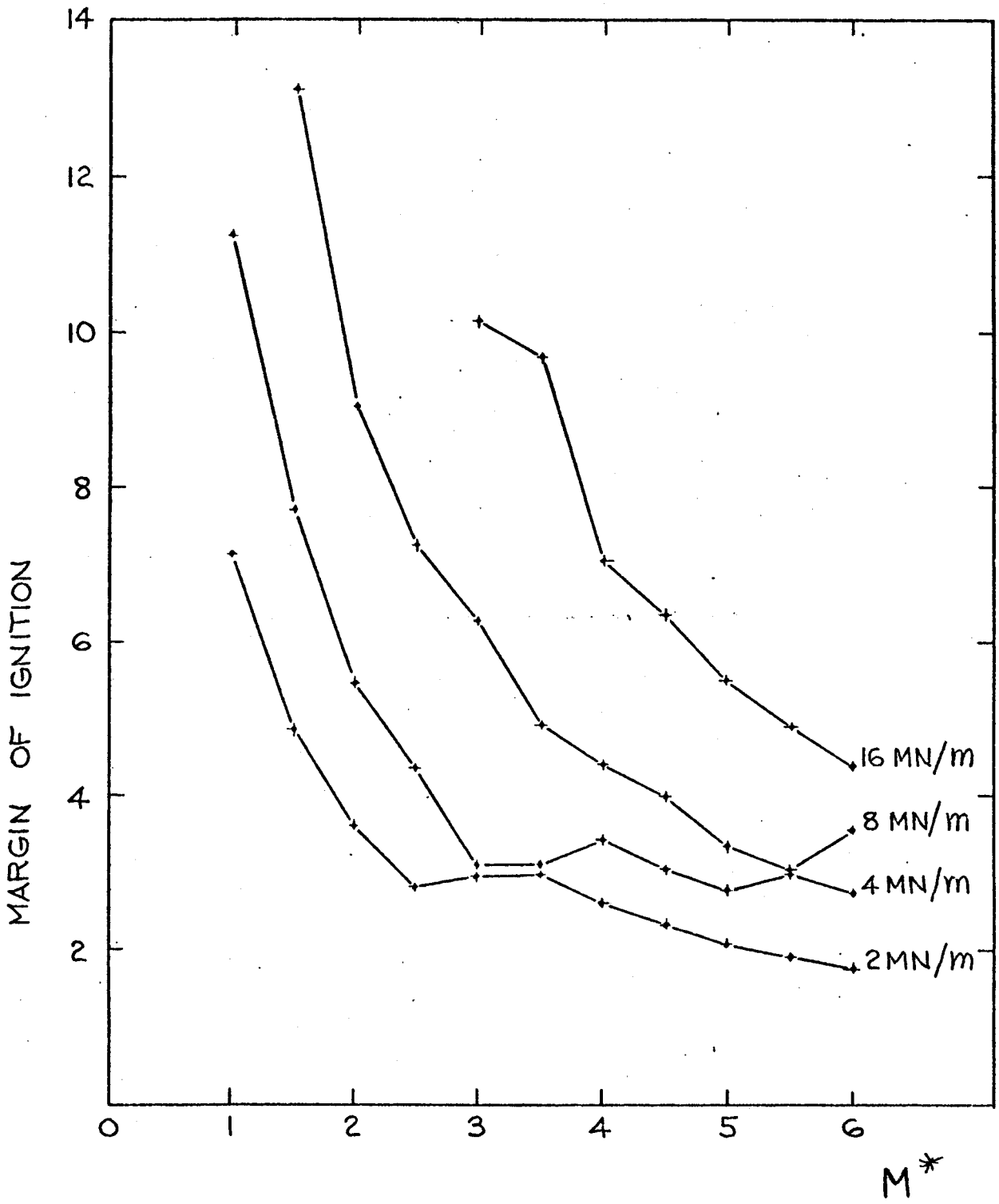

FIGURE 4.5

OPTIMIZED MARGIN OF IGNITION VERSUS $\langle$FORCE/LENGTH$\rangle$ AND M^* FOR $\bar{\upsilon}=.1$

From the previous tables, it can be seen that the option space for an attractive tokamak-stellarator reactor is constrained by the scaling laws described in Chapter III. From Table 4.1, we see the general result that the optimum choices for N and K_β are $N = \ell M^*$, $K_\beta = .5$. Under these constraints, the need to keep the ⟨force/meter⟩ on the helical coils $\leq$ 10 MN/m results in a rather large major radius for the base design (14.31 m), in order to keep the angle between the helical coils and the toroidal field small. Since the tokamak-stellarator reactor is still bound by the $1/A$ scaling in β_t (A = plasma aspect ratio = R_o/a_p), very high toroidal fields ($B_{zo} \simeq$ 10 tesla) are needed to raise the wall loading to an economically attractive value ($\geq$ 2 MW/m^2) if more conservative values of $\mathcal{Q}$ and M^* are needed.

It is instructive to review the characteristics of a conventional tokamak and see the changes effected by the tokamak–stellarator configuration. From the point of modifying a tokamak to prevent disruptions, the "cure" of external helical windings has detrimental side effects. If conversative limits for M^*, $\mathcal{Q}$, $\bar{\iota}$, and K_β are used, the tokamak–stellarator reactor would have:

1) wall loading = 1.31 MW/m^2,

2) P_{th} = 5000 MW, and

3) R_o = 48.19 m,

where the following reactor constraints are assumed:

1) $K_\beta = .3$,

2) B_{zo} = 9 tesla,

3) ⟨force/meter⟩ on the helical coils = 8 MN/m,

4) ohmic power loss in helical coils = 500 $MW_{electric}$.

5) external transform = .15

6) $M^* = 5.5$

This incompatibility of helical coils with TF coils for reactor regimes is evidenced by Japanese designs for a heliotron reactor[2], where even the use of small toroidal field trim coils was ruled out due to assembly and support problems. From the point of view of modifying a reactor of the stellarator-torsatron family, it is difficult to see the overriding advantage in adding a plasma current and making the machine non steady state and susceptible to tokamak β_t and current filamentation limits. There thus appears to be only a small overlap between the physical, engineering, and economic constraints on the tokamak-stellarator reactor, provided modest improvements in the M^* and $\bar{\iota}^{external}$ requirements are possible.

4.4 Analysis of a Resistive Tokamak–Stellarator

We will now show that a tokamak–stellarator with resistive toroidal field coils internal to the helical coils does not appear to be an attractive reactor. In this concept, resistive toroidal field coils are used to reduce the shielding requirements, and the helical coils are placed external to the toroidal field coils in order to eliminate the large forces between the toroidal field and the helical currents. In general, a resistive tokamak has two operating regimes, a high field, small major radius regime, and a low field, large major radius regime. Since the external transform from the helical coils scales as $(R_o/B_{zo})^2$, the helical coils are well suited to the low field, large R_o regime, and are completely incompatible with the high field, small R_o regime. Unfortunately, the low field, large R_o resistive

tokamak is not a particularly attractive concept to begin with, and the extra constraints imposed by the helical coils make the system even less attractive. The ratio of electrical power dissipated by resistive toroidal field coils divided by the primary thermal fusion power ($\mathcal{F}_t$) may be expressed as:

$$\mathcal{F}_t = \frac{{B_{zo}}^2 r_{TF}}{37.9\, t_{TF}\ (\text{margin of ignition})}$$

where

r_{TF} = minor radius of toroidal field coil, and

t_{TF} = radial thickness of toroidal field coil.

In optimizing the design of a low field, large R_o resistive tokamak, one has the goal of minimizing P_{th}, $\mathcal{F}_t$, and R_o simultaneously. At constant $\mathcal{F}$, the need for low M^* is no longer critical, since the extra helical current requirements at high M^* result in thicker helical coils, but not in an increase in the structural support for the helical coil – toroidal field coil interaction.

Three cases of a resistive tokamak–stellarator reactor are shown in Table 4.5 . $B_{zo} \simeq 3$ tesla appears to be the optimal toroidal field on axis; lower B_{zo} results in lower wall loadings and unacceptably large plasma radii, while higher B_{zo} results in too high a value for $\mathcal{F}_t$. It also appears that $\mathcal{F}_{helix} \simeq .07$ and $P_{th} \simeq 4000$ MW optimizes the trade-offs between wall loading, ohmic dissipation, and margin of ignition. The reactor should operate at as high a K_β as possible, and for Table 4.5, K_β is optimistically assumed to be .4 . The distance between the helical coil and the plasma edge should be as small as possible, and for this analysis this distance was set at 1.5 meters (.75 meters

for the void and blanket, and .75 meters for the radial thickness of the toroidal field coils). Table 4.5 shows that a somewhat attractive reactor only exists for very low helical coil aspect ratios. There is little experimental evidence for the performance of helical coils with $R_o/r_{helix} \leq 3$, and there is strong theoretical and computational evidence[3] that such systems might suffer from enhanced heat transport and trapped-particle instabilities. It thus appears unlikely that the resistive tokamak–stellarator reactor will be an attractive concept.

R_o/r_{helix}	2	3	4
K_β	.4	.4	.4
P_{th}	4,000 MW	4,000 MW	4,000 MW
$\mathcal{F}_{helix}$	.07	.07	.07
$\mathcal{F}_t$	.142	.249	.373
R_o	10.51 m	16.86 m	23.61 m
r_{helix}	5.25 m	5.58 m	5.87 m
a_p	3.38 m	3.80 m	4.14 m
wall loading	2.85 MW/m^2	1.58 MW/m^2	1.04 MW/m^2
B_{zo}	3 tesla	3 tesla	3 tesla
margin of ignition	10.04	6.26	4.47

Table 4.5 — A Resistive Tokamak–Stellarator Reactor

4.5 STARFIRE with Helical Coils

It is instructive to compare the scaling relationships developed in Chapter III with a representative tokamak design. For STARFIRE, with $K_\beta = .19$, $R_o = 7$ m, and $P_{th} = 4000$ MW, a set of helical coils could be placed at a minor radius of 3.5 meters. For an external transform of .15, the following helical currents would be required:

M^*	5	2
I_h	13.33 MA	7.86 MA
$\mathfrak{Q}$	71 MN/m	30 MN/m
$h + 2t_p$	15.77 m	3.86 m
$\mathcal{F}$	.152	.053

Table 4.6 — STARFIRE with Helical Coils

In Table 4.6, it is optimistically assumed that 1 radial meter of space is available for the helical conductors. This still results in an ohmic power dissipation of 609 MW for the $M^* = 5$ case, and 212 MW for the $M^* = 2$ case. As will be shown in Chapter V, the values of $\mathfrak{Q}$ result in impossibly thick support structures, even for the $M^* = 2$ case.

References

1) STARFIRE, A Commercial Tokamak Fusion Power Plant Study, Argonne National Laboratory ANL/FPP–80–1, Volumes 1 and 2, September 1980, Argonne, Illinois

2) A. Iiyoshi and K. Uo Proceedings of the Fifth International Conference on Plasma Physics and Controlled Nuclear Fusion Research; Tokyo, 3, p. 619, 11–15 November 1974, International Atomic Energy Agency, Vienna, Austria

3) R. E. Potok, et. al. M.I.T. Plasma Fusion Center Report PFC/RR–80–15, 1981.

Chapter V – Support Structure for the Helical Coils

In this chapter we will show that the bending stress provides the dominant constraint on the helical coil support structure design, and give representative structural dimensions needed to support the bending moments of the base design. An alternative support configuration, one more compatible with modularization, is presented in Chapter VII.

5.1 Analysis of Bending Moments and Stresses on Helical Coils

The bending moment m of an $\ell = 2$ stellarator configuration on a circular hoop (with F being a unit force proportional to the helical current) can be expressed by the following equation (see also Figure 5.1):

$$m(\theta) = .5Fr_s(\sin(\theta) - \cos(\theta))$$

$$m^{max} = .5Fr_s$$

In constrast, the peak bending moment of a torsatron coil design producing the same external transform is $2Fr_s/\pi$, a 28% increase over the stellarator design. The structure supporting these bending moments can be represented by a series of I-beam rings mounted poloidally around the coils. This support structure is illustrated in Figures 5.2 and 5.3 , where the top and side views of a representative $M^* = 2$ reactor are shown. The girders have a plate thickness t_p and a web height h. Each girder has a toroidal width b, with the support system completely enclosing the blanket region

FORCES ON RING SUPPORT
OF AN $\ell = 2$
STELLARATOR CONFIGURATION
BENDING MOMENT $(0^\circ) = .5 F r_s$

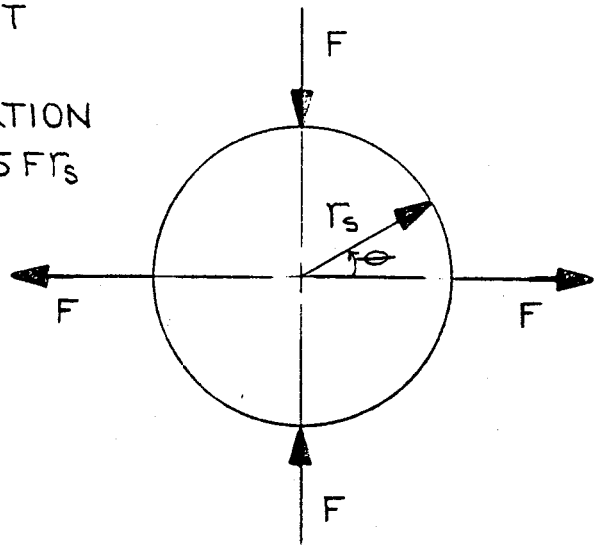

FORCES ON RING SUPPORT
OF AN EQUIVALENT $\ell = 2$
TORSATRON CONFIGURATION
BENDING MOMENT $(0^\circ) = {}^2/_{\pi} F r_s$

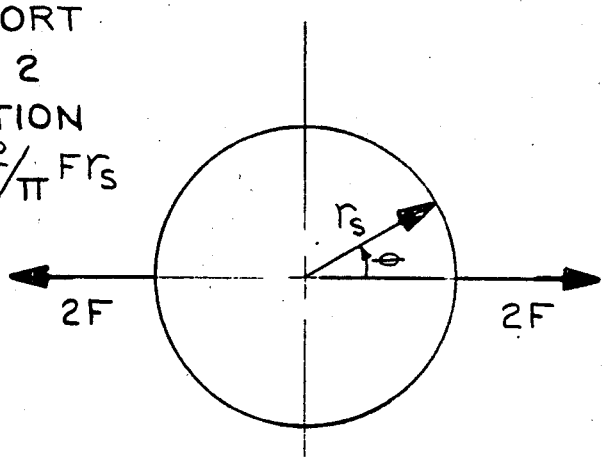

FIGURE 5.1

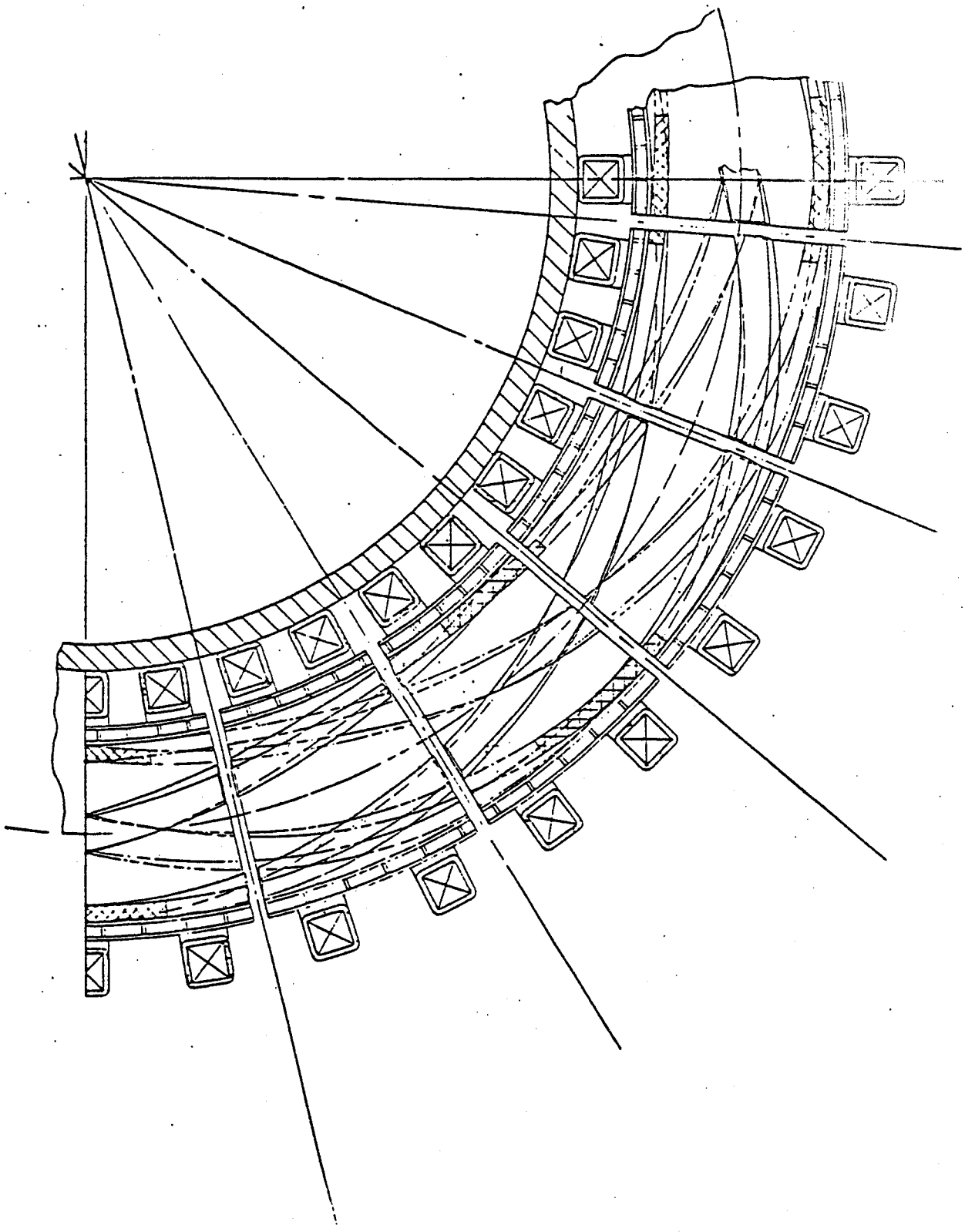

FIGURE 5.2
TOP VIEW OF AN $M^* = 2$ TOKAMAK-STELLARATOR REACTOR

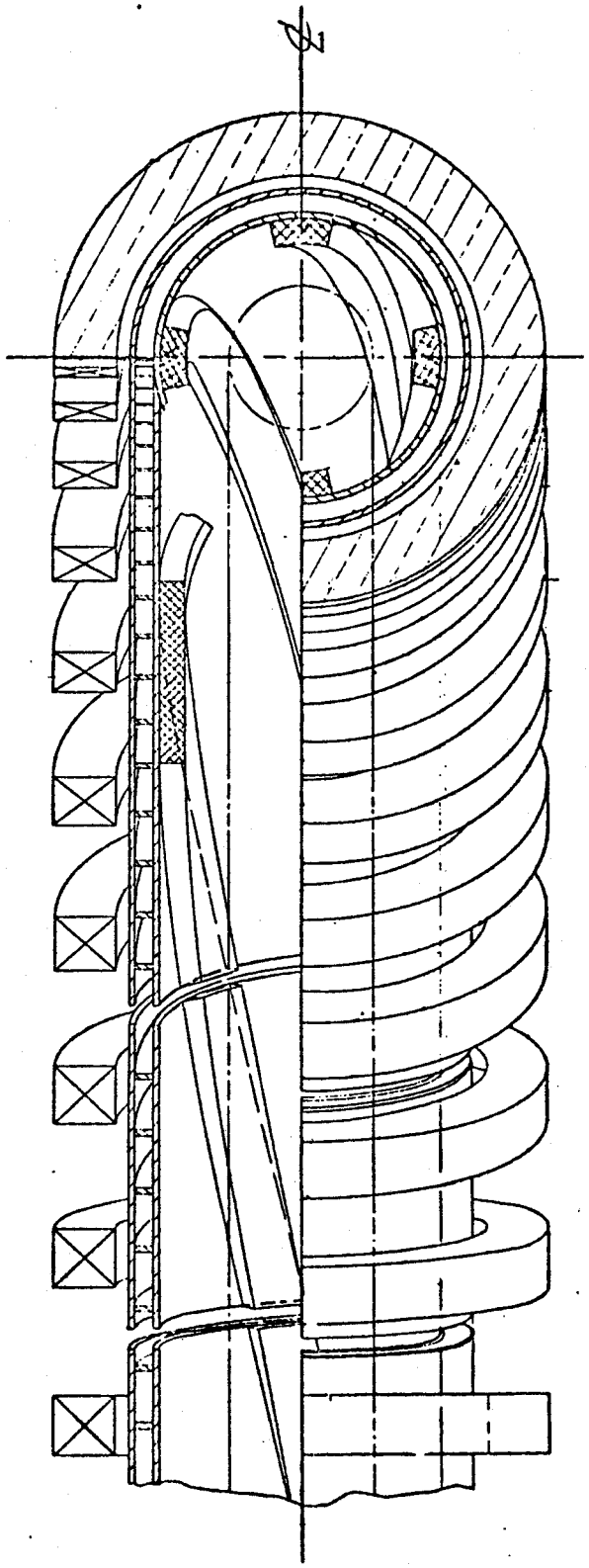

FIGURE 5.3
SIDE VIEW OF AN $M^* = 2$ TOKAMAK-STELLARATOR REACTOR

both toroidally and poloidally. Access requirements are optimistically assumed to be a negligible influence on this representative support design.

Define $\mathfrak{Q} =$ the ⟨force/meter⟩ on each helical coil. The average force per *toroidal* meter ($\mathfrak{Q}^*$) can be expressed as:

$$\mathfrak{Q}^* = \mathfrak{Q}\sqrt{1+\left(\frac{N}{\ell}\frac{r_{\text{coil}}}{R_o}\right)^2}$$

The axial stress σ_{ax} on the hoop of I-beams is:

$$\sigma_{ax} = \frac{F/2}{\text{area}} = \frac{\mathfrak{Q}^* b/2}{(2b+h)t_p}$$

while the bending stress σ_b is:

$$\sigma_b = \frac{\mathfrak{Q}^* b(r_s + h/2)/2}{bt_p(h+t_p/2) + \frac{1}{6}t_p h^2}$$

where

$r_s =$ minor radius of inner structural support of helical coil $= r_{\text{coil}} + t_{\text{coil}}/2 + t_p$

In the limit of $r_s \gg h$,

$$\sigma_b = \frac{2r_s}{h}\sigma_{ax}$$

so, for parameters of reactor interest, it is the bending stress, and not the axial stress, that is the dominant constraint.

If the pitch length of the coils were much less than the radius of the support structure, the bending stresses would be substantially reduced, due to the cancellation of radial forces between adjacent helical coils. The parameter of interest is:

$$\frac{2\pi R_o}{N(r_s + h/2)} \ll 1$$

Unfortunately, for parameters of reactor interest, this parameter is greater than one, and the amount of cancellation is minimal. For the base design, this parameter equals 3.52 .

5.2 Analysis of a Representative Helical Coil Support Structure

Since the representative support structure is not cryogenically cooled, (due to difficulties in thermally isolating the support structure from the fusion and ohmic power sources), the maximum allowable stress is set at 200 MPa (= 29,000 psi). A practical value for the toroidal spacing for the radial ribs of the support structure is 1 meter (i.e. $b = 1$ meter), and a practical upper limit on the thickness of the 316-stainless steel plates of the I-beams would be 10 cm ($t_p = .1$ m) . With these values, the expression for h becomes:

$$40\,h^2 + (240 - 3\mathcal{Q}^*)\,h + (12 - 6\mathcal{Q}^* r_s) = 0$$

$$h = \frac{(3\mathcal{Q}^* - 240) + \sqrt{(3\mathcal{Q}^* - 240)^2 + 160(6\mathcal{Q}^* r_s - 12)}}{80}$$

For these equations, h and r_s are in meters, and $\mathcal{Q}^*$ is in MN/meter. A plot of h versus $\mathcal{Q}^*$ and r_s is presented in Figure 5.4 . In the base design, $\mathcal{Q} = 10$ MN/m, $\mathcal{Q}^* = 12.2$ MN/m, and $r_s = 2.78$ m. Substituting, we obtain:

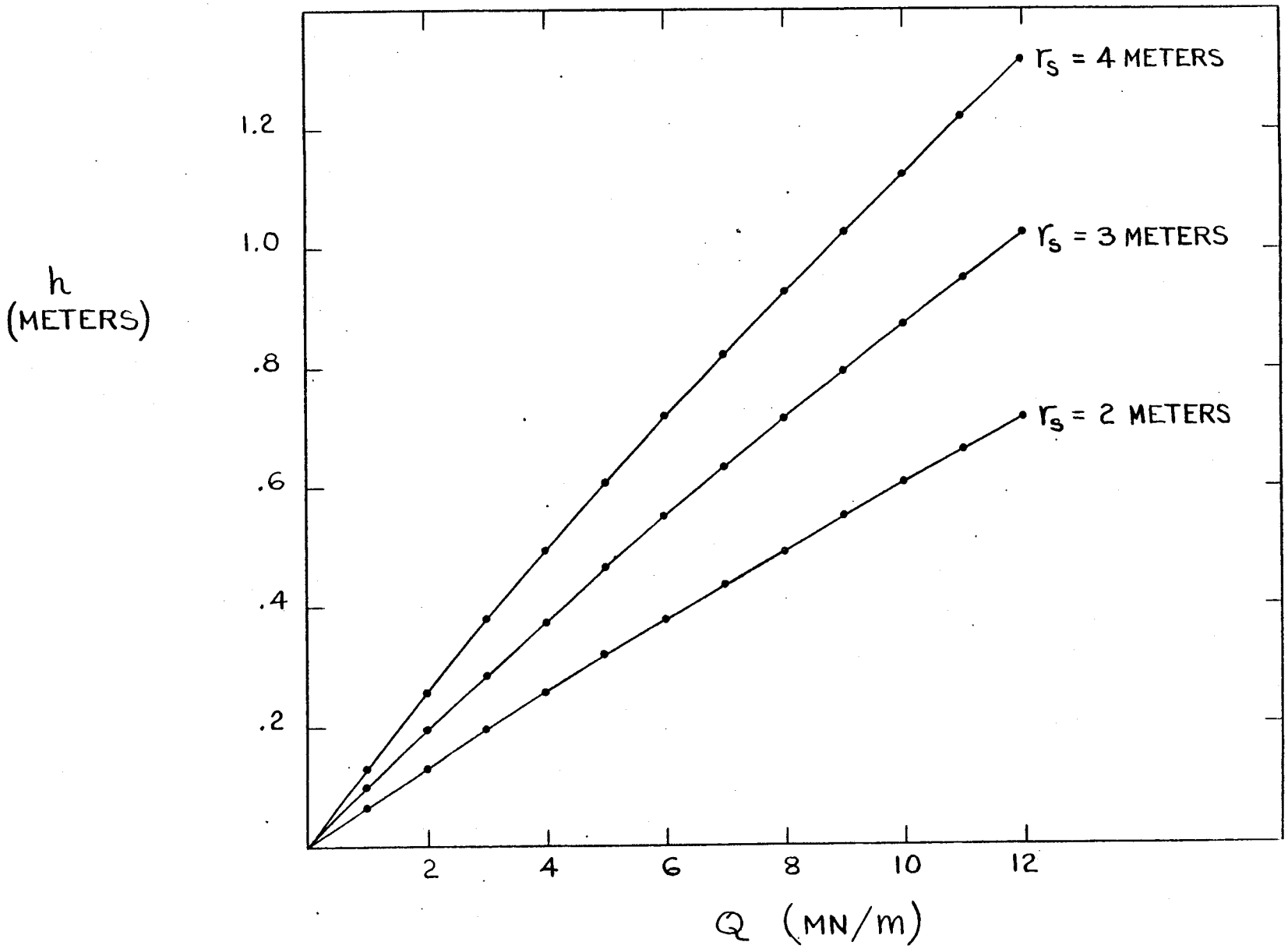

FIGURE 5.4 — h VERSUS Q AND r_s

$h =$ web height $= .82$ m

We see now that even the optimistic base design requires a large supporting structure internal to the TF coils. Furthermore, we have been considering only the average force between the helical coils and toroidal field, and have optimistically assumed the access requirements will impose a negligible influence on the bending stresses. In addition, the helical coils will interact with each other, with the vertical field and ohmic field coils, and with the plasma current. These interactions will add approximately 10% onto the maximum force resulting from the toroidal field.

We thus see that the detailed design of the helical coil support structure of the base design, while possible, might pose some formidable problems. In addition to the access needed during reactor operation for heat removal, neutral beam or RF injection ducts, divertor channels, etc., the helical coil support system must be compatible with the procedures for assembly and maintenance. There must be sufficient space to bolt together the helical coil current elements and vacuum-seal the plasma chamber with the support structure and TF coils already in place.

Increased access can be obtained by decreasing $\langle \mathfrak{Q} \rangle$ and keeping a favorably high wall loading by increasing P_{th}, but a relatively small decrease in bending moment results in a large increase in P_{th} and R_o. For example, keeping $K_\beta = .5$, $\bar{\iota} = .15$, $B_{zo} = 8$ tesla, $\mathcal{T} = .05$, and the wall loading $=$ 3.47 MW/m, we can see from Table 5.1 that decreasing the radial thickness of the support structure by 29% (from 42 cm to 30 cm) increases P_{th} by 217% and R_o by 100%. Given these scaling relationships, it can be seen that a tokamak-stellarator reactor needs a minimum of $\mathfrak{Q} \simeq 4$ MN/m to be of modest size at $M^* = 2$ (see Table 5.1). If an $M^* = 5$ limit is assumed, then $\mathfrak{Q} \geq 20$ MN/m

would be necessary (see Table 5.2).

It will be difficult to connect the cables, the associated cooling supplies, and the attachments to the helical coil support structure. The connection problems could be eased by placing the support structure internal to the helical coils, but this would result in a sharp drop in the wall loading and a large increase in the major radius R_o. These changes are summarized in Table 5.3, where a comparison is made of the base design with the helical coils internal and external to their support structure. For the same illustrative design constraints on $\bar{\iota}$, K_β. B_{zo}, $\mathcal{F}$, $\mathcal{Q}$, P_{th}, and M^*, it can be seen that placing the helical coils external to their support structure decreases the wall loading by 71%, and increases the major radius R_o by 171%. This unfavorable scaling would be even more pronounced if higher values of $\mathcal{Q}$ were used.

$\mathcal{Q}$	$h + 2t_p$	r_{coil}	R_o	P_{th}
2 MN/m	.30 m	2.78 m	36.18 m	9500 MW
3 MN/m	.35 m	2.35 m	22.75 m	4400 MW
4 MN/m	.42 m	2.23 m	18.13 m	3000 MW
6 MN/m	.58 m	2.23 m	14.76 m	2150 MW
8 MN/m	.79 m	2.34 m	13.64 m	1860 MW
12 MN/m	1.28 m	2.62 m	13.05 m	1740 MW
16 MN/m	1.87 m	2.91 m	13.19 m	1770 MW

Table 5.1 — Scaling of Reactor Parameters versus $\mathcal{Q}$ — $M^* = 2$

$\mathcal{Q}$	$h + 2t_p$	r_{coil}	R_o	P_{th}
8 MN/m	.84 m	2.97 m	38.49 m	10500 MW
12 MN/m	1.21 m	2.72 m	26.92 m	5800 MW
16 MN/m	1.69 m	2.75 m	23.35 m	4600 MW
24 MN/m	2.88 m	3.03 m	21.40 m	3960 MW
32 MN/m	4.25 m	3.37 m	21.31 m	3930 MW
48 MN/m	7.29 m	4.07 m	22.50 m	4280 MW

Table 5.2 — Scaling of Reactor Parameters versus $\mathcal{Q}$ — $M^* = 5$

Constraints		
$\iota_{external}$	.1	.1
K_β	.5	.5
B_{zo} (tesla)	6	6
$\mathcal{F}$	.08	.08
$\langle \mathcal{Q} \rangle$ (MN/m)	10	10
$P_{th}^{primary}$ (MW)	3000	3000
N , M^*	8 , 4	8 , 4
helical coil support system	external	internal
Parameters		
margin of ignition	5.53	2.04
wall loading (MW/m^2)	3.50	1.01
t (meters)	.367	.903
a_{plasma} (meters)	1.52	1.95
r_{coil} (meters)	2.50	4.71
R_o (meters)	14.31	38.72
I_{helix} (MA)	2.91	3.81
$\langle j \rangle_{helix}$ (A/cm^2)	721	204
$h + 2t_p$ (meters)	1.02	1.51

Table 5.3 — Comparison of Internal and External Helical Support Structure

Chapter VI – Analysis of Numerical and Experimental Data

6.1 Field Line Tracing

A key question of the tokamak-stellarator concept is whether one can combine the external helical transform and the internal plasma transform and still maintain good flux surfaces. In order to answer this question, a number of field line traces were done in which several different helical winding geometries were tested, with either a PEST[1] equilibrium or analytic background tokamak field. The primary drawback of such a procedure is that it does not reflect the change in the plasma current equilibrium profile caused by the helical windings, yet it is the best available procedure given the lack of a general 3-D equilibrium code. The change in the rotational transform of a surface was computed by integrating along the perturbed path (i.e. integrating along a field line produced by both plasma current and stellarator coils) the transform due to the composite fields and the transform due to the tokamak fields alone.

$$\langle q \rangle = \frac{\int_{surface} \frac{rB_{zo}}{RB_p} d\ell}{\int_{surface} d\ell}$$

$$\iota^{\text{added}} = \frac{1}{\langle q \rangle^{\text{perturbed}}} - \frac{1}{\langle q \rangle^{\text{unperturbed}}}$$

It was found that $\iota^{\text{added}} = \iota^{\text{external}} \pm 20\%$ for $R_o/r_{\text{coil}} \geq 4$, $\iota^{\text{external}}/\iota^{\text{plasma}} \leq .2$, and $r/r_{\text{separatrix}} \leq .5$, so for this regime it is valid to assume one can add together the plasma and helical windings transforms. For low N (1 to 3), it was found that the separatrix radius would rapidly decrease as the external transform was increasesd from 0 to .15. It is thus useful to find the maximum transform that can be imposed at a given plasma radius a_p, without creating magnetic islands and ergodic field lines within a_p.

Table 6.1 shows the maximum external transform that can be imposed for $r_{\text{coil}} = 2.5$ m, $\langle a_p \rangle = 1$ m, and $R_o = 11.5$ m (toroidal effects, however, are not important and these results were found to be fairly independent of aspect ratio). An $\ell = 2$ constant pitch stellarator winding was used for the helical coils.

q at a_p	$N = 1$	$N = 2$	$N = 3$	$N = 4$
2	$\leq .0001$	.052	.16	.266
3	$\leq .0001$	.103	.20	$> .3$
4	$\leq .0001$	.125	.23	$> .3$

Table 6.1 — maximum transform versus q and N

For this data, a simple formula was used for the tokamak background field: a 1/R toroidal field and a poloidal field due to a current carrying loop at the plasma axis. There is no background separatrix with this magnetic geometry. When the same helical configurations were tried with background fields produced by the PEST equilibrium code, we found that the maximum external transform that could be imposed varied from 60% to 80% of the maximum found with the analytic background field. The difference was found to be due to the presence of the axisymmetric separatrix of the PEST background fields. As the helical field is increased, the flux surfaces helically elongate and when an elongated surface passes through the original location of the axisymmetric separatrix the surface is broken. It was found that the elongations at a_p were about 1.3 to 1.7 with a constant pitch winding law versus 1.5 to 2.0 with an ultimate winding law, so a constant pitch winding law was chosen for the analysis. In all cases an extra vertical field was used to center the vacuum transform axis of the helical coils onto the plasma axis. Unfortunately the question of how much the surfaces will actually elongate can not be addressed in this report, because as the surfaces deform the plasma current profiles will change and the effect of this change on the deformation is unknown. A 3-D equilibrium code is needed to study this current migration.

These caveats aside, we can still examine Table 6.1 and see to what limit the axisymmetric representation for the plasma current is valid. For $\langle a_p \rangle / r_{\text{coil}} = .40$ and $\iota^{\text{vacuum}} = .15$, this occurs when the ratio of helical winding transform to plasma transform $= M^* = \frac{N}{\ell} q \simeq 3$. There is also an indication that the dependence of $\iota^{\max}$ is slightly greater on N/ℓ than it is on q, so perhaps a better figure of merit would be $M^* = \left(\frac{N}{\ell}\right)^{1.4} q^{0.6}$. This formula was obtained by fitting the data in Table 6.1 with the equation $M^* = \left(\frac{N}{\ell}\right)^a q^b$. This limit should not be viewed as the point where the flux surfaces are destroyed, but only as the point where the axisymmetric representation of the

plasma current becomes invalid.

In order to examine the limits of external transform and surface disruption, we now review data from two experimental devices that have been run in the tokamak-stellarator hybrid mode.

6.2 Experimental Devices

Experiments began of JIPP T-II at Nagoya University, Japan in July, 1976. JIPP T-II had a hybrid tokamak-stellarator configuration with the following parameters:

$$R_o = 9.1 \text{ m}$$

$$\eta_{\text{limiter}} = .17 \text{ m}$$

$$\ell = 2, N = 4 \text{ helical system}$$

$$\bar{\iota}^{ext} \sim .1 \text{ when } B_{zo} = 3 \text{ tesla}$$

$$\bar{\iota}^{ext} \sim .3 \text{ when } B_{zo} = 2 \text{ tesla}$$

In 1976[2], the plasma would suffer a current disruption when $q_{\text{axis}} < 3$ ($M^* = \frac{N}{\ell} q = 6$). In 1978[3], J. Fufita, et.al, reported that by using a vertical magnetic field to control plasma position, MHD activity in the plasma could be reduced, and that by having a second rapid ramp in the plasma current, $q_{\text{axis}} = 2.5$ could be obtained without a major disruption. These results can readily be compared to the base design described in Chapter II, since both machines have the same helical geometry (an N = 4, $\ell = 2$ stellarator configuration). The base design assumed an operating point of $M^* = 2$, while JIPP-T-II experiences major disruptions for $M^* < 5$, so a factor of 2.5 improvement is needed to meet the base design goals.

A second experimental device run in the tokamak-stellarator mode was Pulsator[4], located at the Max-Planck-Institut-für-Plasmaphysik in Garching. Pulsator's main parameters were:

$$R_o = 70 \text{ cm}$$

$$r_{\text{limiter}} = 12 \text{ cm}$$

$$B_{zo}^{max} = 2.8 \text{ tesla}$$

$$I_{\text{plasma}}^{max} = 100 \text{ KA}$$

Run as a pure tokamak, Pulsator was limited in the high density regime ($n_e^{\text{peak}} = 2 \cdot 10^{14}/\text{cm}^3$) by disruptive instabilities, with the lowest q^{edge} obtainable about 3.3 with $\beta_p = 1.5$. An $\ell = 2$, $N = 1$ stellarator winding was placed within the copper shell of Pulsator, and early experiments confirm our numerical result that an $N = 1$ helical system is unstable to a plasma transform - winding transform resonance. On Pulsator, for $q^{\text{edge}} = 3.5$, a critical helical current of 250 amperes (corresponding to $\iota^{\text{ext}} < 10^{-5}$ for $B_{zo} \simeq 3$ tesla) was sufficient to produce a disruption. F. Karger, et.al.[5] has reported that a stabilizing effect on low m - number MHD modes and spontaneous disruptive instabilities was found when a helical current 60% to 95% of the critical helical current was applied. (This would correspond to $I_{\text{helix}} \simeq 15$ KA for an $N = 1$ reactor design!) The stabilizing effect became greater as the helical current approached the instability level. It is possible that the resonant helical windings create a limited degree of ergodicity and island formation near the plasma axis that hinders the rotation of the MHD-modes and the convective growth of the perturbations. Unfortunately, these results were not easily reproducible, as it was difficult to add enough stabilizing helical current and still avoid disruptive resonance interaction. It is unlikely that it would provide the high certainty of disruption elimination required for reactor operations. One key problem with the use of feedback interaction of the resonant helical windings with spontaneous MHD-modes would

be that the diffusive penetration time of the helical fields into the plasma would be longer than the growth rate of the disruption ($\leq$ 100 ms). The authors thus felt it prudent to reject this method of disruption control for the base design. If the method ever does prove viable, the helical current requirements (and associated support and dissipative power requirements) are so small that no major changes would be needed in the standard tokamak design in order to accommodate the helices.

References

1) J. L. Johnson, et. al. Journal of Computational Physics 32, 212 (1979)

2) J. Fujita, et. al. Proceedings of the Sixth International Conference Plasma Physics and Controlled Nuclear Fusion Research; Berchtesgaden, 2, p. 95, 6–13 October 1976, International Atomic Energy Agency, Vienna, Austria

3) J. Fujita, et. al. Proceedings of the Eighth International Conference Plasma Physics and Controlled Nuclear Fusion Research; Brussels, 1, p. 209, 1–10 July 1980, International Atomic Energy Agency, Vienna, Austria

4) F. Karger, et. al. Proceedings of the Sixth International Conference on Plasma Physics and Controlled Nuclear Fusion Research; Berchtesgaden 1, p. 267, 6–13 October 1976, International Atomic Energy Agency, Vienna, Austria

5) F. Karger, et. al. Proceedings of the Fifth International Conference on Plasma Physics and Controlled Nuclear Fusion Research; Tokyo 1, p. 207, 11–15 November 1974, International Atomic Energy Agency, Vienna, Austria

Chapter VII. Illustrative Design

7.1 Summary of Design Parameters

The main parameters of the optimized $M^* = 4$ reactor design described in Chapter IV are listed in Table 7.1. The toroidal field on axis is 6 tesla, the plasma aspect ratio A is 9.4 and major radius is relatively small ($R_o = 14.31$ m). The large aspect ratio is attractive from the maintenance and assembly point of view because of the relative ease of access.

Figure 7.1 shows the top view of the coils. The helical coils are located inside the toroidal field coils. The toroidal field coils rest against the bucking cylinder. The helical coils, the helical coil support structure and the vacuum vessel are divided into sections in order to allow modularization of the system.

The relatively high aspect ratio of the coils allows a large ohmic heating transformer. Thus the pulse length in the machine can be subtantially increased over that in lower aspect tokamaks.

Figure 7.2 shows a 30^o elevation view of the machine. The toroidal field coils are circular, and have independent cryogenic dewars. This arrangement allow the possibility of removing the toroidal field coils for maintenance and repair.

Figure 7.3 shows a typical module. The modularization scheme is similar to that of the High Field Compact Tokamak Reactor (HFCTR). A module (consisting of the toroidal field coil, the cryostat, the first wall and blanket/shield, the internal helical coils and the support structure) is removed in a remote maintenance operation. A module would be remotely removed and replaced by

another unit. The time requirement for return to operations is therefore significantly reduced from that associated with a non-modular design.

Figure 7.4 shows a side view of the machine. Gaps between the modules are used for interconnecting the helical coils in adjacent modules.

7.2 Toroidal Field Coil: Basic Concept

The engineering of the toroidal field system is dominated by the influence of the helical coils on assembly and maintenance. Also of great importance is the support of the TF coils against the net inward radial force. The TF coils must be supported in a manner compatible with modularization.

The need for modularity for remote maintenance operation requires the use of features similar to those used in other reactor designs[1]. Total modularization requires a cryostat with sufficiently thick insulation to prevent large refrigeration loads. It also requires mechanical vacuum seals, module transporters, modular poloidal coils, and demountable helical field coils (if they are inside of the toroidal field coils).

The toroidal field is created by 32 toroidal field coils carrying 14.32 MA each. The toroidal field coils have a circular elevation shape. These coils have advantages with respect to D-shape coils in that they are easier to manufacture, and are smaller and therefore have less weight (less conductor and suport structure) than D-shape coils. Furthermore, it is not clear whether the claimed advantages of D-shape coils exist in real three dimensional structures [2].

The peak field at the conductor is $B_{peak} \sim 9$ T. A magnet with graded coils, using NbTi in the lower field region and Nb_3Sn in the higher field region, has been shown to minimize the cost

of the winding [3]. The reason for this is that the cheaper material, NbTi, can be used in the bulk of the magnet at relatively high current density, while the more expensive Nb_3Sb can be used in the the high field region exclusively. The use of a graded conductor, however, may require that the magnet be layer wound, instead of pancake wound, as were the coils designed in the HFCTR report. However, pancake wound magnets could be utilized if a reliable NbTi – Nb_3Sb joint could be developed[3].

In order that the TF coil system (together with its structurally dependent helical coils) be fully modular, the cryostats of each of the 16 modules must be independent and separable. This requires transmission of forces between the low temperature region and ground. This is done by means of G-10 compression members. The forces to be transmitted to ground are the centering forces of all the coils due to their mutual attraction and the torques caused by the weak vertical and helical fields.

The inward force per coil is 153 MN. This force is transmitted to the center post structure through epoxy-fiberglass G-10 strouts located in the dewar vacuum space. The strouts are each 20 cm long, 5.7 cm high, and 2 cm wide. The compressive stress in the G-10 is 85 MPa. In order to minimize the thermal load due to conduction through the G-10 strouts, heat sinks are introduced at 77 °K and 20 °K. The heat loads at the refrigeration points are .57 kW at 4.2 °K, 2.3 kW at 20 °K and 26.4 kW at 77 °K.

The required equilibrium field ($\sim$ 0.15 T) produces a torque on the TF coils. The associated horizontal forces on the TF coils must be transmitted to a room temperature torque frame through G-10 strouts, as for the inward force. Assuming 10 cm long strouts at 85 MPa in compression as before, and allowing for either direction of torque, the refrigeration loads at the three stations would

be .72 kW at 4.2 °K, 2.9 kW at 20 °K, and 33 kW at 77 °K. The overturning moments are small because the vertical field is low (because of the high aspect ratio). Therefore the frame required to resist the overturning is small.

The bucking cylinder on the inboard side is designed for a compressive stress of 200 MPA and is 0.75 meters in radial thickness. Figure 7.1 shows the bucking cylinder.

Figure 7.5 and Figures 7.6A through 7.6D illustrate the forces on the TF coil system. There are four TF coils per helical field period, and each TF coil within the field period is affected by the helical coils in a unique manner. The four coil positions are identified in Figure 7.5 , where the toroidal field is in the positive toroidal direction, and the toroidal current is in the positive poloidal direction (with the $\theta = 0^o$ position being on the outboard side). The forces on each TF coil are shown in Figures 7.6A through 7.6D . Each of these figures shows three plots:

1) A plot of the radial force due to the helical coils and the TF coil bursting force (with the radially inward normal being defined as the positive direction),

2) A plot of the small toroidal force on the TF coils due to the helical coils, and

3) A plot of the vector sum of the radial and toroidal forces.

The currents in the helical coils interact with the TF coils in proportion to the poloidal component of helical coil current. The direction of the interaction is along the minor plasma radius and alternates between adjacent helical coils from radially inward to radially outward. The net force on any TF coil is therefore small, and averaged over the toroidal angle there is no net force on the TF coil system. In order to to keep the toroidal forces on the TF coils from the helices small, and in order

to keep the bending moments on the TF coil cases due the helices at 20% of the bending moments produced by the TF coil bursting force (approximately 10 MN-m and 50 MN-m, respectively), about one meter of radial separation must exist between the helical coils and toroidal field coils. If there were no such separation, the toroidal forces on the TF coils due to the helices would be on the same order as the radial forces due to the helices, and the radial forces on the helices due to the TF coils would be on the same order as the anti-helical forces due to the TF coils. These forces would be very difficult to support. Thus, some space must be left between the helical coils and TF coils, and it is reasonable to fill this space with the helical coil support structure.

The principal effect within a TF coil due to the helical coils is to produce an elliptical deflection. The current in the helical coils is a factor of five lower than the current in the toroidal field coils, and the deflections on the TF coils from the helical fields are significantly smaller than the deflections due to the main toroidal field. In the base design, the maximum radial force on the TF coils due to the helical fields at any point is 1.5 MN/m, compared to a maximum bursting force of 55 MN/m along the inboard side. The helical coils maximize the peak bursting force for TF coil #3 and minimize the peak bursting force for TF coil #1 . The TF coil cases must be sufficiently rigid to keep the compressive stress and elliptical deflection within acceptable limits.

The local toroidal forces on the TF coils due to the helices are small (a maximum of 2 MN/m), and the net toroidal force is zero for TF coils #1 and #3 . There is approximately a 6 MN force on TF coil #2 in the positive toroidal direction, and a 6 MN force on TF coil #4 in the negative toroidal direction. These forces can be supported by shear panels between the TF coil cases.

7.3 Poloidal Field System: Axisymmetric and Helical Coils

The low current density of the helical coils (721 A/cm^2) facilitates the design of demountable joints which allow for electrical continuity between modules. Each of the helical coils carries a current of 2.91 MA, so, in order to reduce power supply requirements, it would be preferable that the helical coils be of multi-cable design (15 conductors, each carrying 194 kA), rather than be a single monolithic conductor. Each helical coil consists of 15 hard copper plates assembled into an outline measuring 1.10 m $\times$ 0.37 m. The planes of the conducting plates are parallel to the plasma minor radius. This minimizes the bending stresses in the beam, and gives additional rigidity to the structure.

The four coils of the helical coil system are held in place by the support structure. The radial force on the two coils carrying current in the direction of B_{zo} is outward, and the radial force on the other two coils is inward. The coils with an outward force lie in a groove in the support structure. For the coils with an inward radial force, a rigid frame is built around each coil to transfer the force to the support structure. This structure is illustrated in Figure 7.3 .

The forces on the helical field coils are shown in Figures 7.7A and 7.7B . The helical coil positions are shown in Figure 7.5 . The forces in Figures 7.7A and 7.7B are plotted versus the toroidal angle ϕ. A 90^o scan in ϕ is shown, representing a full 360^o poloidal rotation of each helical coil. The forces have a large $1/R$ variation due to the main toroidal field spatial variation. Superimposed on this field is a small perturbation due to the other helical coils. Because of symmetry, the net vertical and tilting forces on a toroidal sector that is 1/8 of the machine is zero. The net vertical and tilting forces on a toroidal sector of the structure supporting the helical coils are small. The avarage radial

force on the helices due to the TF coils is 10 MN/m, and the helical coil -- helical coil interactions add approximately a 10% modulation onto this force. Because these additional forces are small, it is possible to modularize the structure supporting the helical coils. That is, each module has an independent support struture for the helical coils. This fact is essential to allow modularization of the machine.

Figure 7.7A shows the forces on the helical coil carrying current in the direction of the toroidal field. In the diagram, the radially inward normal is defined as positive, and so the negative radial force shown represents an outward radial force on the helix. Near the horizontal axis the small anti-helical force on the coil is shown, and the vector sum of radial and anti-helical forces is also plotted. The anti-helical force is in the $I_h \times r$ direction, and is proportional to the magnetic ripple present in the toroidal field due to the discreteness of the TF coils. This anti-helical force is largest on the outboard side, where the ripple is greatest. Fortunately, this anti-helical force is always less than 1 MN/m, and the structure attaching the helical coils to the support girders can be made sufficiently strong to support this force.

Figure 7.7B shows the forces on the helical coil carrying current in the direction opposite to the toroidal field. The anti-helical force is so small compared to the radial force that the vector sum of the two forces can not be distinguished from the radial force alone. It can be seen that the radial force is now inward positive, and that the anti-helical force again peaks along the outboard side (see Figure 7.5 for illustration of magnetic geometry).

Interconnection between adjacent helical coil needs to be provided in the region between modules. In order to allow for space to interconnect the helical coil sectors, access is provided through the

support structure. It is estimated that 0.5 m^2 is required per helical coil connection. The support structure could provide 0.5 m gaps between the modules, or 1 m $\times$ 0.5 m cut-outs in the regions of the helical coil connections.

Ideally, when a module is rolled into its position in the toroid, each sector of each of the four helical coils inside the support structure should make a reliable contact with the corresponding sector in the the adjacent module. These contacts should have low enough resistance to assure that the temperature never rises high enough to cause damage to the conductor contact surface or to the conductor insulation. In the HFCTR design, the problem was solved by the use of clamping connectors. A similar set of connectors shown in Figure 7.8 serves the same purpose. The copper conductors are firmly clamped together in the bore component frame seen in Figure 7.8. The joints provide some flexibility, and the tolerance requirements needed to provide contact between the sectors of the helical coils in adjacent modules are reduced from the requirements associated with connecting the coils with separate overlapping connectors.

The base design also requires a set of vertical field coils (not shown) producing about 0.13 to 0.15 tesla of vertical field on the plasma axis. The coils producing this field would be located outside of the toroidal field coils.

The radiation flux at the helical coils must be sufficiently low so that the insulation between the copper plates is not damaged. There are preliminary indications[4] that G-10 epoxy insulation can withstand a total neutron fluence of approximately 6×10^{20} N/cm^2, if the stress on the insulation is on the order of 10,000 psi or less. The stresses on the helical coil insulation is well below this. There is about 500 psi between the helical plates due to the currents within the helical conductor, and about

2000 psi of pressure due to the current interacting with the background magnetic field. The primary neutron flux of the illustrative design at the first wall ($r = 140$ cm) is 1.06×10^{14} N / sec-cm^2, and the peak neutron flux inside the blanket will be approximately 20 times the incident flux[5]. An attenuation of the peak flux by a factor of 10^{-1} would allow a 90 year lifetime for the G-10 insulator, assuming continuous operation. Shielding material around the helical coils can reduce the neutron flux by a factor of 10 for each 13 cm of shielding thickness.[6] In the illustrative design, the distance between the helical coils and the plasma edge (ΔS) was set at 80 cm, allowing for a 20 cm void between the plasma and first wall and a 60 cm region of blanket and shield between the first wall and helical coils. Although a detailed design of the blanket neutronics is beyond the scope of this report, the thicknesses assumed are approximately sufficient for the amount of shielding required. More importantly, the design itself is fairly insensitive to a slight increase in the helical coil radius, if more shielding were indeed needed. Table 7.2 shows a parametric scan of the illustrative design for values of ΔS of 80 cm, 93 cm, and 106 cm. Each step represents 13 cm of additional shielding, and an associated factor of 10 reduction of the neutron flux on the G-10 insulator. The force/meter on the helices was increased in order to keep the plasma characteristics constant. As can be seen in Table 7.2, each additional 13 cm of shielding results in approximately a 20% increase in the force/meter on the helices and a 25% increase in the radial thickness of the helical support structure. Such a change, while significant, would have a relatively small overall impact on the base design.

7.4 Analysis of OH Drive

The number of volt-seconds in the OH drive is proportional to the flux enclosed by the OH coils. This flux is proportional to $B_{OH}R_{OH}^2$, where $B_{OH} = \mu_o I_{OH}/2R_{OH}$, and R_{OH} is the major radius of the OH coils. R_{OH} is approximately equal to the major radius of the inboard side of the toroidal field coils. (For the tokamak–stellarator base design, R_{OH} was set at 8 meters, while the major radius of the inboard side of the TF coils was 9.5 meters). The cross-sectional area of the structural support for the OH ring is proportional to $R_{OH}^2 B_{OH}^2$, while the stored energy E_{OH} is proportional to $R_{OH}^3 B_{OH}^2$. These quantities may be expressed as:

$$\text{Support cross-sectional area} \sim \frac{\text{flux}_{OH}^2}{R_{OH}^2}$$

$$E_{OH} \sim \frac{\text{flux}_{OH}^2}{R_{OH}}$$

Thus, for a given stored flux or volt-second capacity, structural support and energy storage requirements are sharply reduced for large R_{OH}.

The parameters of the OH system are given in Table 7.3.

For full swing operation (B_{OH} varying from plus to minus 1 tesla), the number of volt-seconds available from the ohmic transformer is 400 Vs. The total inductive drive is

$$\text{volt-seconds} = \text{volt-seconds}_{\,OHMIC} + \text{volt-seconds}_{\,VERTICAL}$$

Here volt-seconds $_{VERTICAL}$ refers to the contribution to the inductive drive from the vertical

field needed for equilibrium. As noted in the previous section, the vertical field is $\sim$ 0.15 T; the contribution to the inductive drive from the vertical field is 150 Vs. Therefore, the total inductive drive is 550 Vs, with a stored energy in the ohmic transformer of about 1.7 GJ.

7.5 Modularization

The machine is divided into 16 modules which can be remotely connected and disconnected and removed for replacement by a spare module. This scheme allows for very rapid module replacement[1]. The toroidal field coils are removed in the process, allowing for repairs of the toroidal field coils. The coils are in individual dewars. The coils are connected by shear panels to resist the overturning forces on the toroidal field coils due to the vertical field.

The modules would be in a wheeled base, as in the IIFCTR design [1]. Removal and replacement of a module would be accomplished on tracks.

Complete modularity of a TF coil unit requires the transmission of forces generated within the low temperature region through thermally resistant structure to ground. Both the radial inward force and the overturning torque must be transmitted through G-10 with low cryogenic load, while still allowing removal of a TF module.

The plan view and section view in Figure 7.3 show the basic features of a typical module.

7.6 Plasma Scenario — Start-Up

The start-up and shutdown of a tokamak–stellarator reactor will be similar to the start-up and shutdown procedures of a conventional tokamak[7]. The L/R time constant of the bucking cylinder is appoximately 5 seconds, so a start-up OH coil will be needed external to the bucking cylinder. The advantage of this fast ohmic transformer is that the startup and shutdown process could be shortened if this system can provide (or absorb) all of the required inductive drive; otherwise the plasma current decays with an L/R time constant of the plasma or the main ohmic transformer has to absorb the volt seconds, with the bucking cylinder slowing down the process. The inductive volt seconds at full plasma current is $\sim$ 140 Vs, with the vertical field providing (or subtracting) about 150 Vs. Therefore a small startup (and shut-down) tranformer would be required to provide the balance required between the required volt seconds provided by the vertical field and those required by the plasma.

Another possibility would be to start the plasma without the need of the high voltage spike, by using RF breakdown of the plasma [8].

It is possible that the tokamak–stellarator will be less sensitive to disruptions during start-up and shutdown than conventional tokamaks, due to the stabilizing influence of the helical coils. This would allow greater flexibility in the variations of plasma density, temperature, and current during start-up and shutdown. In particular, start-up could begin at a higher density, which would result in a faster start-up (due to the better coupling between the external power and the plasma) and thus a decrease in the external energy needed for ignition.

The auxiliary heating would be ICRF, coupled through waveguides. The ICRH power require-

ments during start-up will be approximately 150 MW according to the empirical scaling law for energy confinement [7,8]

In order to heat the plasma during start-up, sufficient access is necessary. If the heating power density is about 20 MW/m^2, then about 8 m^2 of access area would be required. If every other module had a port, the access per port would be 1.0 m^2. Therefore, the access port size required for heating is comparable to the access port size required for joining the coil sectors together.

For each burn cycle, the OH drive must be reset so that the plasma current will flow in the same toroidal direction, since the plasma and helical coil transforms must have the same sign. Assuming a 200 MW supply, the time required to reverse the OH transformer is approximately 15 seconds.

7.7 Plasma Scenario — Burn

The voltage requirement on the OH drive during the plasma burn may be written as:

$$V = \frac{4\pi B_{zo}\rho}{q_{edge}^{plasma}\mu_o}$$

where

$$\frac{1}{q_{edge}^{total}} = \frac{1}{q_{edge}^{plasma}} + \frac{1}{q_{edge}^{external}}$$

where ρ is the plasma resistivity. Since the tokamak–stellarator reactor operates best in a high B_{zo}, low q_{edge} regime (in the base design, $B_{zo} = 6$ tesla, and $q_{edge}^{total} = 1.4$), the reactor's voltage requirement is appoximately 1.5 times that of more conventional tokamaks (such as STARFIRE[9] or HFCTR[1]).

However, due to the large major radius of the tokamak–stellarator reactor ($R_o = 14.31$ meters in the base design), the large inboard area available for flux storage allows for very long burn times.

The classical Spitzer plasma resistivity of the base design is 5.66×10^{-10} ohm-meters, assuming $Z^{\text{eff}} = 1$, $T_e = 15$ KeV, and $\log_e \Lambda = 20$. The associated voltage requirement for the OH drive is .0224 volts. Since there are 400 volt-seconds available for the burn in the OH system, the burn could last for 18,000 seconds (that is, 5 hours). Even longer burn times could be achieved by increasing the OH current (eg. $\tau_{burn} = 10$ hours for $B_{OH} = 2$ tesla). Inductive losses and anomalous resistivity might reduce these ideal burn limits by 50% or more. It does appear, however, that 5 hour burn times would be practical.

If there is no need to do wall conditioning in between pulses and if the vacuum pumping speed is high enough, the shut down-time will be determined by the time required to recharge the OH transformer (which is a fraction of a minute). There is need for only a small amount of inertial energy storage to keep the steam generator operating during the shut-down phase.

$\tilde{\iota}_{external}$	0.1
β_t	5.3%
B_{zo} (tesla)	6
N , M^*	8 , 4
margin of ignition	5.53
a_{plasma} (meters)	1.52
R_o (meters)	14.31
I_p (MA)	2.94
r_{coil} (meters)	2.50
t (meters)	0.367
I_{helix} (MA)	2.91
$\mathcal{F}$	.08
$\langle j \rangle_{helix}$ (A/cm^2)	721
$\langle \mathcal{Q} \rangle$ (MN/m)	10
$P_{th}^{primary}$ (MW)	3000
wall loading (MW/m^2)	3.50

Table 7.1 — Main Machine Parameters of Illustrative Design

Constraints			
$\bar{\iota}_{external}$	.1	.1	.1
K_β	.5	.5	.5
B_{zo} (tesla)	6	6	6
$\mathcal{F}$	.08	.08	.08
$\mathcal{Q}$ (MN/m)	10	11.9	14.1
$P_{th}^{primary}$ (MW)	3000	3000	3000
N , M^*	8 , 4	8 , 4	8 , 4
ΔS (meters)	.8	.93	1.06
Parameters			
margin of ignition	5.53	5.53	5.53
wall loading (MW/m^2)	3.50	3.50	3.50
t (meters)	.366	.447	.541
a_{plasma} (meters)	1.52	1.52	1.52
r_{coil} (meters)	2.50	2.50	2.50
R_o (meters)	14.31	14.31	14.31
I_{helix} (MA)	2.91	3.32	3.77
$\langle j \rangle_{helix}$ (A/cm^2)	721	632	556
$h + 2\,t_p$ (meters)	1.01	1.27	1.59

Table 7.2 — Parametric Scan of shielding thickness versus $\mathcal{Q}$

B_{OH}	$\pm$ 1 tesla
R_{OH}	8 meters
I_{OH}	$\pm$ 12.7 MA
E_{OH}	1.7 GJ
bursting force per unit length	22.0 MN/m
cross sectional area of structural support	0.87 m^2

Table 7.3 — Parameters of OH drive

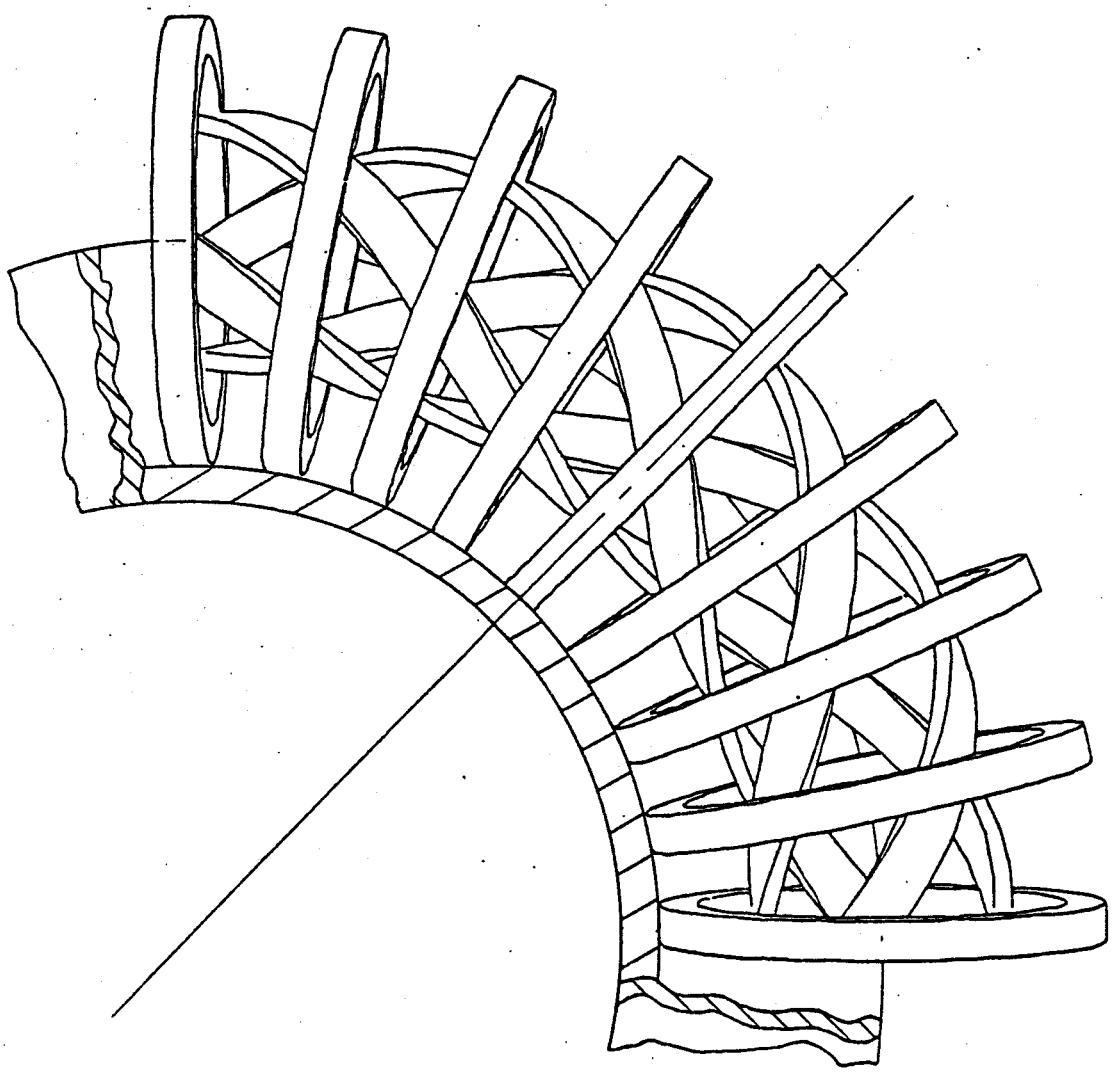

FIGURE 7.1
TOP VIEW OF ILLUSTRATIVE DESIGN

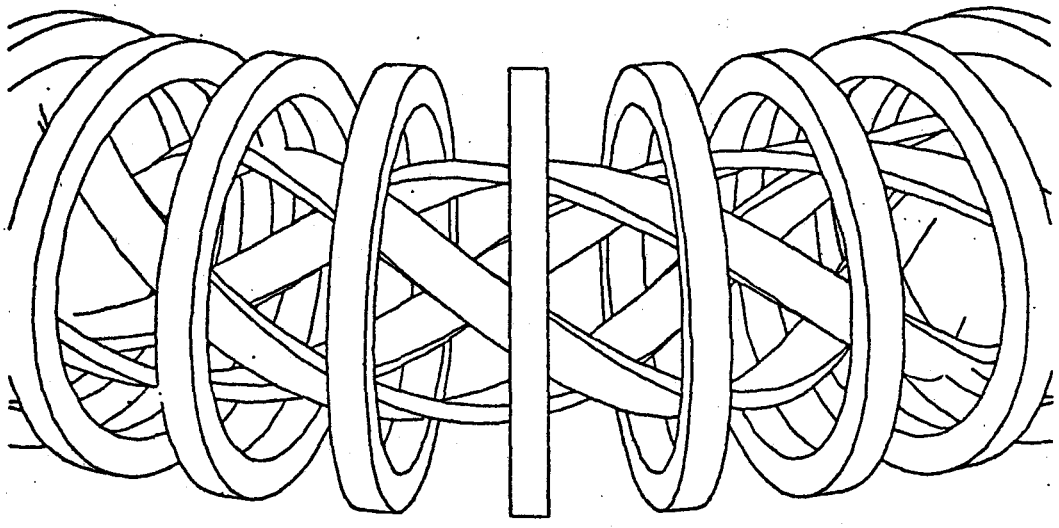

FIGURE 7.2
30° ELEVATION VIEW OF HELICAL AND TOROIDAL FIELD COILS

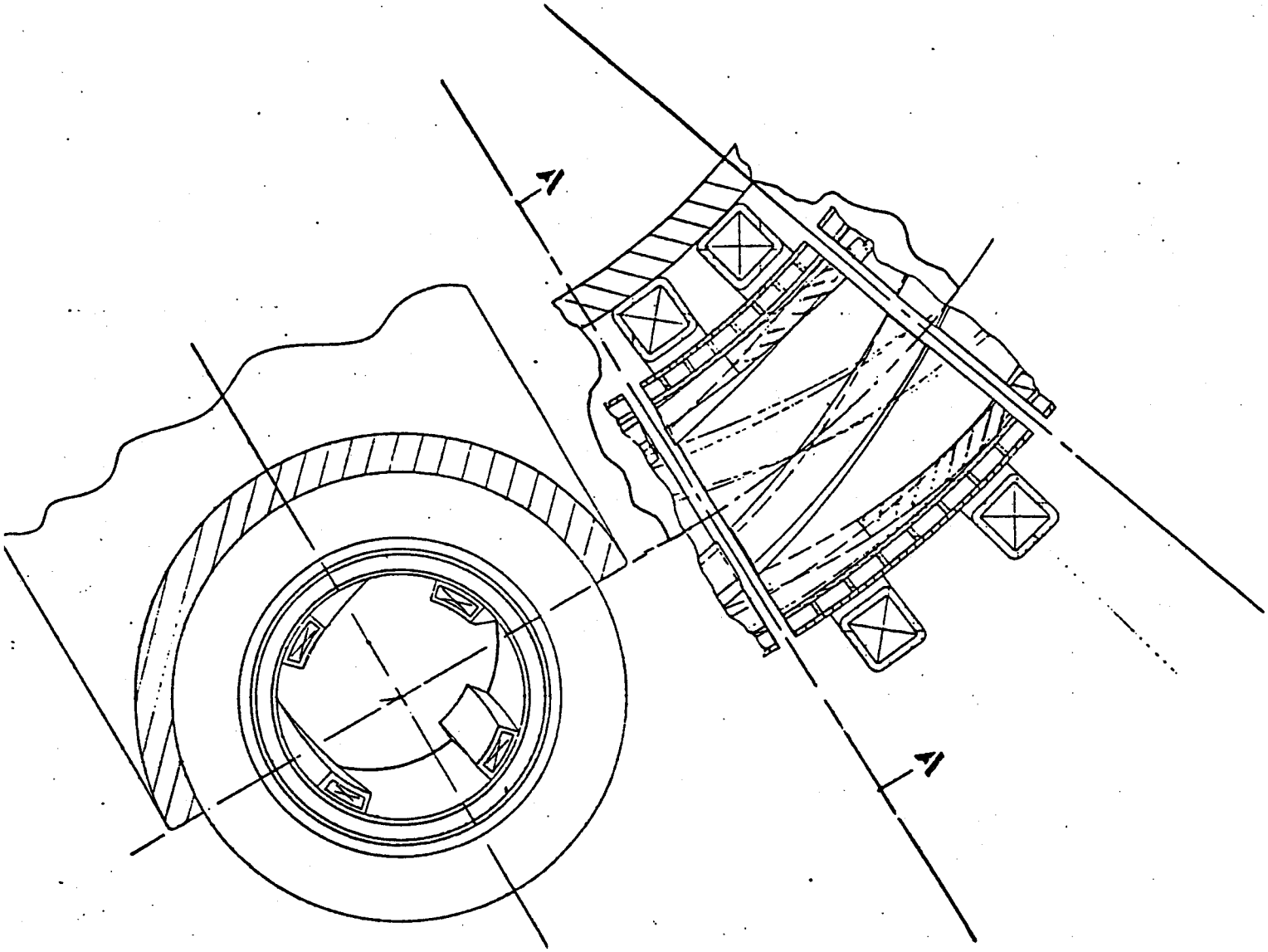

SECTION A - A

FIGURE 7.3
PLAN VIEW OF REACTOR MODULE

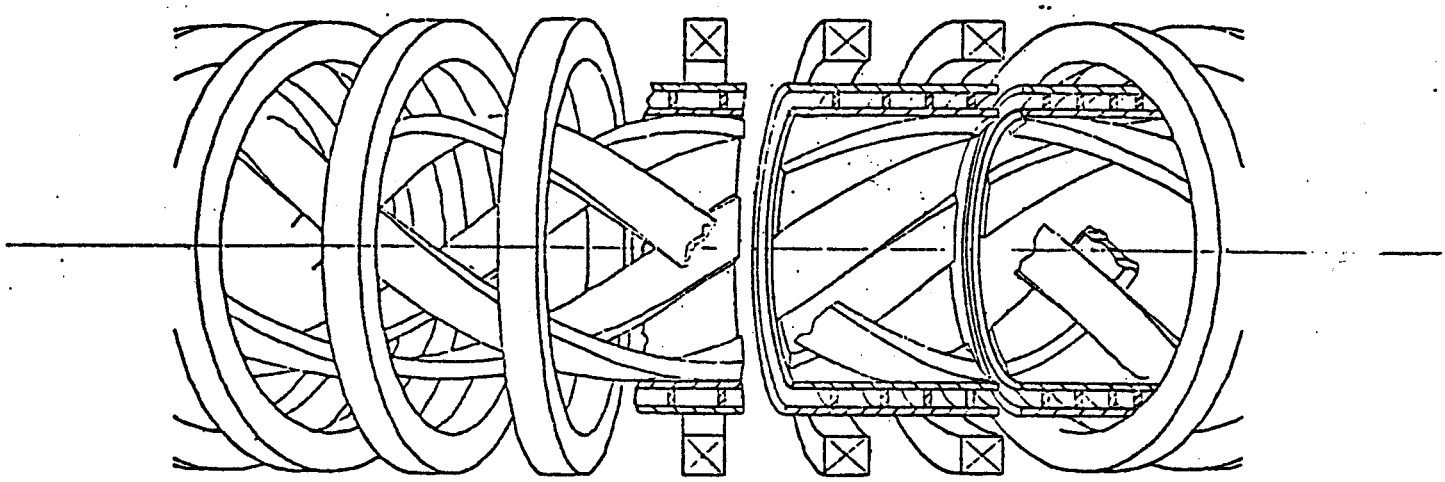

FIGURE 7.4
SIDE VIEW OF ILLUSTRATIVE DESIGN

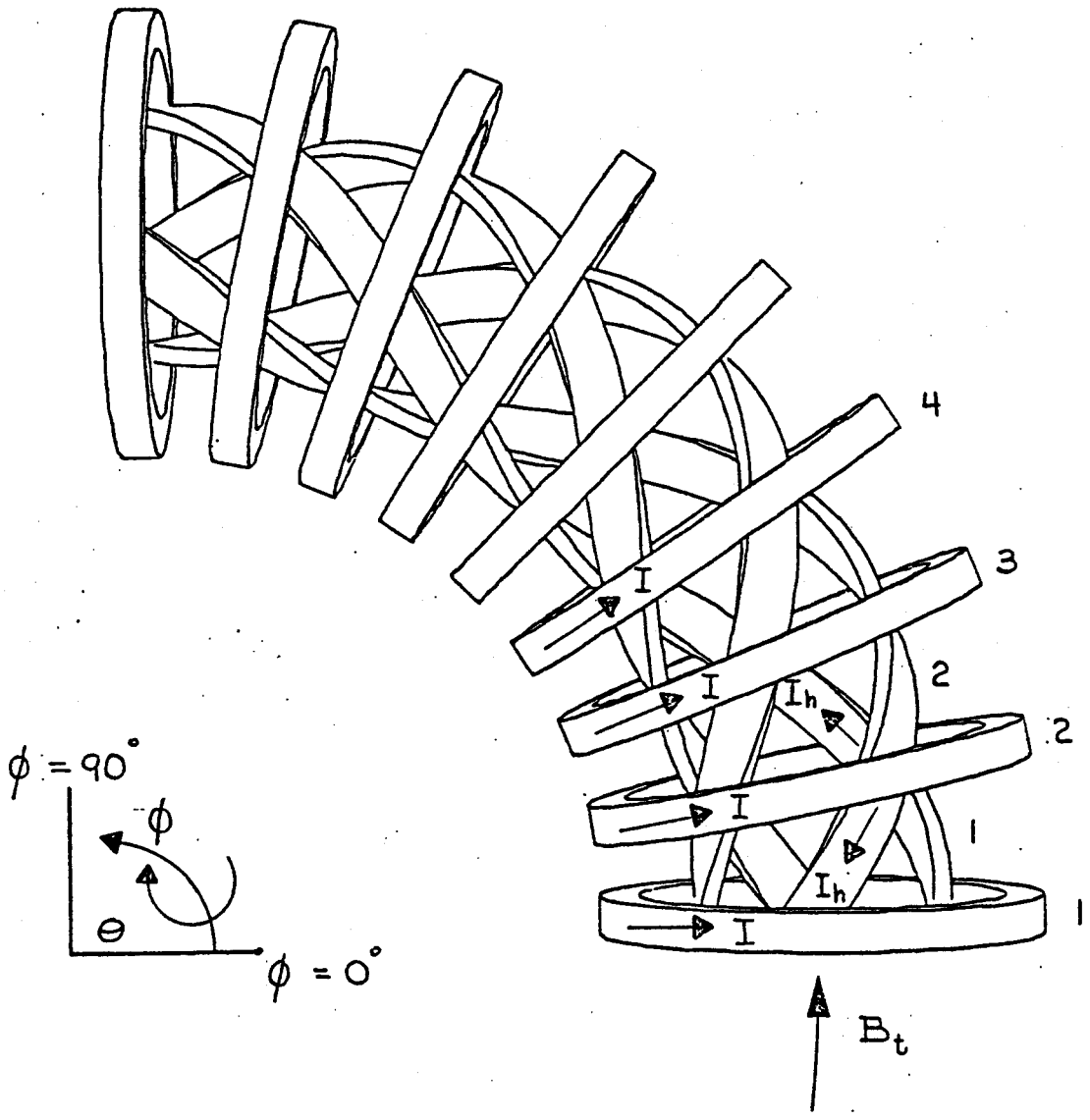

FIGURE 7.5
MAGNETIC GEOMETRY

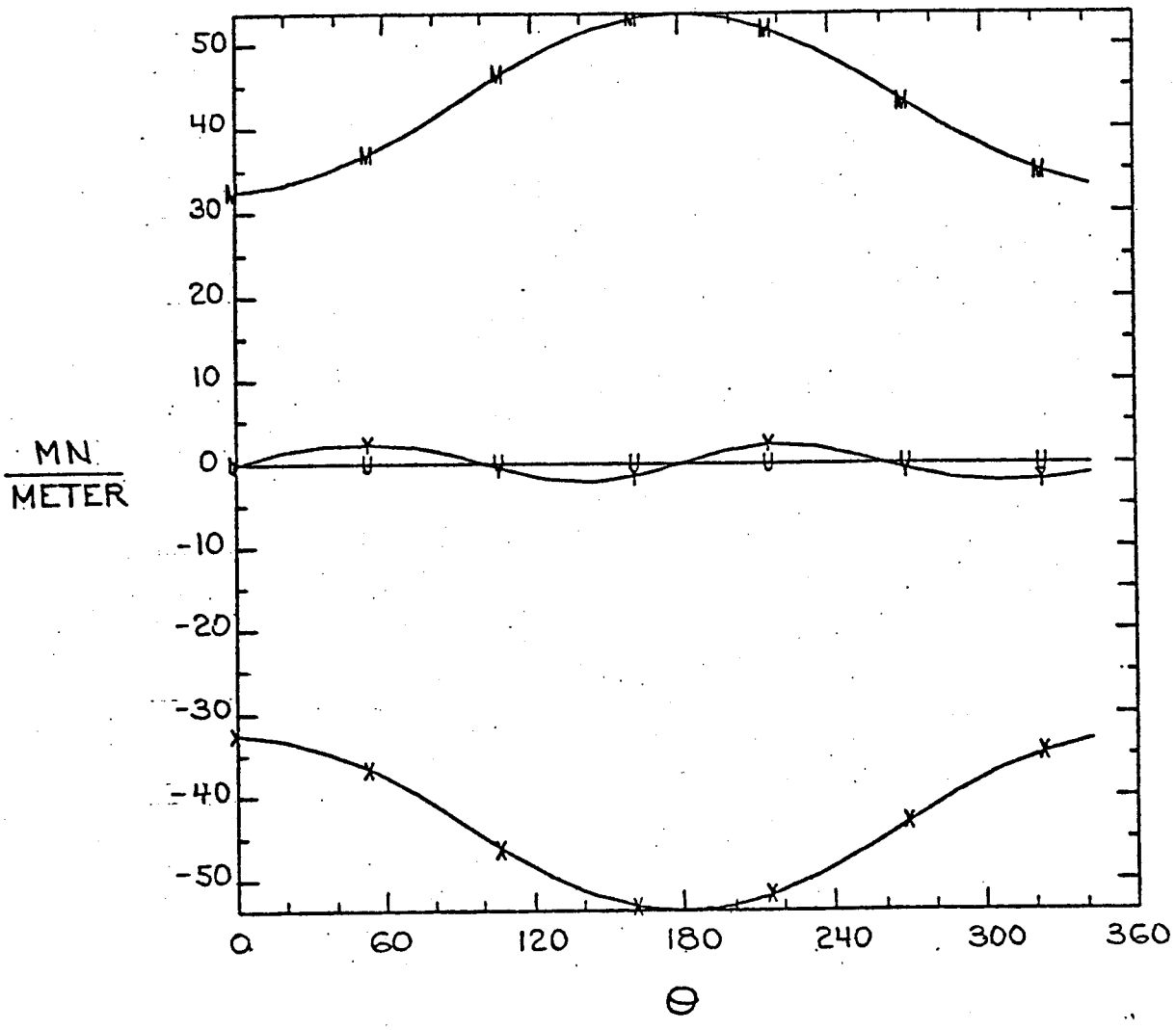

FIGURE 7.6A
FORCES ON TF COIL #1

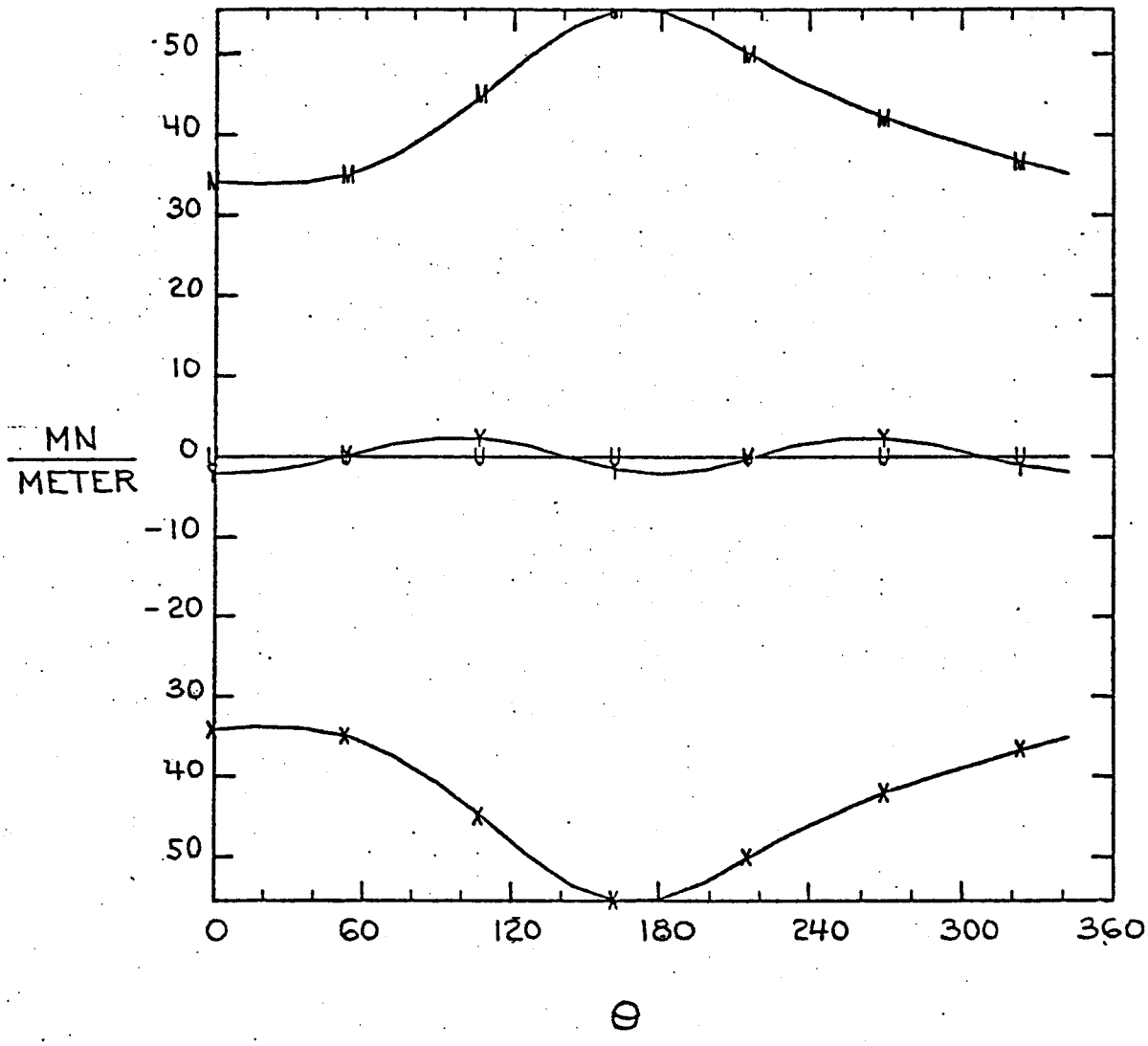

FIGURE 7.6 B
FORCES ON TF COIL #2

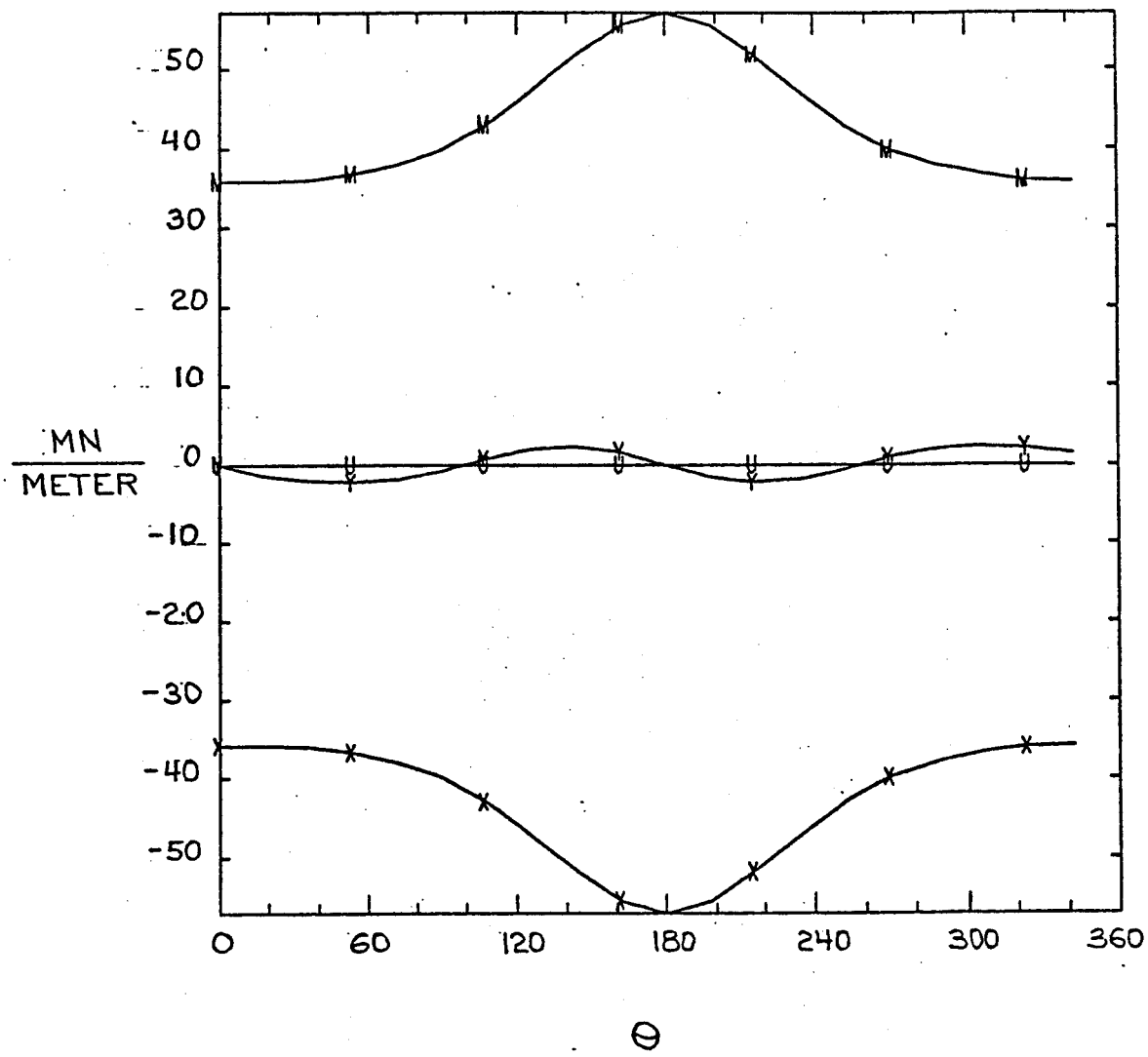

FIGURE 7.6C
FORCES ON TF COIL #3

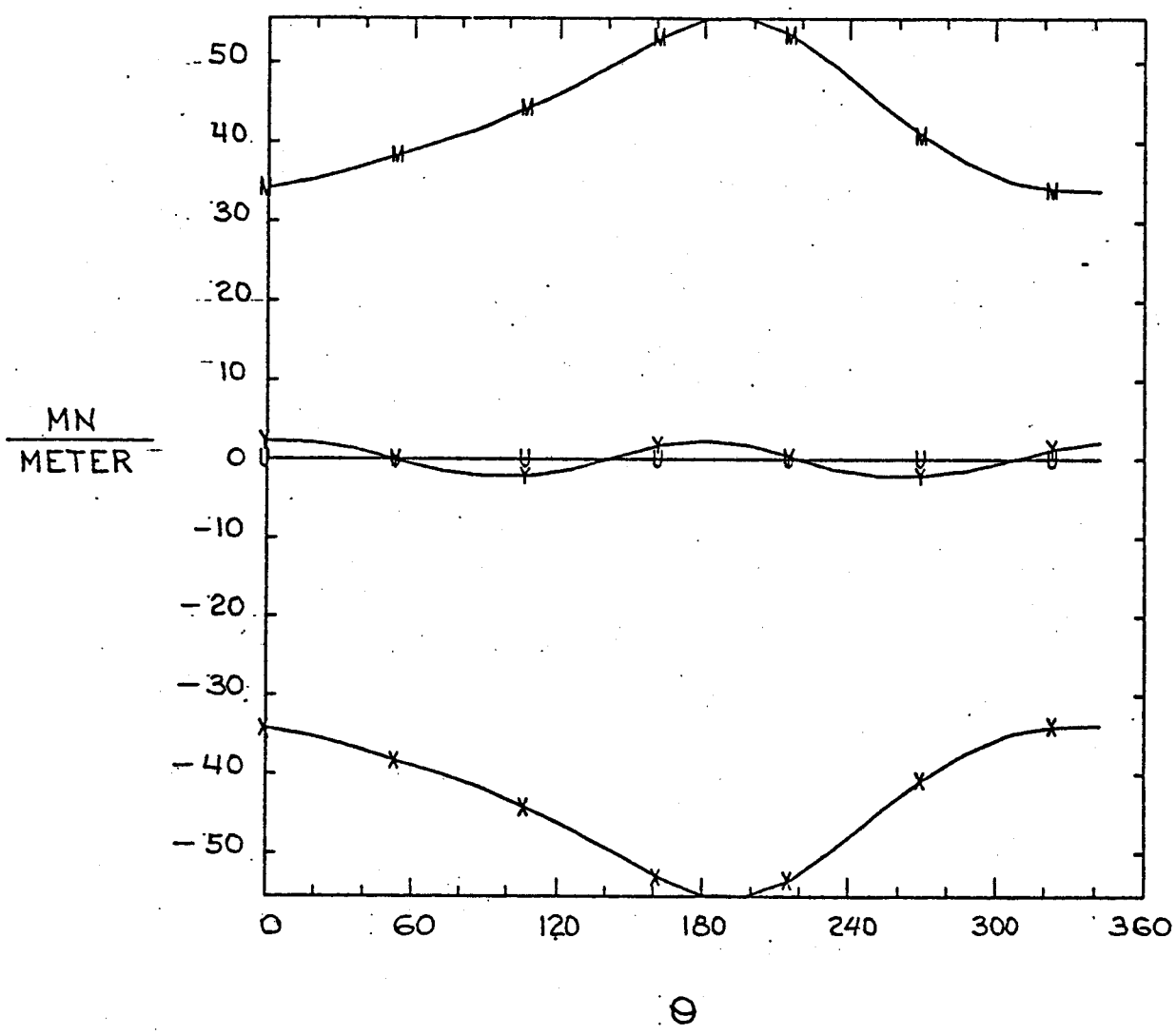

FIGURE 7.6D
FORCES ON TF COIL #4

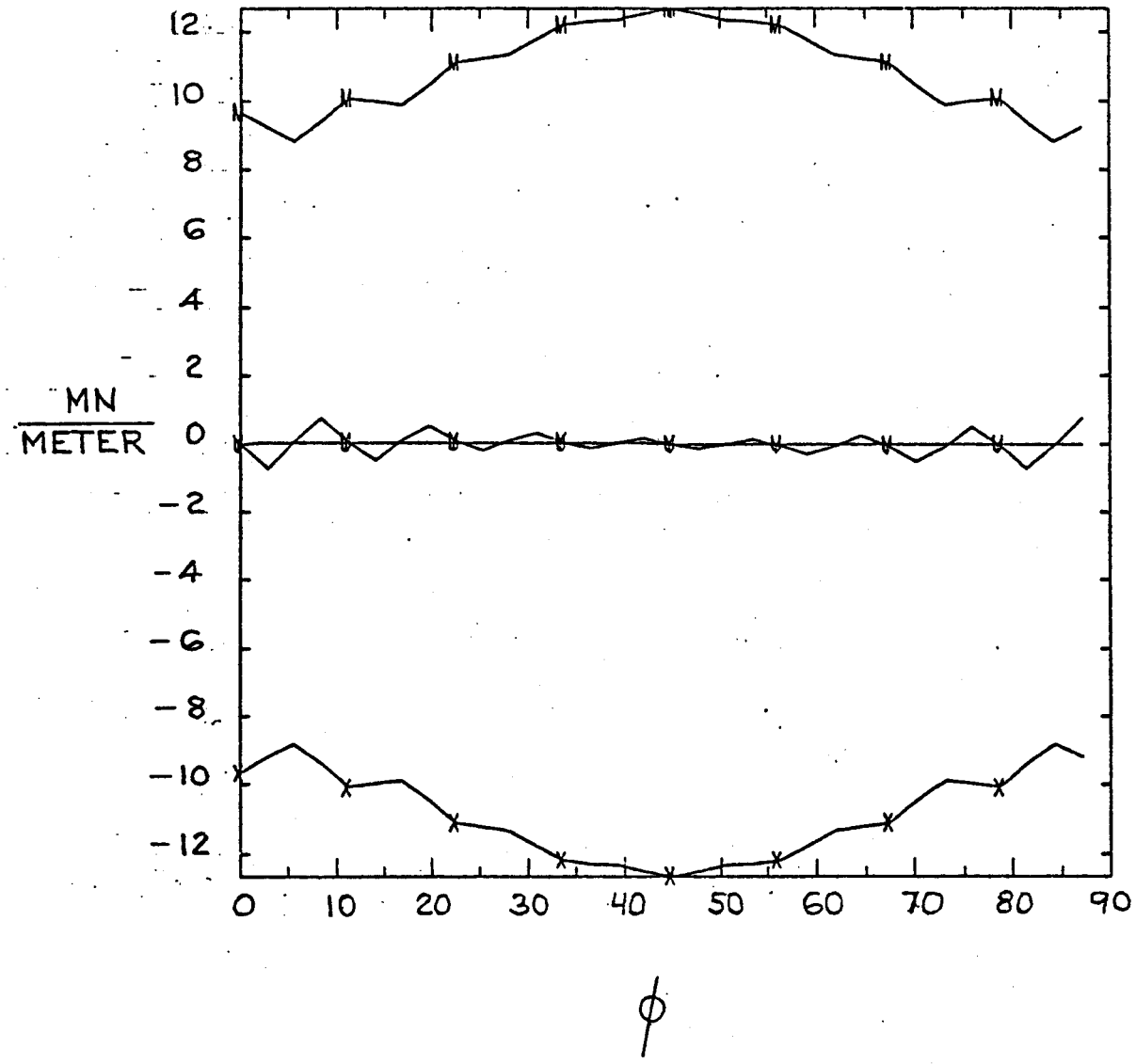

FIGURE 7.7A
FORCES ON HELICAL COIL #1

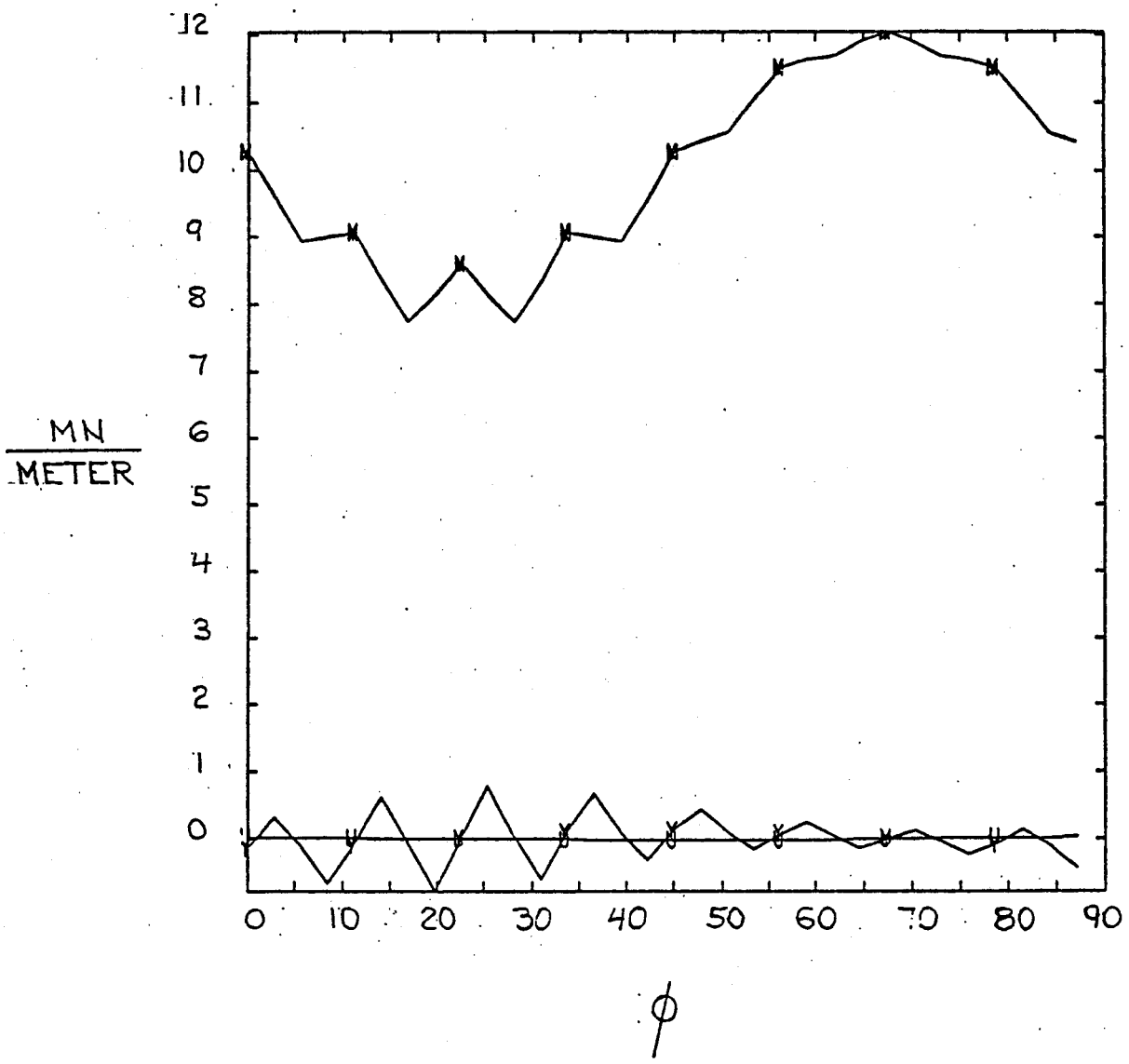

FIGURE 7.7B
FORCES ON HELICAL COIL #2

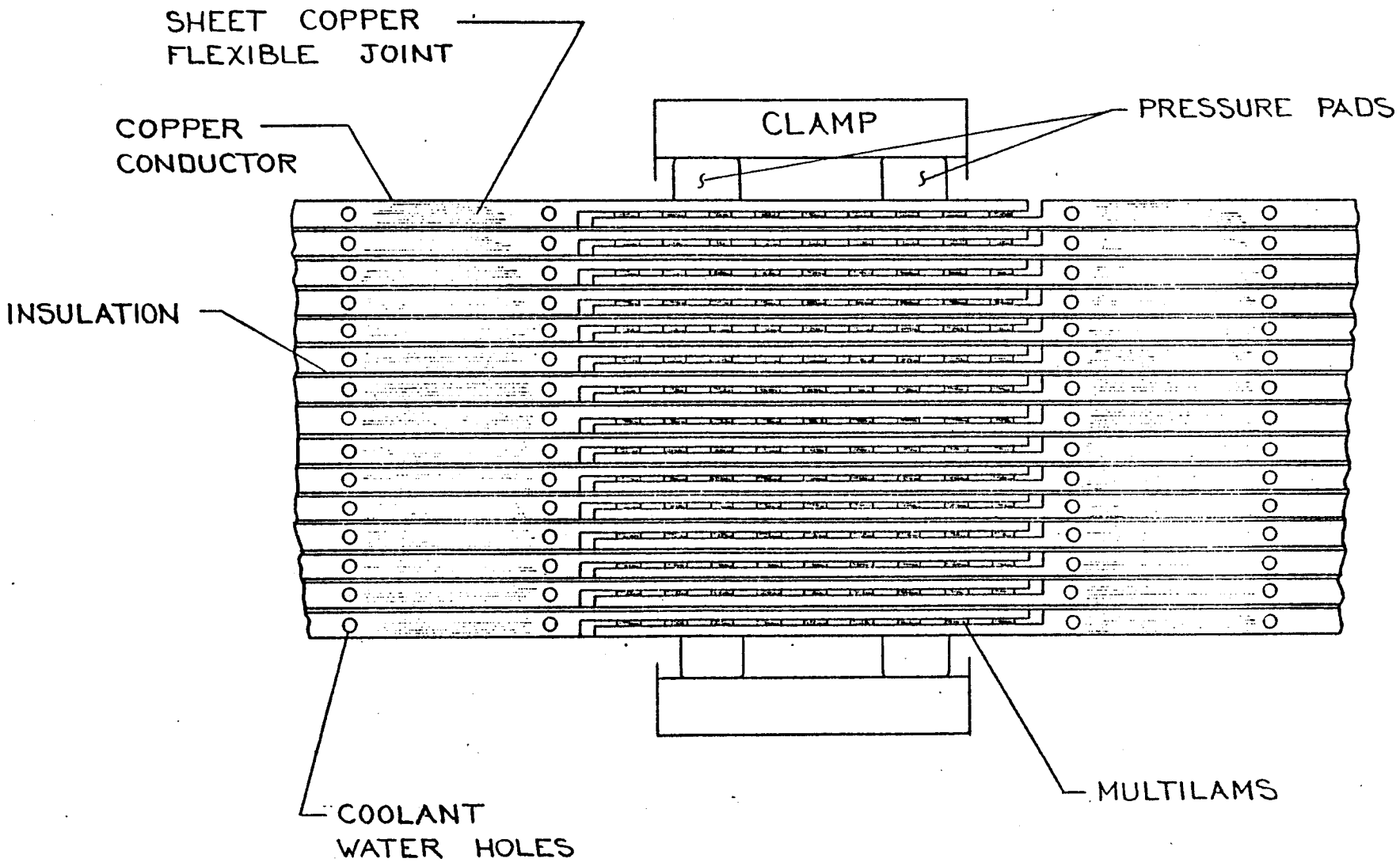

FIGURE 7.8
TOP VIEW OF HELICAL COIL CONNECTOR

References

1) D.R. Cohn, et. al. M.I.T. Plasma Fusion Center Report PFC/RR-79-2, 1979.

2) E. Bobrov and J.H. Schultz, Proceedings of the Ninth Symposium on Engineering Problems of Fusion Research, Chicago, Ill (Nov. 1981).

3) J. Schultz, MIT Plasma Fusion Center, personnal communication

4) E.A. Erez and H. Becker, International Cryogenic Materials Conference, Geneva, 1980.

5) J.E.C. Williams, et. al. M.I.T. Plamsa Fusion Center Report PFC/RR-81-24, 1981.

6) B. Badger, et. al., NUWMAK report, UWFDM-330, University of Wisconsin, 1979.

7) Report of the International Tokamak Reactor Workshop, International Atomic Energy Agency, 1980.

8) Y.K.M. Peng, S.K. Borowski, and T. Kammash, Nuclear Fusion 18 (1978) 1489

9) STARFIRE, A Commercial Tokamak Fusion Power Plant Study, Argonne National Laboratory ANL/FPP-80-1, Volumes 1 and 2, September 1980, Argonne, Illinois

Acknowledgements

The authors gratefully acknowledge many useful discussions with Dr. Peter A. Politzer and Dr. Lawrence M. Lidsky during this study. This work was supported by Department of Energy contract DE-ACO2-78ET-51013.

EXTERNAL DISTRIBUTION

Institutions

Argonne National Laboratory
Association Euratom-CEA
    Grenoble, France
    Fontenay-aux-Roses, France
Atomics International
Austin Research Associates
Bank of Tokyo
Brookhaven National Laboratory
CNEN-Italy
College of Wiliam and Mary
Columbia University
Cornell University
    Laboratory for Plasma Studies
    Applied & Engineering Physics
Culham Laboratory
Culham Laboratory/Project JET
E G & G Idaho, Inc.
Electric Power Research Institute
Gneral Atomic Company
General Electric Company
Georgia Institute of Technology
Grumman Aerospace Corporation
Hanform Engineering Development Lab.
Hiroshima University
Japan Atomic Energy Research Institute
Kernforshungsanlage/Julich GmbH
Kyoto University
Kyushu University
Lawrence Berkeley Laboratory
Lawrence Livermore Laboratory
Los Alamos Scientific Laboratory
Max Planck Institut für Plasma Physik
McDonnell Douglas Astronautics Co.
Nagoya University
Naval Research Laboratory
New York University/Courant Institute
Nuclear Service Corporation
Oak Ridge National Laboratory
Osaka University
Physics International Group
Princeton University/Plasma Physics
Sandia Research Laboratories
Science Applications, Inc.
    Fusion Energy Development
    Lab for Applied Plasma Studies
    Plasma Research Institute
Stanford University
University of California/Berkeley
    Dept. of Electrical Engineering
    Dept. of Physics
University of California/Irvine
University of California/Los Angeles
    Dept. of Electrical Engineering
    Dept. of Physics
    Tokamak Fusion Laboratory
    School of Eng. & Applied Science
University of Maryland
    Dept. of Electrical Engineering
    Dept. of Physics
    Inst. for Physical Science & Tech.
University of Michigan
University of Rochester
University of Texas
    Dept. of Mechanical Engineering
    Dept. of Physics
University of Tokyo
University of Washington
University of Wisconsin
    Dept. of Nuclear Engineering
    Dept. of Physics
Varian Associates
Westinghouse Electric Corporation
Yale University

EXTERNAL DISTRIBUTION

Individuals

Amheard, N.
Electric Power Research Institute
Balescu, R.C.
University Libre de Bruxelles
Bartosek, V.
Nuclear Res. Inst., Czechoslovakia
Berge, G.
University of Bergen, Norway
Braams, C.M.
FOM/Inst. for Plasma Phys., Netherlands
Brunelli, B.
C.N.E.N.-Centro Frascati, Italy
Brzosko, J.S.
Inst. of Physics, Warsaw University
Cap, F.
Inst. fur Theor. Physik, Innsbruck
Conn, R.W.
Chemical Engineering, UCLA
Consoli, T.
Residence Elysee I, Claud, France
Cuperman, S.
Dept. of Physics, Tel-Aviv University
Engelhardt, W.
Max-Planck Institute für Plasmaphysik
Engelmann, F.
FOM/Inst. for Plasma Phys., Netherlands
Fiedorowicz, H.
Kaliski Inst. of Plasma Physics, Warsaw
Frolov, V.
Div. of Research & Laboratories, Vienna
Fushimi, K.
Science Council of Japan, Tokyo
Gibson, A.
JET/Culham, Abingdon, England
Goedbloed, J.P.
FOM/Inst. for Plasma Phys., Netherlands
Goldenbaum, G.
Lawrence Livermore Laboratories
Hamberger, S.M.
Australian National University
Hellberg, M.A.
University of Natal, South Africa
Hintz, E.A.K.
Kernforschungsanlage/Julich GmbH
Hirose, A.
University of Saskatchewan
Hirsch, R.
EXXON Research & Engineering Co.
Hosking, R.J.
University of Waikato, New Zealand
Ito, H.
Osaka University
Jacquinot, J.G.
CEN/Fontenay-aux-Roses, France
Jensen, V.O.
Riso National Lab, Denmark
Jones, R.
National University of Singapore
Kadomtsev, B.B.
Kurchatov Institute, Moscow
Kostka, P.
Central Res. Inst., Budapest
Kunze, H.-J.
Ruhr-Universitat, F. R. Germany
Lackner, K.
Max-Planck Inst. für Plasmaphysik
Lee, S.
University of Malay
Lenhert, B.P.
Royal Inst. of Technology, Sweden
Malo, J.O.
University of Nairobi, Kenya
Mercier, C.H.B.
C.N.E.N./Fontenay-aux-Roses, France
Nodwell, R.A.
University of British Columbia, Canada
Offenberger, A.A.
University of Alberta, Canada
Ortolani, S.
Centro di Studio/C.N.R., Italy
Palumbo, D.
Rue de la Loi, 200, Bruxelles
Pellat, R.
Centre National, Palaiseau, France
Paquette, G.
Universite de Montreal, Canada
Rabinovich, M.S.
Lebedev Institute, Moscow
Razumova, K.A.
Kurchatov Institute, Moscow
Rogister, A.
Kernforschungsanlage/Julich GmbH
Rosenau, P.
Technion, Haifa, Israel
Rosenblum, M.
Soreq Research Center, Yavne, Israel
Rudakov, L.I.
Kurchatov Institute, Moscow
Ryutov, D.D.
Nuclear Physics Instit., Novosibirsk
Salas, J.S.R.
Inst. Nacional de Investig. Nucleares
Shafranov, V.D.
Kurchatov Institute, Moscow
Smirnov, V.P.
Kurchatov Institute, Moscow
Spalding, J.-J.
Culham Laboratory, Abingdon, England
Tachon, J.
CEN/Fontenay-aux-Roses, France
Tewari, D.D.
Dept. of Physics, IIT, New Dehli
Trocheris, M.
CEN/Fontenay-aux-Roses, France
Vandenplas, P.E.
Ecole Royale Militaire, Bruxelles
Verheest, F.
Rijksuniversiteit, Gent, Belgium
Watson-Munro, C.N.
University of Sydney, Australia
Wesson, J.A.
Culham Laboratory, Abindgon, England
Wilhelm, R.
Inst. für Plasmaphysik, Stuttgart
Wilhelmsson, K.H.B.
Chalmers Univ. of Technology, Sweden
Wobig, H.
Max-Planck Inst. für Plasmaphysik